Mountain Waves and Downslope Winds: Forecasts, Predictability, and Data Assimilation

Patrick Alexander Reinecke

A dissertation submitted in partial fulfillment
of the requirements for the degree of

Doctor of Philosophy

University of Washington

2008

Program Authorized to Offer Degree: Atmospheric Sciences

University of Washington
Graduate School

This is to certify that I have examined this copy of a doctoral dissertation by

Patrick Alexander Reinecke

and have found that it is complete and satisfactory in all respects,
and that any and all revisions required by the final
examining committee have been made.

Chair of the Supervisory Committee:

_____
Dale R. Durran

Reading Committee:

_____
Dale R. Durran

_____
Gregory J. Hakim

_____
James D. Doyle

Date: _____

In presenting this dissertation in partial fulfillment of the requirements for the doctoral degree at the University of Washington, I agree that the Library shall make its copies freely available for inspection. I further agree that extensive copying of this dissertation is allowable only for scholarly purposes, consistent with "fair use" as prescribed in the U.S. Copyright Law. Requests for copying or reproduction of this dissertation may be referred to Proquest Information and Learning, 300 North Zeeb Road, Ann Arbor, MI 48106-1346, 1-800-521-0600, or to the author.

Signature_____

Date_____

University of Washington

Abstract

Mountain Waves and Downslope Winds: Forecasts, Predictability, and Data Assimilation

Patrick Alexander Reinecke

Chair of the Supervisory Committee:
Professor Dale R. Durran
Atmospheric Science

An investigation of the predictability of mountain-waves and downslope winds is conducted with high-resolution numerical weather prediction (NWP) ensemble simulations. While the features predicted in these models look realistic, their predictability has yet to be explored. An ensemble Kalman filter (EnKF) is implemented into the atmospheric portion of the Navy's Coupled Oceanic/Atmospheric Modeling System (COAMPS) to explore the predictability characteristics of orographically generated mountain waves and downslope winds.

The predictability of two prototypical downslope wind events is explored with a 70 member ensemble generated with an EnKF and the COAMPS model. In the first event, large amplitude mountain-wave breaking is the dominant mechanism responsible for the strong downslope winds. In the second event the mountain wave experiences non-linear amplification associated with the layering of the upstream static stability profile. Wave breaking is not present for the second event. While the predictability is shown to differ for each event, the forecast uncertainty for both cases grows rapidly with the ensemble members differing by as much as 30 m s^{-1} within a 12-hr simulation. The mechanisms

for error growth in each event will be discussed.

The potential for assimilating mesoscale observations into a high-resolution NWP model is also explored. It is shown that the EnKF can produce realistic analysis increments associated with surface wind observations. Several examples of analysis increments are given for wind observations both upstream and downstream of a major mountain barrier.

Analytic solutions for discrete flow over topography suggest that numerical errors associated with poorly resolved features lead to decreased mountain-wave and downslope-wind predictability at non-hydrostatic scales. Linear analysis shows that insufficient resolution of non-hydrostatic waves forced by the topography can lead to a 30% over-amplification of the mountain wave. This result is confirmed in the fully nonlinear COAMPS model where discretization errors produce a significant amplification of the standing mountain wave and result in up to a 20 m s^{-1} over-prediction of downslope winds. Modifying the advection scheme in the model significantly reduces the ensemble spread of downslope winds.

TABLE OF CONTENTS

LIST OF FIGURES

LIST OF TABLES

ACKNOWLEDGMENTS

I would like to extend my deepest gratitude to my advisor Dale Durran who has given me the opportunity explore my research interests and taught me how to be a scientist. I would also like to thank Greg Hakim, Jim Doyle, and Dennis Hartmann for serving on my thesis committee as well as Jessica Lundquist who was able to step in at the last moment to serve as my GSR. I am also indebted to Ryan Torn who has answered numerous questions regarding data assimilation and predictability, as well as providing the core of the EnKF code. This research would not of been possible without a generous grant of computer time from Jim Doyle. Finally, I would like to express my sincere appreciation of my wife Amy who has stood by me and supported me through this long 6-year process. She is a constant source of joy and inspiration.

Chapter 1
INTRODUCTION

1.1 Overview and Motivation

In recent years the availability of high resolution numerical weather prediction (NWP) has increased substantially, due in part to great strides in computing ability. In fact, it is not uncommon for the horizontal resolution of operational forecasts to exceed 2 km (e.g Grubišić et al., 2008). While these models appear to be producing realistic looking forecasts, the ability to accurately predict features on such small scales is largely unknown.

Early assessments of mesoscale predictability suggested that small-scale motions may have an intrinsically shorter prediction period than larger-scale motions (Lorenz, 1969). However, as mesoscale models became common place, an optimistic view of mesoscale predictability emerged. Anthes et al. (1985) argued that many mesoscale phenomenon can attain extended predictability because they are either well organized and are able to resist the energy cascade described in Lorenz or are controlled by by well known physical boundaries such as orography and land characteristics. However, Anthes et al. did not propose a physical mechanism of how orography or land characteristics could extend predictability and subsequent studies found that much of the apparent enhancement was due to a combination of numerical dissipation, deterministic lateral boundary conditions which advected "error-free" information into the domain, and the fact that the initial perturbations projected onto gravity wave modes which rapidly decayed after an initial period of geostrophic adjustment (Errico and Baumhefner, 1987; Paegle and Vukicevic, 1989; Ehrendorfer and

Errico, 1995). Nevertheless, there is a widely held belief that topography significantly enhances mesoscale predictability (e.g. Vukicevic and Errico, 1990; Mass et al., 2002).

One of the earliest examples of the apparent enhancement of mesoscale predictability by topography was given in the context of a linear two-dimensional mountain-wave and downslope-wind model (Klemp and Lilly, 1975). The model was initialized with soundings upstream of the Colorado Rockies and used to forecast downslope wind events in Boulder, CO. For soundings taken 3-5 hours prior to the event the model produced a positive correlation between the predicted and observed winds. This positive correlation led some to speculate that the predictability of downslope winds and mountain waves was determined almost entirely by the synoptic scale predictability and that accurate downslope wind forecasts could be made up to 24 hrs in advance (e.g. Anthes, 1984). While Klemp and Lilly found a high correlation between the predicted and observed wind speeds, subsequent use of the model demonstrated that it had a tendency to over-forecast wind-storm frequency (Bower and Durran, 1986).

One issue with the Klemp and Lilly model is that downslope winds can be a strongly non-linear phenomenon (Peltier and Clark, 1979; Durran, 1986a, 1992). More recently, Nance and Coleman (2000) developed a two-dimensional non-linear downslope-wind forecasting tool. Their model was initialized with Eta soundings upstream of several mountainous locations throughout the western United States. Unfortunately, as with the Klemp and Lilly model, their model was unable to differentiate between wind-storm events and null events. They hypothesized that the low forecast skill was associated either to the two-dimensional model being unable to capture the relevant downslope-winds dynamics, or the Eta model was unable to provide adequate initial conditions. The latter hypothesis implies a sensitivity to the upstream conditions.

Downslope winds and mountain-waves are an important mesoscale phe-

nomenon routinely forecast in high-resolution NWP simulations. While early guidance suggests a predictability up to 24-hrs prior to the event, several studies have indicated that downslope-wind and mountain-wave predictions are very sensitive to the model formulation and physical parameterizations (e.g. Clark et al., 1994; Doyle et al., 2000). Furthermore, simulations of downslope winds and mountain waves frequently verify poorly against observations (e.g. Gohm et al., 2004; Garvert et al., 2007). Basic questions regarding the predictability of these events are generally unanswered. For example, what is the predictive time scale for downslope wind simulations, and, can consistent model biases result in poor mountain-wave forecasts and decreased predictability? Furthermore, the applicability of modern ensemble data assimilation in regions of complex terrain has not been explored. This thesis will investigate these questions and provide significant insight into the predictability of downslope winds and mountain waves.

The thesis is organized as follows. The rest of this chapter contains additional background material. In chapter 2 an analysis of discretization errors which lead to mountain-wave over-amplification in numerical models will be presented. The impact of these discretization errors on the predictability of mountain-waves and downslope winds will also be discussed. In chapter 3, a predictability experiment for downslope-wind forecasts will be presented. Chapter 4 contains an evaluation of the potential application of ensemble data assimilation in regions of complex terrain. Conclusions are presented in chapter 5.

1.2 Background

Significant advancements in the theoretical understanding of downslope winds have occurred over the past three decades and several pathways to strong downslope winds have been identified (Durran, 1990). One type occurs when

a large amplitude mountain wave breaks down and strong downslope winds form beneath the breaking region (Clark and Peltier, 1977; Peltier and Clark, 1979). Wave breaking can also lead to severe turbulence which can be a significant threat to aviation (Lilly, 1978; Nastrom and Fritts, 1992). A second type occurs when a layer of strong static stability is located underneath weak upper-tropospheric stability (Durran, 1986a). For this class of windstorms, wave breaking is not a dominant mechanism. This thesis does not intend to explore the dynamics of the processes leading to strong downslope winds, but instead to examine the predictability of the different types of downslope wind storms. Furthermore, the predictability of clear-air turbulence and mountain wave breaking will be investigated.

1.2.1 Forecasting Mountain Waves and Downslope Winds

Numerous studies have demonstrated that the numerical models can simulate realistic looking orographically generated flows. For example, Shutts (1992) was able to simulate orographically induced lee waves with a high-resolution numerical model. Based on comparisons between the model simulations and a handful of radiosonde profiles, they speculated that operational models would be capable of deterministically predicting mountain-waves and clear-air turbulence. In another example Clark et al. (1994) presented two- and three-dimensional simulations of a severe downslope windstorm in Boulder, CO. They found that while the model was able to predict a wind storm, it was not able to simulate the detailed evolution or location of the storm. Furthermore, the model solutions were strongly dependent on the formulation of the boundary layer scheme.

While the previous examples were limited in the sense that they were initialized with horizontally uniform soundings, full physics high-resolution NWP models with time dependent boundary conditions have also shown the ability to

simulate orographically induced phenomenon. In one example, Colle and Mass (1998) were able to successfully simulate a downslope wind event along the western slopes of the Washington Cascades. The model demonstrated its ability to realistically depict features such as upstream blocking, shooting downslope flow, and flow splitting around the Olympic mountains. In another example, Doyle and Shapiro (2000) demonstrated that the COAMPS model could realistically simulate a severe downslope wind event associated with the nonlinear amplification of a mountain wave due to the upstream layering of static-stability in a frontal boundary.

While the general qualitative success of these models is extensive, quantitative evaluation is difficult due to limited observations in complex terrain. However, Clark et al. (2000) compared LIDAR observations to model simulations of mountain-wave breaking associated with a Boulder, CO wind storm. They claimed that the model was able to accurately represent the wave-breaking region and the deterministic forecasts of clear-air turbulence associated with the wave breaking were feasible. The mesoscale alpine program (MAP) provided several opportunities to verify model simulation of mountain waves against observations. In general, it was difficult to obtain quantitatively accurate comparisons between model simulations of mountain waves during MAP and observations (e.g. Doyle et al., 2002; Volkert et al., 2003).

One persistent problem in both real-time and *a posteriori* forecasts is the tendency to over-predict the mountain-wave amplitude directly over the barrier. One possible consequence of mountain-wave over prediction is a greater tendency for waves to break down and generate severe downslope winds (e.g. Peltier and Clark, 1979). Additionally, excessive wave breaking in model forecasts can lead to inaccurate forecasts of clear-air turbulence. Real-time, *a prior*, forecasts of mountain-waves, used for mission planing during MAP, produced mountain waves with much larger amplitude than observed as well as frequent

wave breaking (Doyle 2008, personal communications). Furthermore, *a posteriori* simulations indicate that simulated waves in high resolution models were substantially stronger than observed (Doyle and Jiang, 2006). Mountain-wave over-prediction is not limited to the European Alps. Garvert et al. (2007) used horizontal winds derived from a dual-Doppler radar mounted on the NOAA P-3 aircraft to compare observations of a mountain-wave event over the Oregon Cascades to high-resolution model simulations. They found that the simulated mountain-wave amplitude was much stronger than observed.

1.2.2 Downslope Wind and Mountain Wave Sensitivities

While downslope winds are strongly forced by the underlying topography, simply specifying the terrain does not in general guarantee accurate forecasts. For example the removal of low-level stable layers upstream of mountain ranges can result in a large difference when simulating downslope winds (Durran, 1986a). Durran conducted a pair of idealized non-linear numerical simulations using a sounding from the 11 January, 1972 Boulder windstorm (Lilly and Zipser, 1972; Lilly, 1978). The sounding contained a region of high static stability near crest level and strong cross-barrier flow through the depth of the atmosphere. In the first simulation, a strong downslope wind response was apparent on the lee slope of the topography with a large amplitude mountain wave propagating away from the mountain. In the second simulation, the low-level stable layer was removed. As a consequence the downslope wind storm and large amplitude mountain wave did not develop in the model solution. While the modification to the initial sounding was relatively large, it provides an example of how variations in the upstream synoptic-scale flow can lead to large changes of the downslope wind response.

Several additional studies of the 11 January, 1972 Boulder windstorm have been conducted with idealized two-dimensional models. In order to verify that

high-resolution models could simulate upper-tropospheric and stratospheric wave breaking, Doyle et al. (2000) conducted a series numerical model intercomparisons in which 11 different models were initialized with the same upstream sounding from the Boulder windstorm. While all of the models were able to produce a region of wave breaking in the lower stratosphere, the temporal evolution of the breaking was significantly different between the individual models. Furthermore, both the downslope wind response and the upper-level wave breaking response were found to be very sensitive to small variations in the stratospheric profiles of wind speed and temperature.

In an effort to systematically evaluate mountain-wave and downslope wind sensitivities Doyle and Reynolds (2008) performed idealized, two-dimensional ensemble simulations using the same 11 January, 1972 Boulder windstorm sounding. Perturbations with magnitudes similar to radiosonde observational errors were added to the initial sounding in order to construct the ensemble. They found that for a linear response, forced by a small hill, weak error growth occurred and that the ensemble distribution was narrow. As the height of the hill increased and the flow became more non-linear, the error growth increased and the ensemble spread broadened. For non-linear flow, near the wave-breaking threshold, the ensemble spread was characterized by a bimodal distribution with half of the members simulating a large amplitude breaking wave in the stratosphere and the other half of the members simulating a trapped-wave response. Additionally, the downslope wind speed varied by over 25 m s^{-1} between the ensemble members.

Doyle et al. (2007) used an adjoint model to explore downslope-wind sensitivity in an idealized two-dimensional model. They found for smalls hills, in which the flow is linear and hydrostatic, the lee-slope winds are sensitive to perturbations in two lobes which extended upstream and above the topography. These two lobes represent downward propagating internal gravity waves.

For larger amplitude mountain waves, the sensitivity patterns were considerably more complex. Large sensitivities to middle tropospheric perturbations of potential temperature and wind speed 1-hr prior to the optimization time were found. This suggests that the predictive time scales of downslope winds could potentially be as short as 1-hr.

The predictability studies summarized above are limited to two dimensional simulations and are primarily focused on the 11 January, 1972 Boulder windstorm. The predictability limitations of downslope winds and mountain waves in fully three-dimensional NWP models has been largely unexplored. While it should be expected that the sensitivities associated with wave breaking, and described in Doyle and Reynolds (2008), are applicable in more complex models, this has not been fully explored. Furthermore, strong downslope winds can develop without wave breaking. For example, if the upstream profile is structured so that a layer of strong static stability is located beneath a layer of upper-tropospheric weak static stability then non-linear wave amplification can lead to strong winds (Durran, 1986a). The predictability of this type of event is unexplored.

Other predictability studies related to orography

Several authors of examined the predictability of orographic precipitation in cloud resolving models (Walser et al., 2004; Hohenegger et al., 2006). Hohenegger et al. looked at error growth in cloud-resolving numerical model simulations of several several orographic precipitation events during MAP. Using an small ensemble in which the synoptic-scale flow is assumed to be "perfectly predictable" by specifying identical lateral boundary conditions for each ensemble member, they proposed a mechanism based on the group velocity of gravity waves in which errors could grow in limited area models. They hypothesize that if the group velocity propagates upstream, then small errors on the meso-

scale will have the opportunity to grow before being advected out of the domain. These results, however, would be strongly dependent on the size of the numerical domain. Additionally, errors at inflow boundaries will always be present in limited-area model forecasts and should be accounted for when addressing the predictability of flows with strong synoptic dynamics.

Predictability of Moist Baroclinic Waves

In addition the the predictability of orographic flows, it has been shown that moist processes can significantly reduce the predictability of baroclinic waves in mesoscale models (Ehrendorfer et al., 1999; Zhang et al., 2002, 2003, 2007a). Ehrendorfer et al. (1999) used singular vectors to show that the inclusion of moist process increased the initial condition sensitivity in a situation of baroclinic instability compared to otherwise equal, but dry simulations. (Zhang et al., 2007a) showed that small initial errors in moist baroclinic flow can grow in three stages. In the first stage, rapid error growth occurs on the convective scale with error saturation occurring within 6-hrs. In the second stage, errors associated with the convective growth can project onto balanced motions leading to errors in the potential vorticity (PV) field. These PV perturbations project onto growing baroclinic modes which leads to a third stage of large scale baroclinic error growth.

1.2.3 Ensemble Data Assimilation

The EnKF is an ensemble based data assimilation method, which under suitable assumptions provides an optimal combination of observations and background estimates of the atmosphere (Evensen, 2003; Hamill, 2006). The background estimates are usually short-term model forecasts that were initialized with a previous EnKF assimilation cycle (e.g. Evensen, 1994). The short-term

forecasts are used to estimate the background error covariance statistics, $\mathbf{P}^b$. If $\mathbf{x}^b$ is a vector containing all model variables at all the grid points then $\mathbf{P}^b = \left\{\mathbf{x}^b \mathbf{x}^{bT}\right\}$, where the curly braces indicate that it is an expected value over the ensemble. The background error statistics are used to spread observational information around the model domain and update the short-term forecast to a new analysis state.

Several studies have demonstrated the benefit of using the EnKF for atmospheric applications. While the method was first limited to global models in which observations were drawn from the model solution (Houtekamer and Mitchell, 1998; Mitchell and Houtekamer, 2002), subsequent work has shown that the EnKF can be beneficial when using real-data observations (Houtekamer et al., 2005). The EnKF has also been adapted for mesoscale models (Zhang et al., 2006; Torn et al., 2006; Zhang et al., 2007b; Dirren et al., 2007; Torn and Hakim, 2008b). Torn and Hakim demonstrated that assimilating observations with the EnKF improved 6-hr forecasts up to 50% when compared to forecasts without data assimilation.

One issue with limited-area ensembles is the influence of the lateral boundaries on the ensemble variance. If deterministic boundaries are specified, the variance can artificially decrease over time. Torn et al. (2006) developed and tested several methods in which the boundary conditions could be perturbed for limited area models. They found a "fixed-covariance" perturbation method, in which the boundary perturbations were derived from a static covariance model, was particularly attractive.

Using limited area convective scale models, several authors have demonstrated that the EnKF is able to assimilate synthetic observations of radar reflectivities and velocities into an ideal model simulations of convective thunderstorms (Synder and Zhang, 2003; Zhang et al., 2004; Tong and Xue, 2005; Caya et al., 2005). Furthermore, Dowell et al. (2004) was able to assimilate

Doppler velocities and reflectivities of an observed tornadic supercell with an EnKF. While these studies have shown that the flow-dependent nature of the background-error covariances are beneficial when assimilating mesoscale observations, the improvement to subsequent forecasts is unclear. Furthermore, these high-resolution data-assimilation experiments are sensitive to the ensemble initiation procedure (e.g. Synder and Zhang, 2003; Zhang et al., 2004).

Orographic flows often exhibit a strong time tendency. Static background-error statistics derived from balance relations such as geostrophy or thermal-wind are not appropriate under such circumstances. Additionally, terrain-induced flows are often strongly dependent on larger scale motions and as such any data-assimilation system must account for this multi-scale aspect. In one example, Echevin et al. (2000) demonstrated that the flow-dependent background-error statistics from the EnKF produced more realistic analysis increments in a coastal ocean model with bottom topography than an OI scheme, however, the capability of flow-dependent statistics to capture mesoscale structures such as orographic blocking, mountain-waves, and downslope winds is unknown.

Several studies have demonstrated that data assimilation in complex terrain can improve the realism of short-term forecasts. For example, Doyle and Smith (2003) showed that cycling a forecast system with an optimal interpolation (OI) data assimilation step provided a more realistic representation of the horizontal wavelength of mountain-waves. Jaubert et al. (2005) used an OI system to assimilate in-situ temperature data in an alpine-valley cold pool into a high-resolution NWP simulation of a foëhn event. They found that the simulations initialized with the cold pool were able to better captured the evolution of the surface foëhn winds compared to the simulations without the cold pool. This thesis will explore the capability of the EnKF for data assimilation in complex terrain.

Chapter 2

GRAVITY WAVE OVER-AMPLIFICATION IN NUMERICAL SOLUTIONS TO FLOW OVER TOPOGRAPHY

The influence of numerical error on the mountain-wave amplitude is examined in this chapter. With the aid of linear theory it will be shown that numerical models with second-order-accurate advection and the common "C-grid" staggering (Mesinger and Arakawa, 1976) are not capable of accurately simulating waves forced by flow over a $10\Delta x$-wide obstacle. Davies and Brown (2001) investigated the minimum horizontal resolution need to accurately simulate hydrostatic flow over topography. The concluded that while models demonstrate appreciable skill for $6\Delta x$-wide features $10\Delta x$ was required for convergence. More generally, the impact of discretization errors across a wide range of hydrostatic and non-hydrostatic scales is investigated with a variety of numerical schemes on both a staggered and unstaggered meshes.

2.1 Discrete flow over topography

In this section the role of discretization errors in simulations of linear Boussinesq flow over an isolated two-dimensional barrier will be quantified by comparing discrete analytic mountain-wave solutions with the solution to the continuous problem. Klemp et al. (2003) computed discrete analytic mountain-wave solutions to demonstrate the need for consistent finite-differencing in domains with vertically transformed coordinates. Here, we compute similar analytic mountain-wave solutions to investigate the errors due to inadequate horizontal resolution in finite-difference models for flow over orography. We fo-

cus first on non-hydrostatic waves, which are more likely to be poorly resolved by operational mesoscale models and then consider the impact of discretization on hydrostatic waves.

2.1.1 The Discrete Boussinesq System

Consider a differential-difference approximation to the continuous Boussinesq system in which the spatial derivatives are computed with finite differences and the time derivatives are left in continuous form. As is common in many finite-difference NWP models, the unknown fields are defined on a "C-Grid", such that the perturbation pressure P and buoyancy b are co-located at the index point (p, q), while the perturbation horizontal momentum (u, v), and vertical momentum w, are staggered one-half grid point in the horizontal and vertical directions, respectively. Staggering the variables in this way allows the pressure gradient and divergence terms to be calculated on a numerical mesh with twice the resolution of the grid, leading to a better representation of the shortest resolvable gravity waves when compared to an unstaggered mesh. Further improvements to the numerical accuracy can be obtained by computing the horizontal advective terms with higher-order-accurate finite differences. We consider the impact on the discrete solution when the order of accuracy for the horizontal advective terms ranges from first- through sixth-order.

Assuming there are no y-direction variations, the semi-discrete Boussinesq system for flow with uniform background wind speed, U, Brunt-Väisälä frequency, N, and Coriolis parameter f, can be concisely expressed with the aid of operator notation as

$$\left.\frac{\partial u}{\partial t}\right|_{p-\frac{1}{2},q} + UD_{nx}u_{p-\frac{1}{2},q} - f\left\langle v_{p-\frac{1}{2},q}\right\rangle^{x} + \delta_x P_{p-\frac{1}{2},q} = 0 \tag{2.1}$$

$$\left.\frac{\partial v}{\partial t}\right|_{p,q} + UD_{nx}v_{p,q} + f\left\langle u_{p,q}\right\rangle^{x} = 0 \tag{2.2}$$

$$\left.\frac{\partial w}{\partial t}\right|_{p,q-\frac{1}{2}} + UD_{nx}w_{p,q-\frac{1}{2}} + \delta_z P_{p,q-\frac{1}{2}} = \left\langle b_{p,q-\frac{1}{2}} \right\rangle^z \tag{2.3}$$

$$\left.\frac{\partial b}{\partial t}\right|_{p,q} + UD_{nx}b_{p,q} + N^2 \left\langle w_{p,q} \right\rangle^z = 0 \tag{2.4}$$

$$\delta_x u_{p,q} + \delta_z w_{p,q} = 0. \tag{2.5}$$

Here, δ_x and δ_z are operators representing second-order centered finite differences in the horizontal and vertical directions with grid spacing $\Delta x/2$ and $\Delta z/2$, respectively. The operator D_{nx} is a n^{th}-order approximation to the first derivative with grid spacing Δx. Table 1 shows D_{nx} for first- through sixth-order differences as a function of the centered finite-difference operator

$$\delta_{nx} f(x) = \frac{f\left(x + \frac{n}{2}\Delta x\right) - f\left(x - \frac{n}{2}\Delta x\right)}{n\Delta x}. \tag{2.6}$$

Note that δ_x and δ_z are defined by (2.6) for the case of $n = 1$. In addition to the finite-difference operators, an averaging operator defined by

$$\left\langle f(x) \right\rangle^x = f\left(x + \frac{1}{2}\Delta x\right) + f\left(x - \frac{1}{2}\Delta x\right) \tag{2.7}$$

is used in (2.1)-(2.4).

Analogous to the familiar approach used with the continuous Boussinesq system, the semi-discrete dispersion relationship can be computed by substituting discrete plane-wave solutions of the form

$$\psi = \psi_0 e^{i(kp\Delta x + mq\Delta z - \omega t)} \tag{2.8}$$

into (2.1)-(2.5) and solving for ω (Durran, 1999). Here, the horizontal and vertical wavenumbers are given by k and m, respectively, while the frequency of the oscillation is given by ω. The exact formulation of the semi-discrete dispersion relationship depends on the order of accuracy in which the horizontal advective terms are computed, as well as the horizontal and vertical grid spacing, however, a generalized form can be written as

$$\omega = U\tilde{K}_n - \left(\frac{\tilde{N}^2\tilde{k}^2 + \tilde{f}^2\tilde{m}^2}{\tilde{k}^2 + \tilde{m}^2}\right)^{\frac{1}{2}}. \tag{2.9}$$

Table 2.1: The first- through sixth order discrete operator, D_{nx}, to the first derivative, as well as the discrete representation of the wavenumber associated with that finite difference approximation to a plane wave function.

n	D_{nx}	K_n
1	$\delta_{2x} - \frac{\Delta x}{2}\delta_x^2$	$\tilde{k}_2 + i\frac{[\cos(k\Delta x)-1]}{\Delta x}$
2	δ_{2x}	$\tilde{k}_2$
3	$\delta_{2x} - \frac{\Delta x^2}{6}\delta_x^2 D_{1x}$	$\frac{1}{3}(4\tilde{k}_2 - \tilde{k}_4) - \frac{i}{3}\frac{[\cos(k\Delta x)-1]^2}{\Delta x}$
4	$\left(1 - \frac{\Delta x^2}{6}\delta_x^2\right)\delta_{2x}$	$\frac{1}{3}(4\tilde{k}_2 - \tilde{k}_4)$
5	$\left(1 - \frac{\Delta x^2}{6}\delta_x^2\right)\delta_{2x} + \frac{\Delta x^4}{30}\delta_x^4 D_{1x}$	$\left(\frac{3}{2}\tilde{k}_2 - \frac{3}{5}\tilde{k}_4 + \frac{1}{10}\tilde{k}_6\right) + \frac{i}{15}\frac{[\cos(k\Delta x)-1]^3}{\Delta x}$
6	$\left(1 - \frac{\Delta x^2}{6}\delta_x^2 + \frac{\Delta x^4}{30}\delta_x^4\right)\delta_{2x}$	$\left(\frac{3}{2}\tilde{k}_2 - \frac{3}{5}\tilde{k}_4 + \frac{1}{10}\tilde{k}_6\right)$

Here $i\tilde{K}_n$, $i\tilde{k}$, and $i\tilde{m}$ are the eigenvalues associated with various finite difference operators in (2.1)-(2.5), such that

$$\tilde{k} = \frac{\sin\left(\frac{\Delta x}{2}k\right)}{\frac{\Delta x}{2}},\ \tilde{m} = \frac{\sin\left(\frac{\Delta z}{2}m\right)}{\frac{\Delta z}{2}}, \tag{2.10}$$

and $\tilde{K}_n$, the horizontal wavenumber associated with the approximation of the horizontal advection terms, is given in Table 1 as a function of

$$\tilde{k}_n = \frac{\sin\left(\frac{n}{2}\Delta x k\right)}{\frac{n}{2}\Delta x}. \tag{2.11}$$

The $\tilde{k}$ and $\tilde{m}$ terms arise from the δ_x and δ_z finite-difference operators associated with the pressure gradient and divergence terms in (2.1), (2.3), and (2.5). Apparent from the definition of $\tilde{k}_n$ is that $\tilde{k} = \tilde{k}_1$. Finally, $\tilde{N}$ and $\tilde{f}$ are associated with the averaging operators in (2.1)-(2.4) and are defined by

$$\tilde{N} = \cos\left(\frac{\Delta z}{2}m\right) \quad \text{and} \quad \tilde{f} = \cos\left(\frac{\Delta x}{2}k\right), \tag{2.12}$$

respectively. Note the similarity between the semi-discrete dispersion relationship (2.9) and the continuous dispersion relationship,

$$\omega_c = Uk \pm \left(\frac{N^2k^2 + f^2m^2}{k^2 + m^2}\right)^{\frac{1}{2}}. \tag{2.13}$$

In the limit of good horizontal and vertical resolution $\tilde{K}_n \to k$, $\tilde{k} \to k$, $\tilde{m} \to m$, $\tilde{N} \to N$, and $\tilde{f} \to f$ implying that $\omega \to \omega_c$.

2.1.2 Flow Over Topography

To investigate the effects of numerical errors in the discretized problem we must first consider the continuous case. Following Smith (1979) the vertical velocity for a single Fourier mode over an infinitely long ridge is

$$\hat{w}(k,z) = ikU\hat{h}(k)e^{imz}. \tag{2.14}$$

In the preceding $\hat{h}(k)$ is the Fourier transform of the topographic profile $h(x)$ and $\hat{w}$ is the transform of the vertical velocity. The vertical wavenumber m is obtained by setting $\omega_c = 0$ in (2.13) and solving the resulting equation to give

$$m^2 = k^2 \left[\left(\frac{N}{Uk} \right)^2 - 1 \right] \left[1 - \left(\frac{f}{Uk} \right)^2 \right]^{-1}. \tag{2.15}$$

Substituting for m in (2.14) and taking the inverse Fourier transform gives the vertical velocity w from which P, b, u, and v can be recovered from the polarization relations (Gill, 1982).

Non-dimensional parameters governing the mountain-wave structure may be defined as follows. Inspection of (2.15) reveals two relevant horizontal length scales, U/N and U/f. Vertical propagation is possible over the range $f/U < k < N/U$. Since $N/f \approx 100$ in mid-latitudes, the spatial scales of vertically propagating waves can vary by two orders of magnitude. If the horizontal scale of the topography is a then $\delta = Na/U$ is the non-dimensional mountain width and $R_o = U/(fa) \approx 100/\delta$ is the Rossby number. For $\delta = O(1)$ the response is dominated by non-hydrostatic motions and rotational effects are negligible. For $\delta = O(10)$, the wave motions are primarily hydrostatic and rotational effects only minimally modify the solution. As δ increases beyond 10, the influences of rotation must be considered.

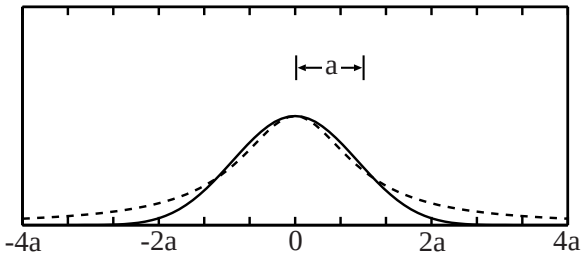

Figure 2.1: Topography given by (2.16), solid line, compared to a Witch of Agnesi with half-width a (dashed). The tick marks are plotted every $\frac{2}{3}a$ corresponding to the grid spacing for the examples in lines 1 and 2 of Table 2.

The terrain profile is specified as

$$h(x') = \begin{cases} \frac{h_0}{16}\left[1+\cos\left(\pi\frac{x}{4a}\right)\right]^4, & \text{if } |\frac{x}{4a}| \le 1; \\ 0, & \text{otherwise,} \end{cases} \tag{2.16}$$

which, as shown in Fig. 2.1, is similar to the widely used Witch of Agnesi except that it drops to zero at a finite distance (of $4a$) from the mountain crest. To compute $\hat{h}(k)$ from (2.16), a Fast Fourier transform (FFT) is used on a grid with 2048 points spaced $0.05a$ apart. The vertical velocity field is recovered by applying the inverse FFT to (2.14).

Figure 2.2 shows the vertical velocity in the continuous system for flow over $h(x)$ with $\delta = 1.8$. Consistent with the scaling arguments presented above, the impact of rotation is ignored by setting $f = 0$. The vertical velocity is normalized by Uh_0/a, which arises from (2.14) by setting the scale for k as a^{-1}. The x-axis has been normalized by the mountain half-width $x' = x/a$ and the z-axis has been normalized by the vertical wavelength of a two-dimensional hydrostatic mountain wave $z' = zN/(2\pi U)$. The non-hydrostatic nature of the flow is clearly evident in Fig. 2.2 as the wave is dispersive with a substantial amount of wave energy propagating both vertically and downstream (Durran, 1986b).

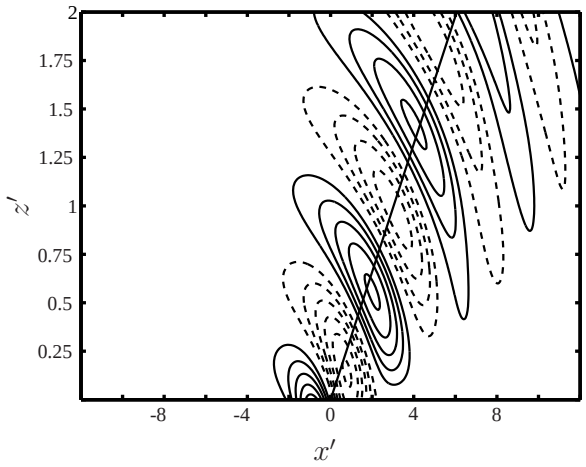

Figure 2.2: Non-dimensionalized vertical velocity for linear two-dimensional flow over an isolated ridge. The flow is non-hydrostatic with $\delta = 1.8$. The contour interval is 0.125 and the zero contour is omitted. A line that makes a 50° angle with the horizontal is plotted for reference.

Turning now to the discrete system, the vertical velocity is given by

$$\hat{w}(k, q\Delta z) = ikU\hat{h}(k)e^{im_n q\Delta z}. \tag{2.17}$$

Here m_n is the vertical wave number associated with the n^{th}-order finite difference scheme satisfying the steady version of (2.9). Setting $\omega = 0$ in (2.9) and using (2.10) and (2.12) the discrete vertical wavenumber is

$$m_n = \frac{2}{\Delta z}\cos^{-1}\left\{\sqrt{\frac{\left(\Delta z\tilde{k}\right)^2 + 4 - \left(2\tilde{R}_n\right)^2}{\left(\tilde{k}\frac{N}{U}\frac{\Delta z}{\tilde{K}_n}\right)^2 + 4 - \left(2\tilde{R}_n\right)^2}}\right\}, \tag{2.18}$$

where $\tilde{R}_n = \tilde{f}/\left(U\tilde{K}_n\right)$. The discrete linear solutions are obtained using Fourier transforms in an identical manner as the continuous case with one exception: $h(x)$ is defined on a horizontal grid with spacing Δx.

To appreciate the errors that may occur when computing approximations to the solution in Fig. 2.2, suppose the non-dimensional horizontal and vertical grid intervals used to evaluate the discrete solutions are $\Delta x' = \Delta x/a = 0.67$

Table 2.2: Illustrative physical parameters for the three mountain-wave solutions considered assuming the background wind speed and Brunt-Väisälä frequency are $U = 25$ m s^{-1} and $N = 0.01$ s^{-1}, respectively.

δ	a (km)	f (s^{-1})	Δx (km)	Δz (km)
1.8	4.5	0	3.0	0.75
10	25	10^{-4}	16.7	0.75
10	25	10^{-4}	33.6	0.75

and $\Delta z' = \Delta z N/(2\pi U) = 0.048$. Figure 2.1 shows the horizontal grid point spacing in relation to the topographic profile and indicates that the barrier is resolved by roughly 8 grid points. A concrete example of one representative set of dimensional parameters corresponding to this case is listed in the first row of Table 2. Note that the high vertical resolution makes the solutions relatively insensitive to moderate variation in $\Delta z'$.

The normalized vertical velocity forced by the topographic profile (2.16) is shown for first- through sixth-order schemes in Fig. 2.3. It is not surprising that the well-known diffusive nature of the first-order scheme (Fig. 2.3a) produces excessive damping of the mountain-wave solution. The large errors of the second-order scheme (Fig. 2.3b) for flow over the $8\Delta x$-wide mountain were however, unexpected. Considering the maximum vertical velocity within the first positive phase of the wave (from $z' = 0.25$ to $z' = 1.0$), the second-order solution is 30% stronger than the corresponding continuous solution. This is a direct result of the second-order scheme being unable to adequately resolve waves forced by the $8\Delta x$ topography. In addition, the morphological behavior of the second-order solution is substantially different from the continuous solution. The second-order solution does not correctly capture the downstream propagation evident in the continuous solution. Instead, the majority of wave

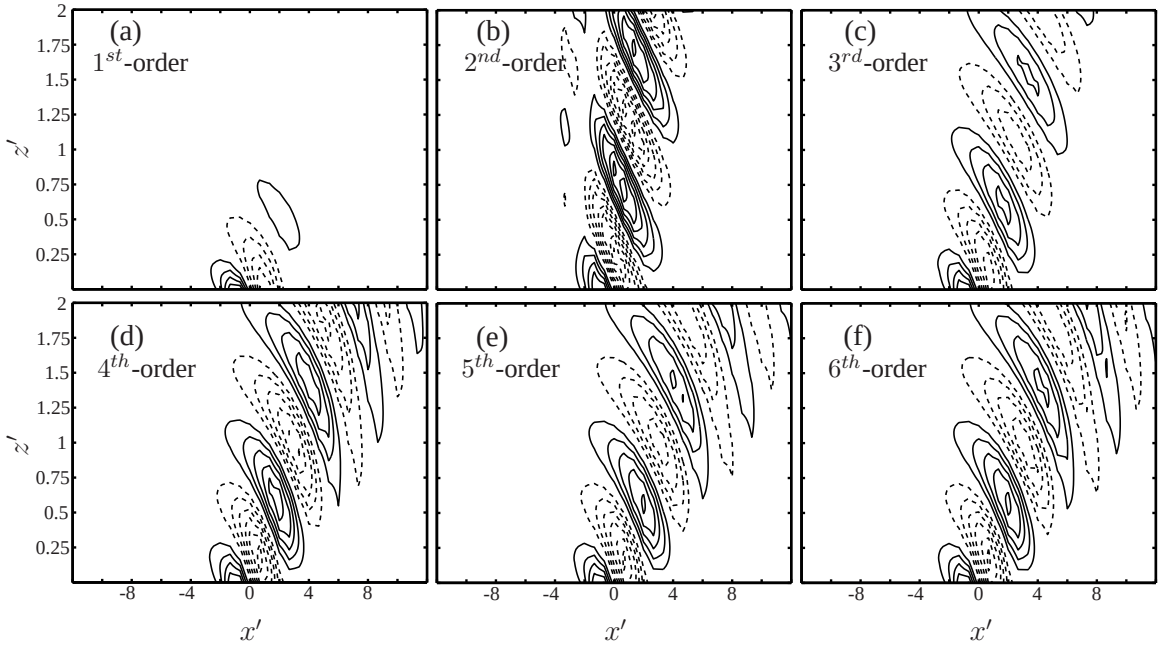

Figure 2.3: The non-dimensional vertical velocity for the discrete solution to linear non-hydrostatic ($\delta = 1.8$) Boussinesq flow over an isolated ridge for (a) first-, (b) second-, (c) third-, (d) fourth-, (e) fifth-, and (f) sixth-order-advection schemes. The horizontal grid spacing is $\Delta x' = 0.67$ resulting in 8 grid points across the ridge. The contour interval is 0.125 and the zero contour is omitted.

energy is found directly over the crest of the topography, as would be expected in a hydrostatic mountain wave.

Increasing the order-of-accuracy of the advective scheme improves the morphological behavior of the mountain wave and reduces the magnitude of the errors in the vertical velocity. For example, the third-order scheme more faithfully represents downstream wave propagation (Fig. 2.3c), however, the implicit numerical diffusion in the third-order approximation removes too much energy from the shortest wavelengths. Downstream propagation is clearly evident in the solution obtained using the fourth-order scheme (Fig. 2.3d), however, similar to the second-order solution, the vertical velocity amplitude in the first phase of the wave is over-predicted by 11%. The two best performing numerical

methods are the fifth and sixth-order schemes (Figs. 2.3e and f, respectively). In both of these solutions the downstream energy propagation evident in the continuous solution is present. Additionally, the vertical velocity amplitude within the first phase of the wave compares well with the continuous solution. The fifth and sixth-order schemes are respectively, 1% and 4% stronger than the corresponding continuous solutions. It is interesting that despite the numerical diffusion associated with the fifth-order solution, the wave amplitude is stronger than the continuous solution.

We now consider the discretization impact on hydrostatic mountain waves. Figure 2.4a shows the normalized vertical velocity in the continuous Boussinesq system for $\delta = 10$. The influence of the Coriolis force is included in the solution, however, the impacts are minimal since the Rossby number is relatively large ($R_o = 10$). As expected, the majority of wave energy is located directly over the mountain crest and the phase-lines tilt upstream with height (e.g. Smith, 1979). The second-order discrete solution for flow over an $8\Delta x$ wide mountain when $\Delta x' = 0.67$ and $\Delta z' = 0.048$ is shown in Fig. 2.4b. Note that the waves propagate upstream and the vertical-velocity amplitude is decreased over the mountain crest by 7% relative to that in the continuous solution. Representative dimensional parameters for this problem are given on line 2 of Table 2 and are typical of the resolutions used in operational NWP forecasts. The grid-point locations relative to the mountain are shown in Fig. 2.1 and are identical to those in the previously considered $\delta = 1.8$ case.

A less-well-resolved case is shown in Fig. 2.4c, in which the normalized horizontal resolution is $\Delta x' = 1.35$, corresponding to slightly more than four grid-points spanning the mountain barrier. A $4\Delta x$ wavelength feature is often accepted as being adequately resolved (Grasso, 2000). Line 3 of Table 2 gives the dimensional parameters for an illustrative example that would map to this case. Clearly the wave structure is grossly distorted; a substantial amount

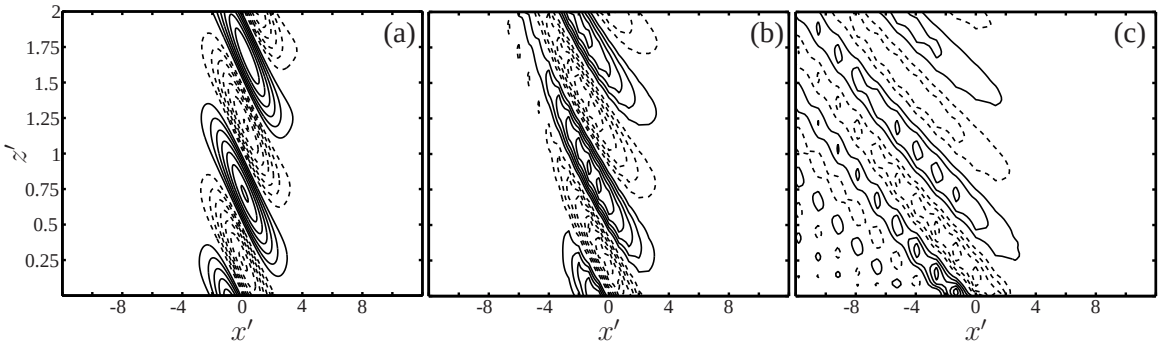

Figure 2.4: The non-dimensional vertical velocity when $\delta = 10$ and $Ro = 10$ for the (a) continuous solution as well as second-order solutions with (b) $\Delta x' = 0.67$, and (c) $\Delta x' = 1.35$. The contour interval is 0.125 and the zero contour is omitted.

of wave-energy is propagating upstream and the magnitude of the vertically propagating wave is significantly reduced. The maximum vertical velocity in the first phase of the wave is 39% lower than the corresponding continuous solution.

2.1.3 Pressure Drag

One important quantity related to mountain waves is the pressure drag across the mountain barrier. This drag can be large enough to significantly alter the general circulation of the atmosphere (e.g. Bretherton, 1969) and must be accounted for in global models which do not explicitly resolve the topography (Palmer et al., 1986; McFarlane, 1987). In this section the pressure drag in the discrete solution is compared to the drag in the continuous solution.

The drag for the second- and fourth-order discrete solutions, normalized by the continuous drag, is shown as a function of the non-hydrostatic parameter δ in Fig. 2.5. Consistent with the examples shown in Figs. 2.3 and 2.4b, the horizontal resolution for the discrete solution is fixed at $\Delta x' = 0.67a$. For non-hydrostatic flow ($\delta < 3$), the drag in the second-order scheme is more than 25%

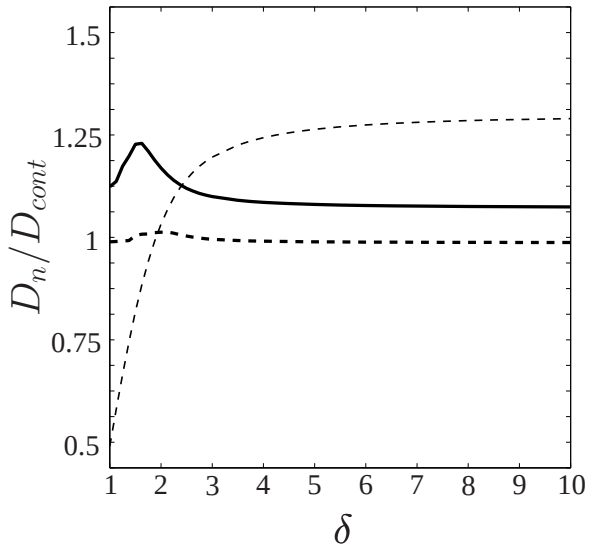

Figure 2.5: The pressure drag as a function of the non-hydrostatic parameter δ for the second-order (solid) and fourth-order (thick dashed) schemes where the horizontal resolution is $\Delta x' = 0.67a$. The pressure drags have been normalized by the drag for the continuous solution. Also plotted is the continuous pressure drag (thin dashed) normalized by the pressure drag for hydrostatic linear flow over a Witch of Agnesi profile.

larger than the continuous drag, while for the hydrostatic waves ($\delta > 5$) it is close to 5% larger. Figure 2.5 also shows the continuous drag, normalized by the drag for linear hydrostatic flow over a Witch of Agnesi profile. Although the overprediction by the second-order scheme is large for the non-hydrostatic waves, it is not particularly alarming because the continuous drag is relatively weak for these wavelengths. However, for the hydrostatic waves, where the continuous drag is relatively large, the overprediction represents an excessive force on the atmosphere that may need to be accounted for when formulating drag parameterizations for grid-point mesoscale and global models. Consistent with the improvement of the discrete mountain wave solutions for the fourth-order scheme, the drag calculations are significantly improved and are very close to the continuous drag.

2.2 Group Velocity Analysis

The differences between the mountain-wave solutions in the continuous and discrete systems can be understood by comparing the group velocities for each system. First, we consider group velocities for wavelengths associated with the non-hydrostatic mountain waves shown in Figs. 2.2 and 2.3. Then, the impact of numerical errors on the group velocity across a wide range of horizontal scales and numerical resolutions is investigated by considering the angle the group velocity vector makes with the horizontal plane. Finally, the influence of grid staggering on group-velocity errors is explored.

2.2.1 Continuous and Discrete Group Velocities

In the continuous case, the horizontal and vertical components of the group-velocity vector $\mathbf{c}_g$ are

$$c_{gx} = U - \frac{km^2\left(N^2 - f^2\right)}{\left(k^2 + m^2\right)^{\frac{3}{2}}\left(N^2k^2 + f^2m^2\right)^{\frac{1}{2}}} \tag{2.19}$$

and

$$c_{gz} = \frac{k^2 m \left(N^2 - f^2\right)}{\left(k^2 + m^2\right)^{\frac{3}{2}} \left(N^2 k^2 + f^2 m^2\right)^{\frac{1}{2}}}. \tag{2.20}$$

While $\mathbf{c}_g$ admits both steady and non-steady motions, attention is restricted to steady flow by requiring m to satisfy (2.15). The horizontal and vertical components of the continuous group velocity for steady flow are plotted (using solid lines) in Figs. 2.6a and b as functions of the normalized horizontal wavelength $\lambda_x' = \lambda_x N/(2\pi U)$. For decreasing λ_x' the influence of non-hydrostatic motions become important as evident by the increasing amount of downstream propagating wave energy in Fig. 2.6a. Near the non-hydrostatic cut-off of $\lambda_x' = 1$, c_{gz} drops rapidly to 0 and c_{gx} increases to 1; the majority of wave energy at these short horizontal scales is propagating downstream.

In the context of the continuous non-hydrostatic mountain-wave solution (Fig. 2.2), the range of λ_x' presented in Figs. 2.6a and b contains most of the power forced by the $\delta = 1.8$ mountain. For example, Fourier analysis of the vertical velocity field in the non-hydrostatic mountain wave shows the dominant horizontal wavelength is $\lambda_x' = 1.55$. From Fig. 2.6, $\mathbf{c}_g = (1.04U, 1.23U)$ for this wave implying that the group-velocity vector makes an angle of $\theta \approx 50^\circ$ with the horizontal plane. The dashed line in Fig. 2.2 is drawn at an angle of $\theta = 50^\circ$ showing that the majority of wave energy propagates downstream at this angle.

Now consider the effect of discretization on the group-velocity vector. In an analogous manner to the continuous system, the discrete steady version of $\mathbf{c}_g$ can be derived by differentiating (2.9) with respect to k and m and substituting (2.18) for m into the resulting two equations. The steady-state horizontal and vertical discrete group velocities are plotted in Figs. 2.6a and b for the second, fourth, and sixth-order numerical schemes. The odd-order schemes are not plotted since their group velocities are identical to those for the next higher

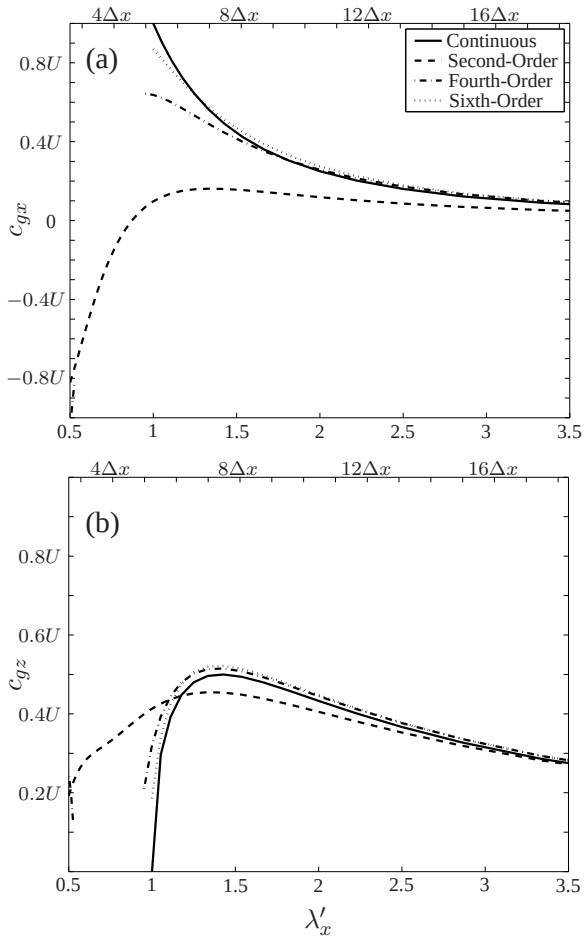

Figure 2.6: The discrete group velocities in the (a) horizontal and (b) vertical directions as a function of the normalized horizontal wavelength. The top label indicates the number of points resolving λ'_x. The grid spacing corresponds to the example given in the first line of Table 2.

even-order schemes. The number of grid-points-per-wavelength indicated along the top axis of both panels corresponds to the numerical resolution of the waves forced by the topography in Fig. 2.3.

As evident in Fig. 2.6, the second-order scheme is unable to accurately approximate the correct non-hydrostatic group velocities for any value of λ_x' between 0.5 and 2.5. The downstream component of the group velocity is significantly reduced compared to the continuous system and there is a non-trivial vertical component of the group velocity for wavelengths which would be evanescent in the continuous system ($\lambda_x' < 1$). These errors in the group velocity lead to an accumulation of wave energy over the topography resulting in over-amplification of the vertically propagating wave (Fig. 2.3b). In contrast, at the same wavelengths the fourth and sixth-order schemes more faithfully represent the downstream propagation of $\mathbf{c}_g$. However, the shortest non-hydrostatic waves are still poorly represented by the fourth-order advection scheme and as a result c_{gx} is retarded at these wavelengths. The sixth-order scheme performs well, even at the shortest horizontal wavelengths.

2.2.2 Angle of Propagation

While the preceding analysis was particular to the grid spacing used to approximate the non-hydrostatic mountain waves shown in Figs. 2.2 and 2.3, it can be concisely extended to a wide range of horizontal scales and numerical resolutions by considering the angle θ that the discrete group-velocity vector makes with the horizontal plane. Figure 2.7 shows contour plots of θ for a steady internal gravity wave as a function of the normalized horizontal wavelength λ_x' and the number of grid-points-per-wavelength $\lambda_x/\Delta x$. In order to clearly display θ across a wide range of horizontal scales λ_x' has been plotted on a logarithmic axis. While the contour plots are independent of any particular mountain geometry, each δ can be associated with a particular λ_x' through the maximally

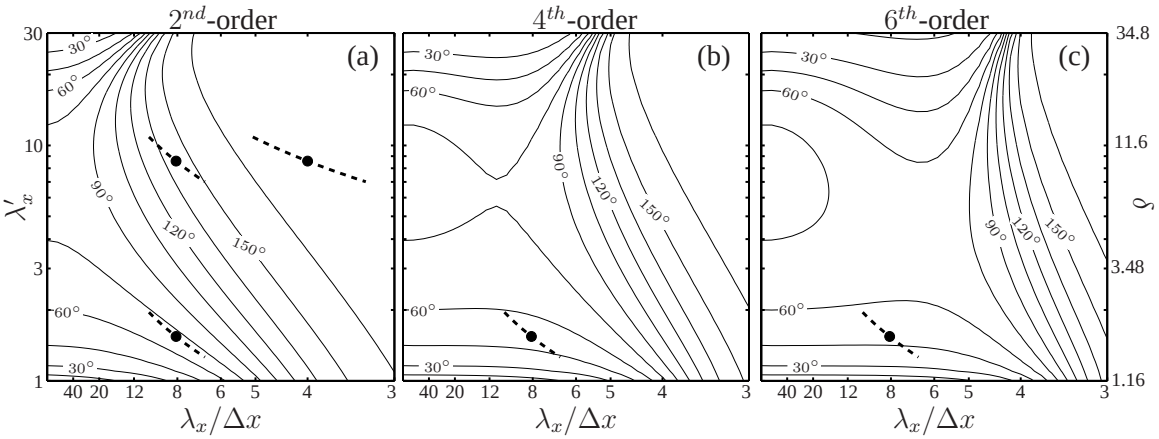

Figure 2.7: The discrete angle of propagation for the (a) second-, (b) fourth-, and (c) sixth-order schemes as a function of the normalized horizontal wavelength and the number of points-per-wavelength. The dots represent the location in the parameter space of the dominantly forced wavelength in the three mountain-wave solutions considered in Table 2. The dashed curves represent a slice through the parameter space where 90% of the wave energy is forced in the mountain-wave solutions. The value of the non-hydrostatic parameter δ for the maximally forced wavelength is shown on the right-hand axis.

forced horizontal wavelength in the vertical velocity field for that particular δ. The right-hand axis show the non-dimensional mountain width δ for which λ'_x is the horizontal wavelength at the peak of the vertical velocity spectrum forced by the mountain profile (2.16).

In the continuous limit $\lambda_x/\Delta x \to \infty$ (left edge of each plot in Fig. 2.7), the group-velocity vector points downstream for the shorter non-hydrostatic wavelengths and points increasingly towards the vertical as λ'_x approaches 10. However, as λ'_x exceeds 10, Coriolis effects become important and the group-velocity vector again tilts downstream. The impact of discretization on a particular monochromatic wave can be seen by moving from left to right in each plot. As the horizontal resolution decreases, the errors in θ increase. For example, for the second-order scheme (Fig. 2.7a) decreasing the number of grid points per

wavelength of the $\lambda'_x = 5$ wave leads to the vector pointing increasingly upstream such that when the wave is resolved by 8 grid points, $\theta \approx 125^\circ$ instead of the correct value of $\theta \approx 78^\circ$. The errors in the second-order scheme grow more rapidly than those of the fourth and sixth-order schemes with decreasing horizontal resolution, as evidenced by the greater horizontal extent of θ contours from the left edge of Figs. 2.7b and c.

The approximate locations in this parameter space of the three discrete mountain-wave cases shown in Figs. 2.3 and 2.4 are indicated by the black dots and dashed lines in Fig. 2.7. The black dots are plotted at the wavelength and spatial resolution at which the vertical velocity is maximally forced, and the dashed lines are the locus of all such points containing 90% of the power in the vertical velocity spectrum forced by each mountain. For the second-order non-hydrostatic mountain-wave solution (Fig. 2.7a) the group velocities are oriented too vertically ($\theta > 70^\circ$) for all wavelengths within 90% of the maximum forcing. For example, at the dominant horizontal wavelength ($\lambda'_x = 1.55$), $\theta = 71^\circ$ in the second-order scheme, compared to 50° in the continuous solution. In this case the horizontal resolution is inadequate, and as a result the energy in these non-hydrostatic modes propagates vertically instead of downstream, leading to an over amplification of the mountain wave directly above the topography. Higher-order schemes provide more accurate representations of the topographically forced vertical velocity spectrum; for $\lambda'_x = 1.55$, $\theta = 53^\circ$ for the fourth-order scheme (Fig. 2.7b) and 50° (the correct value) for the sixth-order scheme (Fig. 2.7c).

Turning now to the discrete solutions for the hydrostatic mountain waves, $\delta = 10$, the parametric points of the maximally forced wavelength in the vertical velocity spectrum ($\lambda'_x = 8.63$) yields an angle of $\theta = 142^\circ$ for the $8\Delta x$-wide mountain and $\theta = 174^\circ$ for the $4\Delta x$-wide mountain compared to $\theta = 80^\circ$ in the continuous system. Additionally, the 90% threshold for the vertical velocity

spectrum spans a wide range of propagation angles leading to the dispersive nature of the discrete hydrostatic mountain waves and the upstream propagation observed in Figs. 2.4b and c.

2.2.3 Higher-order Finite-Differences on the Staggered Mesh

The numerical errors in the preceding are exacerbated by the use of the staggered "C-grid". Inspection of Fig. 2.7 reveals that at intermediate resolution (6-12 points-per-wave) the sixth-order-scheme often generates larger errors than the fourth-order-scheme, especially at hydrostatic wavelengths. For example, at $\lambda_x' = 10$ with 8 points-per-wave resolution, $\theta = 76^\circ$ for the fourth-order scheme and $\theta = 59^\circ$ for the sixth-order scheme, compared to $\theta = 79^\circ$ in the continuous solution. One way to improve the solution obtained using sixth-order advection is to employ a fourth-order approximation of the derivatives on the staggered mesh,

$$\frac{\partial f}{\partial x} = \left(\frac{9}{8}\delta_x - \frac{1}{8}\delta_{3x}\right) f + O\left(\Delta x^4\right). \tag{2.21}$$

Figure 2.8 shows θ obtained when (2.21) is used to compute the pressure gradient in (2.1) and the horizontal divergence in (2.5) in combination with fourth or sixth-order advection (the 4-4 and 6-4 schemes, respectively). The increased accuracy of the 6-4 scheme is evident as the horizontal extent of θ contours from the left-axis is much greater than the 6-2 scheme. Considering the same parametric location as above, a nearly correct value of $\theta = 80^\circ$ is given by the 6-4 scheme.

The source of the errors in θ can be partially understood by considering how inconsistencies between $\tilde{K}_n$ and $\tilde{k}$ influence the downstream component of group velocity. In the limit of good vertical resolution, the discrete horizontal group velocity for hydrostatic, non-rotating flow is

$$\tilde{c}_{gx} = U\tilde{K}_n \frac{\partial}{\partial k}\left[\log\left(\frac{\tilde{K}_n}{\tilde{k}}\right)\right] \approx U\tilde{K}_n \frac{\partial}{\partial k}\left(\frac{\tilde{K}_n}{\tilde{k}}\right). \tag{2.22}$$

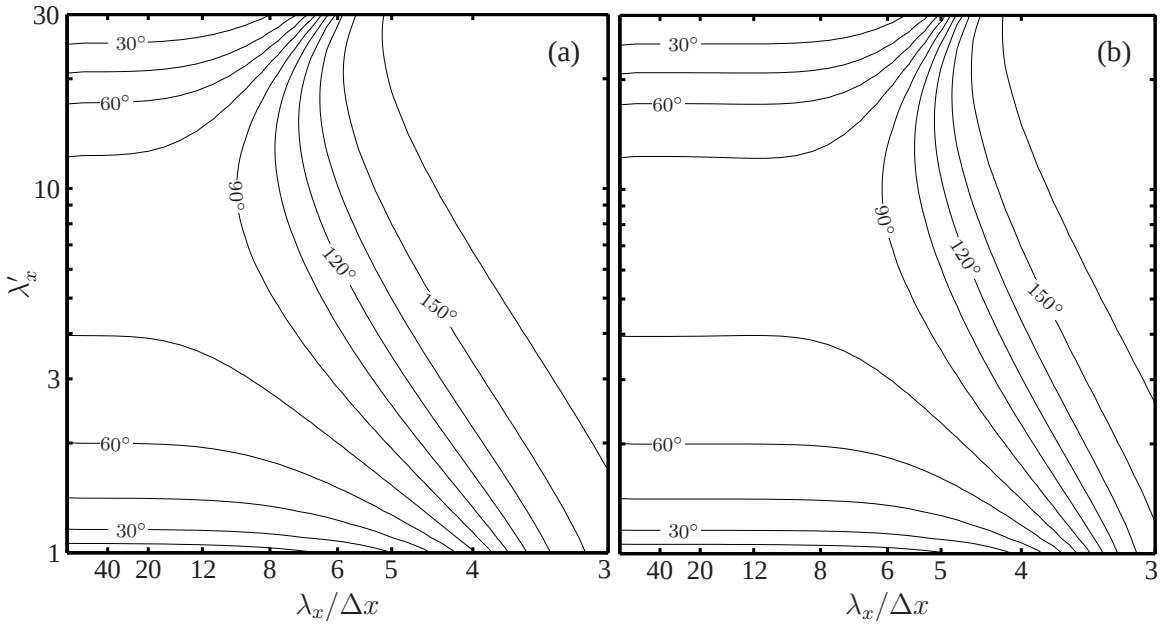

Figure 2.8: The discrete group-velocity angle for (a) fourth- and (b) sixth-order horizontal advection schemes when the horizontal pressure gradient and divergence terms are computed with a fourth-order finite difference.

Errors in $\tilde{c}_{gx}$ arise when $\tilde{K}_n$ and $\tilde{k}$ are different functions of the true horizontal wave number k, as will always be the case on staggered meshes. At very fine resolutions $\tilde{K}_n/\tilde{k}\rightarrow 1$ and $\tilde{c}_{gx} \rightarrow c_{gx} = 0$, however, at intermediate resolutions, small differences in the dependence of $\tilde{K}_n$ and $\tilde{k}$ on k can lead to large errors in $\tilde{c}_{gx}$. Figure 2.9 shows the ratio between $\tilde{K}_n$ and $\tilde{k}$ for the previously consider finite-difference combinations.[1] From (2.22) errors in $\tilde{c}_{gx}$, and thus θ, are large where the slope of $\tilde{K}_n/\tilde{k}$ is steep and small where the slope is shallow. As a result of the larger differences between $\tilde{K}_6$ and $\tilde{k}$, in the hydrostatic non-rotating limit, the errors in the 6-2 scheme are larger than the errors in the 4-2 scheme. As evident in Fig. 2.9, the 6-4 scheme gives a more consistent representation of $\tilde{K}_6$ and $\tilde{k}$ over a wide range of horizontal resolutions.

[1]For the 6-4 and 4-4 schemes $\tilde{k} = \left(\frac{9}{8}\tilde{k}_1 - \frac{1}{8}\tilde{k}_3\right)$.

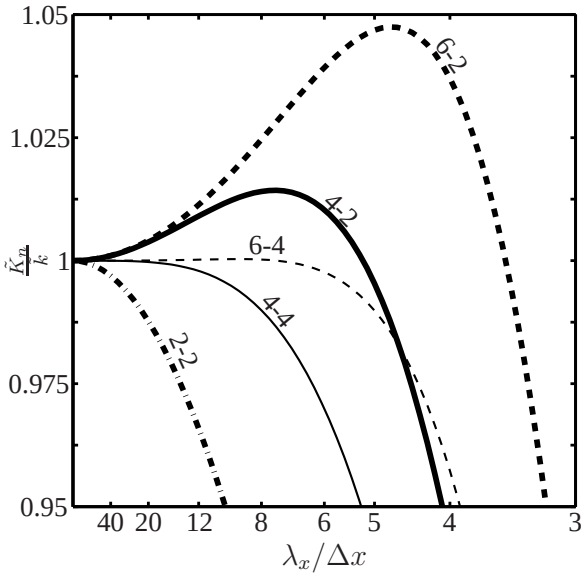

Figure 2.9: The relative difference between $\tilde{K_n}$ and $\tilde{k}$ for the 2-2 scheme (thick dash-dot), 4-2 scheme (thick solid), 6-2 scheme (thick dashed), 4-4 scheme (thin solid), and 6-4 scheme (thin dashed).

2.2.4 Unstaggered Meshes

In light of Fig. 2.9 and (2.22) one could conceivably improve the discrete group velocity by using unstaggered meshes. Figure 2.10 shows θ computed on an unstaggered mesh for second and fourth-order finite differences. At hydrostatic wavelengths ($\lambda_x' > 10$) the θ contours extend horizontally over a wider range of resolution compared to the 2-2 and 4-4 schemes on the staggered mesh (Figs 2.7ab). Additionally, no wave energy propagates upstream for $\lambda_x/\Delta x > 4$. The most notable improvement occurs with the 2-2 scheme; for the previously considered $8\Delta x$-wide wave associated with the hydrostatic mountain-wave case ($\lambda_x' = 8.63$), $\theta = 82^\circ$, which may be compared to 142° on the staggered mesh and 80° in the continuous system.

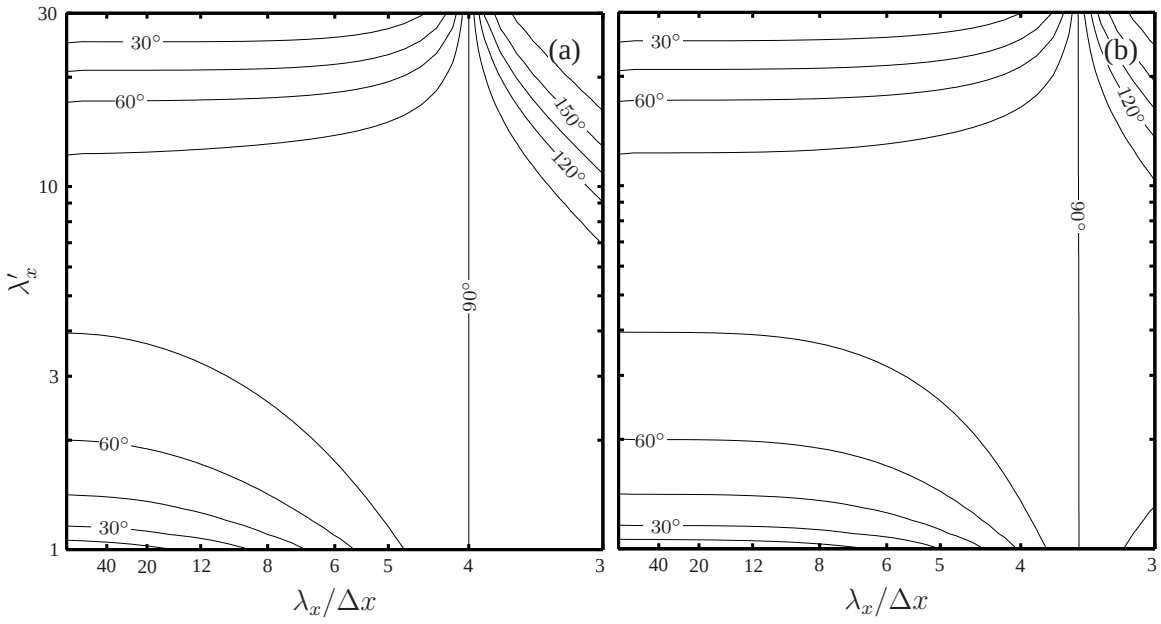

Figure 2.10: The group-velocity-vector angle on an unstaggered mesh for (a) second- and (b) fourth-order finite differences.

2.3 Case study with the COAMPS model

In this section an example of the tendency for poorly resolved, non-hydrostatic modes to over-amplify mountain waves will be given in the context of a 70 member, fully non-linear, mesoscale NWP ensemble system.

2.3.1 Non-linear numerical model

Numerical simulations of a mountain wave event were computed using the atmospheric portion of the Coupled Ocean-Atmosphere Mesoscale Prediction System (COAMPS^{TM}; Hodur, 1997). COAMPS solves a finite difference approximation to the fully compressible, non-linear, non-hydrostatic equations of motion on a terrain-following vertical coordinate system. As with the linear Boussinesq system presented above, the model variables are staggered on an "C-grid". The metric terms are computed in an internally consistent man-

ner as discussed in Klemp et al. (2003). With the exception of the horizontal advective terms, the spatial derivatives are approximated with centered second-order finite-differences. An option exists within COAMPS to compute the horizontal advective terms with either second-order or fourth-order centered finite-differences. One-way nests are used for all experiments described below. A more detailed description of the COAMPS numerical setup can be found in appendix A.

2.3.2 Experimental Setup

The model is used to create a 70 member ensemble hindcast of the flow over the Sierra-Nevada mountains on 16-17 April, 2006, a period when strong mountain waves were forecast operationally during IOP-13 in the Terrain-Induced Rotor Experiment (TREX; Grubišić et al., 2008). In order to explicitly resolve the scales of motion associated with mountain waves, three one-way nests with increasing horizontal resolution are used. Figure 2.11a shows the location and topography on the three nests. The outer-most domain has a horizontal resolution of 27 km and covers a large region of the Western North American Continent and Eastern Pacific Ocean. An intermediate size domain with 9 km resolution encompasses the entire north-south extent of the Sierra-Nevada Mountain range. A smaller domain with 3 km horizontal resolution is placed over the highest portion of the Sierra-Nevada Mountains as well as regions immediately upstream and downstream of the mountain range. In the experiments described below the large time step is 3.3 s on the 3 km domain and increases by a factor of 3 for each larger domain. The topography on the 3 km domain is shown in Fig. 2.11b. The vertical relief between the mean crest of the Sierra-Nevada and the Owens Valley directly to the east is greater than 2 km.

Initial conditions on 00 UTC, 17 April, 2006 for the 70-member ensemble are provided by an ensemble Kalman filter (EnKF). Unless otherwise noted,

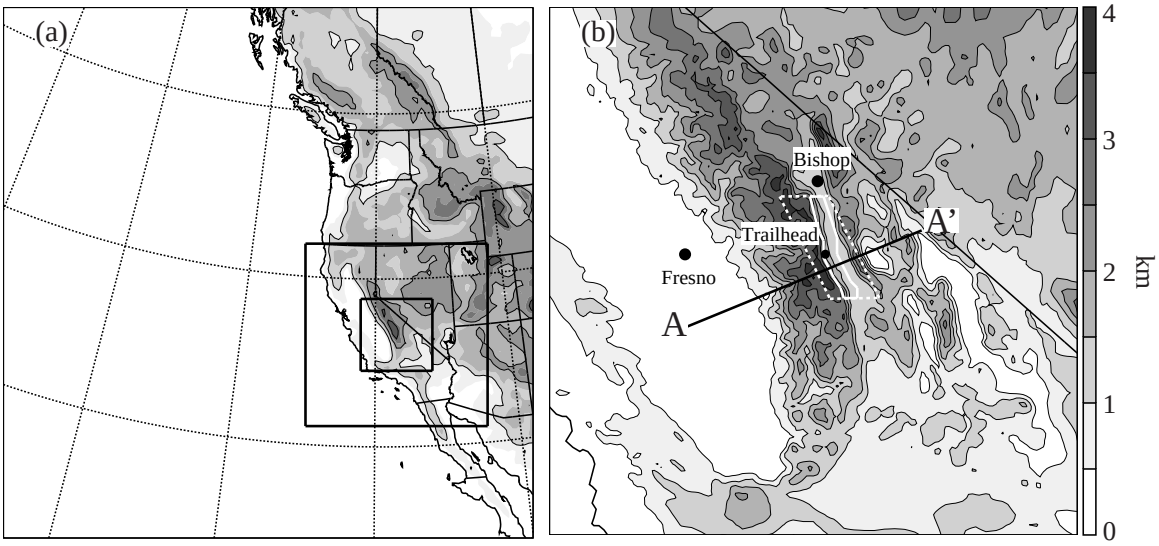

Figure 2.11: Location and topography of the (a) 27, 9, and 3 km COAMPS domains as well as the (b) topography and cross-section location on the 3 km domain. The solid and dashed white lines in (b) indicate the spatial extent over which the respective downslope wind metric and minimum flow aloft metric are computed.

all times are given in reference to this initial time. The EnKF approach was adopted for two reasons. First, data assimilation using an EnKF provides an optimal combination of observations and model background states (Hamill, 2006, appendix B). Second, an EnKF provides a natural way to generate ensemble forecasts which can be used to ascertain probabilistic forecast information.

On the 27-km domain, the EnKF is cycled over the duration of the entire TREX field campaign as described in appendix C. The 9- and 3-km domains are initialized several assimilation cycles prior to the 00 UTC forecast. During the spin-up time, data assimilation is performed on the the higher resolution domains every 6-hrs. The same set of observations used for assimilation on the 27-km domain are used for the 9- and 3-km domains. The boundaries of the 9- and 3-km domains are updated every time step from the parent ensemble

member. Prior to the 00 UTC forecast, second-order horizontal advection is used on all three domains. For the 00 UTC forecast the horizontal advection on the two outer domains remains second-order, however, the advection on the 3-km domain is computed with either second-order and fourth-order schemes. The initial conditions for each experiment, as well as the flow on the 27- and 9-km domains are identical.

2.3.3 Model Simulations

The 00 UTC ensemble mean analysis and 06 UTC ensemble mean forecast of the 500 hPa geopotential height field and wind speeds on the 27 km domain are plotted in Fig. 2.12. At the analysis time (Fig. 2.12a) a low-pressure trough is located just off-shore of the Western United States. Associated with the low-pressure trough is a jet extending around the base of the trough and into the central portion of California. The wind speeds within the jet exceed 40 m s^{-1} at 500 hPa. Six-hours later (Fig. 2.12b) the trough has moved on-shore and the associated jet-max is interacting with the central and southern portion of the Sierra-Nevada Mountains. This synoptic-scale flow regime is conductive to the formation of mountain waves and downslope winds within the Owens Valley.

A vertical cross-section of the six-hour ensemble mean forecast of w and θ above the transect indicated in Fig. 2.11b is plotted in Fig. 2.13 using data from the 3-km-resolution mesh. The second-order solution (Fig. 2.13a) shows a large-amplitude mountain wave anchored to the Sierra crest. The vertical velocities in the ensemble mean exceed 18 m s^{-1} through a large depth of the troposphere. However, the ensemble variability of vertical velocity is very large within the mountain wave. The maximum upward motions range from 6 m s^{-1} in the weakest ensemble member to 28 m s^{-1} in the strongest member. The large amplitude mountain wave is also apparent in the potential temperature field. For example, the 320 K isentrope is depressed nearly 2.5 km on the lee-

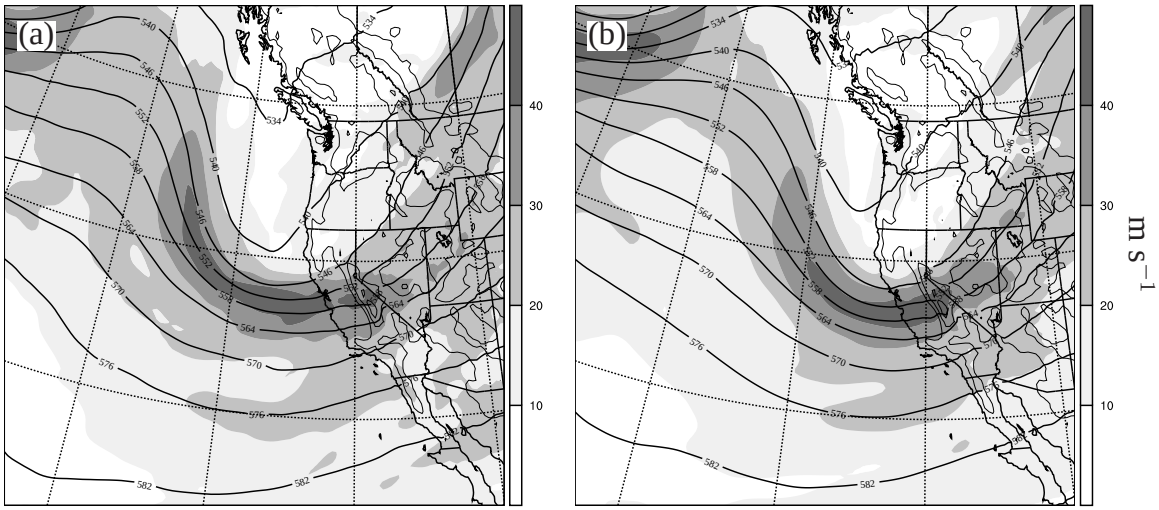

Figure 2.12: The (a) 0- and (b) 6-hr ensemble mean forecast of 500 hPa geopotential height and wind speed for the 00 UTC 17 April, 2006 initialized forecast.

side of the orography. In contrast to the second-order solution, the mountain-wave solution computed with the fourth-order-advection scheme (Fig. 2.13b) is substantially weaker. The maximum vertical velocities in the ensemble mean do not exceed 8 m s^{-1}. Additionally, the ensemble variability of vertical velocity is also considerably reduced. The maximum vertical velocity ranges between 4 m s^{-1} in the weakest member to 16 m s^{-1} in the strongest. In this simulation the 320 K isentrope is only displaced downward about 1 km indicating a much weaker wave. While non-linear effects are clearly present in this mountain-wave simulation, the linear analysis presented in the previous section provides guidance for the sources of the errors in the second-order scheme. The wave energy in the poorly resolved non-hydrostatic modes present in the simulations propagates vertically in the second-order solution leading to a significant over-amplification of the vertically propagating modes.

Associated with the large-amplitude wave in the second-order solution is a severe downslope wind storm penetrating into the Owens Valley. Figure 2.14

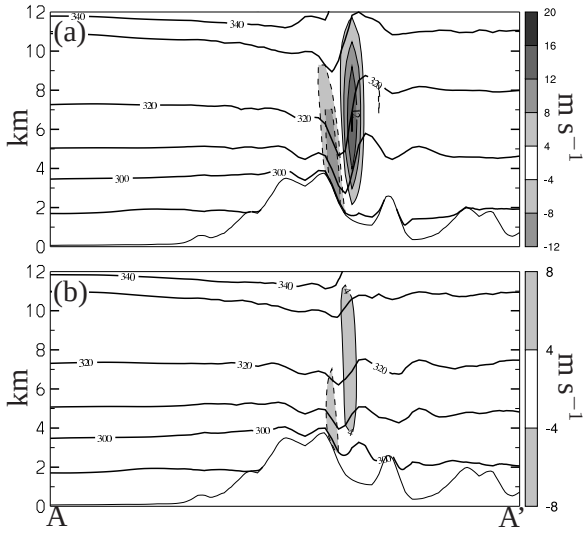

Figure 2.13: The 6-hr ensemble mean forecast of vertical velocity and potential temperature using (a) second- and (b) fourth-order horizontal advection. The location of the cross-section is shown in Fig. 2.11b.

shows the simulated and observed downslope wind speeds 10 m AGL at the point labeled 'Trailhead' in Fig. 2.11b. The observational data has been filtered with a low-pass filter to remove high-frequency oscillations. At the peak intensity of the second-order solution, the simulated winds are more than 30 m s^{-1} stronger than observations. In contrast, the relatively weak mountain-wave in the fourth-order solution leads to much better agreement between the simulated and observed winds. This is especially true for the second-half of the 12 hour forecast where the errors in the model simulation are generally less than 5 m s^{-1}. The larger errors during the first half of the forecast could be associated with adjustments to the mountain-wave structure associated with the switch from the second to fourth-order schemes.

Probability densities of the simulated downslope wind speed at the 'Trailhead' station at 06 UTC are shown in Fig. 2.15. The probability densities have been computed by binning each of the 70 ensemble members into 5 m s^{-1} bins

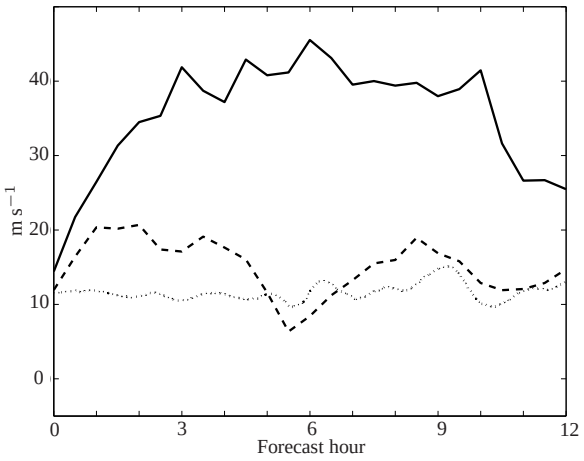

Figure 2.14: The observed (dotted) 10-m downslope wind speed at the University of Leeds Trailhead mesonet station (see Fig 2.11b). Also plotted is the forecasted ensemble mean 10 m wind speed for the second-order (solid) and fourth-order (dashed) horizontal advection schemes.

and normalizing the resulting distribution so that the area under the curve is equal to 1. Switching from the second-order scheme to the fourth-order scheme results in a significant decrease of downslope wind intensity for most ensemble members, as well as a decrease in the ensemble spread.

The weaker downslope winds present in the fourth-order solution can be understood as a response to reduced mid-tropospheric wave breaking. Figure 2.16 shows a scatter plot of the downslope winds in the Owens Valley as a function of the cross-barrier flow aloft at 06 UTC. The downslope winds are computed for each ensemble member by averaging the zonal wind speed over a 250 m deep box whose perimeter is depicted by the solid white line in Fig. 2.11b. The cross-barrier flow is computed as the minimum wind speed perpendicular to the Sierra-Crest between 5 km and 9 km over the region defined by the dashed box in Fig. 2.11b. In the second-order solution (Fig. 2.13a), a large number of ensemble members have reversed flow above the lee-slope, indicating that the mountain waves are breaking. Strong downslope winds in the Owens Val-

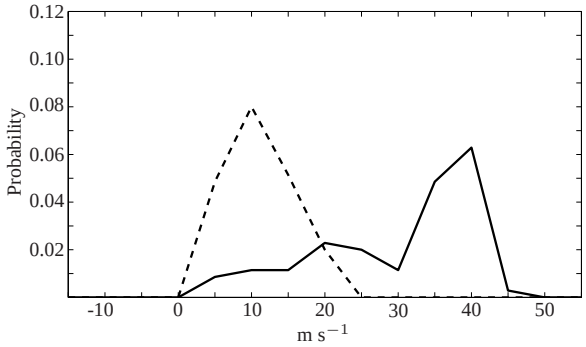

Figure 2.15: The ensemble derived probability density function for the 6 hr forecast of 10 m downslope wind speeds at the Trailhead station. Both the the second- (solid) and fourth-order (dashed) solutions are plotted.

ley are associated with such breaking (Peltier and Clark, 1979). In contrast, the upper-level flow for most of the ensemble members is not reversed in the fourth-order solution, indicating that the mountain wave is not breaking, and as a consequence the downslope winds are much weaker.

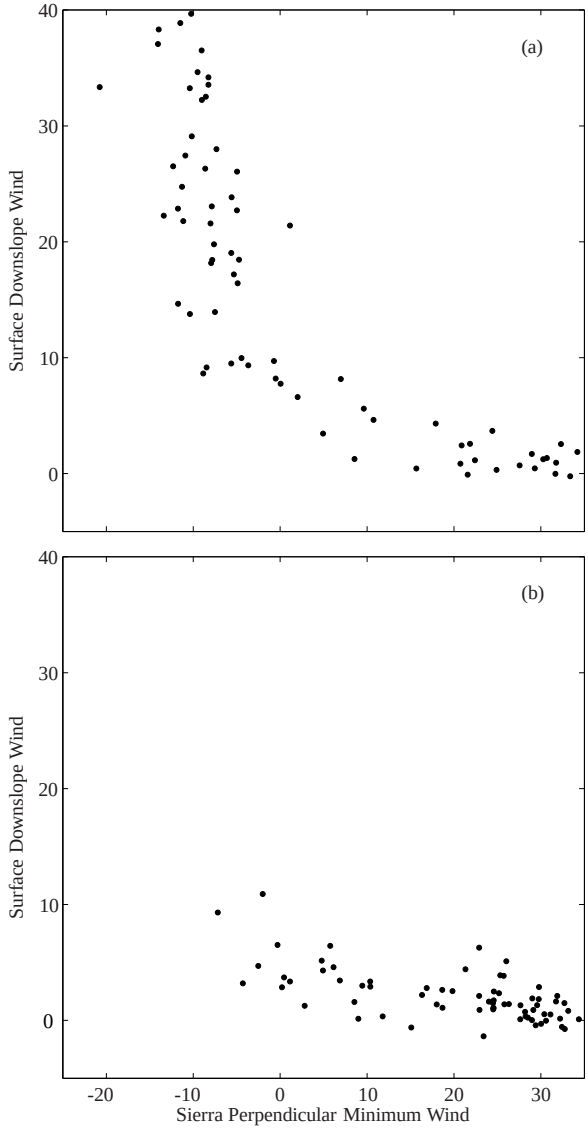

Figure 2.16: The ensemble scatter for the (a) second- and (b) fourth-order horizontal advection schemes between the simulated 6-hr downslope winds in the Owens valley and the minimum Sierra perpendicular wind speed in a region over the Sierra Crest and Owens Valley.

Chapter 3

PREDICTABILITY AND ENSEMBLE VARIABILITY OF DOWNSLOPE WINDS AND MOUNTAIN-WAVES

In this chapter the predictability of two prototypical types of downslope winds will be explored with a fully non-linear, non-hydrostatic NWP model. The first type forms when a large amplitude mountain wave breaks down and strong downslope winds form beneath the breaking region (Clark and Peltier, 1977; Peltier and Clark, 1979). The second type occurs when a layer of strong static stability is located underneath weak upper-tropospheric stability (Durran, 1986a). For this second class of windstorms, wave breaking is not a dominant mechanism. The predictability of mountain-wave breaking and clear-air turbulence will also be discussed.

3.1 Experimental setup

As mentioned previously, the TREX special observing period (SOP; Grubišić et al., 2008) was a two-month long field campaign centered over the Sierra-Nevada mountains and Owens Valley in California (Fig. 3.1). The SOP extended from 1 March - 30 April, 2006 and provided several opportunities to study the predictability of mountain-wave breaking and associated downslope winds as well as the layered-type downslope wind storm.

The COAMPS model (Hodur, 1997, appendix A) is used to perform numerical simulations with a 70-member ensemble of two strong downslope wind events during TREX. The first windstorm, intensive observation period (IOP) 6 (25-26 March, 2006) generated large-amplitude mountain waves which, as

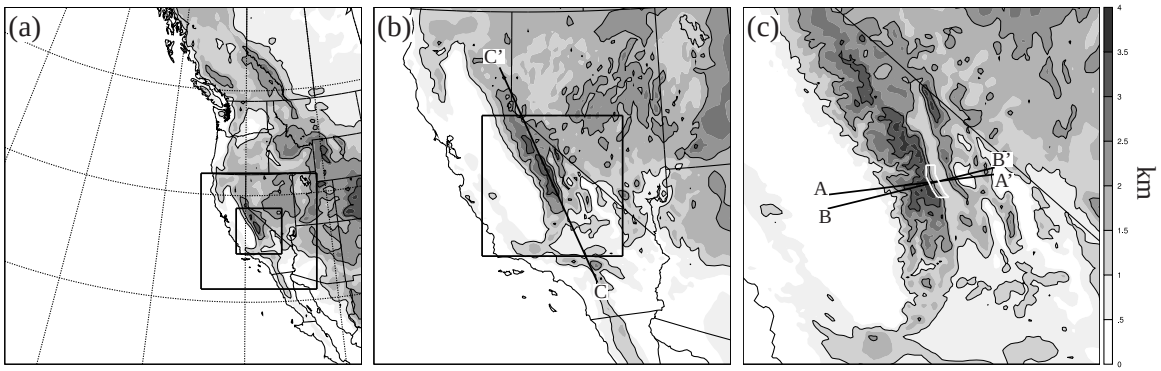

Figure 3.1: The topography on the (a) 27, (b) 9, and (c) 3 km domains. The solid black lines in (b) and (c) indicate the locations of the vertical cross sections. The Owens-Valley metric box is depicted by the solid white lines.

will be shown, contained significant wave-breaking, turbulent kinetic energy (TKE), and strong downslope winds in the Owens Valley. The second windstorm, IOP 13 (16-17 April, 2006), was characterized by upstream layering of the static-stability profile. Wave breaking was not apparent in the model simulations for this case, however, strong downslope winds were simulated on the lee-slope of the Sierra-Nevada mountains. The predictability of each windstorm is characterized by examining the sensitivity of the downslope winds to the model initial conditions. This is done examining the growth of ensemble variability for short-term forecasts. If the ensemble variability grows rapidly then the downslope winds are strongly sensitive to the initial conditions and the predictability is low. Additionally, the extent to which downslope-wind forecasts can be based solely on the large-scale synoptic conditions will be addressed by considering the synoptic-scale variability for the range of downslope wind predictions.

3.1.1 Numerical Model

The numerical setup consists of three one-way nests with 27-, 9-, and 3-km horizontal resolution centered over the Sierra-Nevada mountains and Owens Valley (Fig. 3.1). These domains are identical to the domains used in the previous chapter. Each nest is configured with 40 vertical levels, typical of real-time operational NWP models. The time step on the 3-km domain is 3.3 s and increases by a factor of 3 for each larger domain. Unless otherwise noted, the horizontal advective terms are computed with fourth-order finite differences in this chapter .

3.1.2 Data Assimilation

The EnKF is a relatively new tool for performing data assimilation and generating an ensemble of initial conditions for NWP forecasts. The EnKF is an ensemble-based data assimilation system, which under suitable assumptions, optimally combines a background-estimate of the atmospheric state with observations (Hamill, 2006, appendix B). These ensemble members can then be used as initial conditions for ensemble forecasts. After the data assimilation step, the the variability of the initial conditions represents the uncertainty of the observations and background forecasts.

As described in appendix C, the EnKF is cycled on the 27-km domain for the duration of the TREX SOP. However, due to the high computational costs of running the high-resolution ensemble, the 9- and 3-km experiments were limited to several assimilation cycles prior to the IOP-6 and IOP-13 events. To initialize the nested-domain ensemble, each member is interpolated from the coarse parent domain to the higher-resolution child domain. The 9- and 3-km-domain initializations are staggered in time so that the resolved motions on each domain have time to "spin-up." Table 3.1.2 summarizes the initializa-

Table 3.1: The initialization times of the 9- and 3-km ensembles for the IOP-6 and IOP-13 simulations.

Δx	9 km	3 km
IOP-6	06 UTC, 24 March	00 UTC, 25 March
IOP-13	12 UTC, 15 April	06 UTC, 16 April

tion times on the nested domains for the IOP-6 and IOP-13 forecasts. After each nest is initialized, data assimilation is performed independently every six hours with the same set of observations available for the 27-km domain experiment.

3.2 Synoptic-Scale Flow

The synoptic-scale environment for the IOP-6 and IOP-13 events are described in this section. The IOP-6, 500-hPa ensemble mean analysis of the geopotential heights and wind speed is shown in Fig. 3.2. At 18 UTC, 25 March, 2006 (Fig. 3.2a), a relatively sharp negatively tilted trough is situated directly over the Northern-California coastline. Associated with the trough is 45 m s^{-1} jet maximum located directly west of the San Francisco and strong southwesterly flow extends northeastward over the northern portion of the Sierra-Nevada mountains. The ensemble mean analysis at 00 UTC, 26 March 2006 (Fig. 3.2b) shows that the trough has progressed eastward, however, the intensity of the jet maximum has decreased below 45 m s^{-1} as well as decreasing its spatial coverage. The strongest winds are located directly upstream of the Owens Valley and oriented nearly perpendicular to the barrier. As will be shown, the ensemble mean downslope-wind response is very strong at this time.

The synoptic-scale evolution for IOP-13 case is shown in Fig. 3.3. At 00 UTC, 17 April, 2006 (Fig. 3.3a) a broad, positively titled, trough is situated nearly

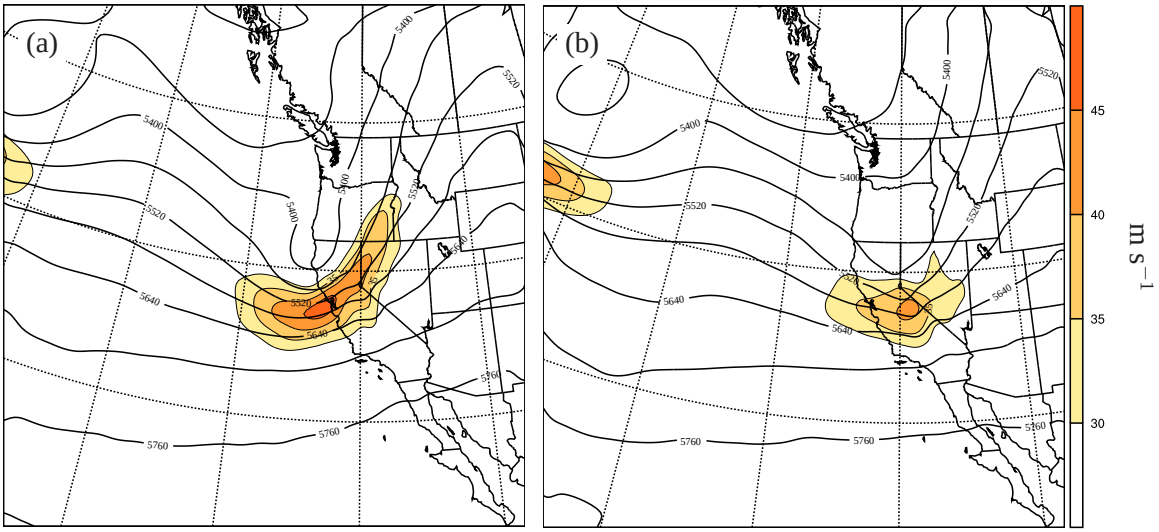

Figure 3.2: The EnKF mean analysis of the 500 hPa geopotential heights and wind speed on the 27-km domain for IOP-6 at (a) 18 UTC, 25 March and (b) 00 UTC, 26 March.

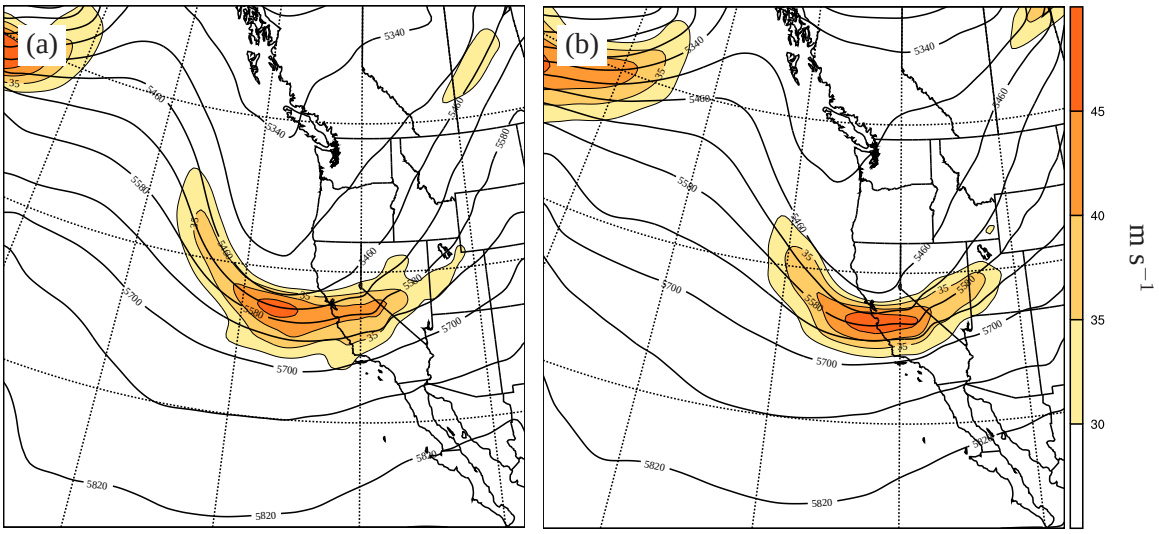

Figure 3.3: The EnKF mean analysis of the 500 hPa geopotential heights and wind speeds on the 27-km domain for IOP-13 at (a) 00 UTC, 17 April and (b) 06 UTC, 17 April.

400-km west of San Francisco. A region of strong westerly flow extends from the base of the trough, eastward across the central and southern Sierra-Nevada mountains. For this case, the wind speeds in the jet max exceed 45 m s^{-1}. Compared to the IOP-6 case, the horizontal scale of the trough is considerably broader and the strong winds extend across a larger area. Six-hours later, at 06 UTC, 17 April, 2006 (Fig. 3.3b) the ensemble mean analysis indicates that the trough has progressed eastward and is located directly upstream of the Sierra-Nevada mountains, over the Central Valley. Additionally, the 500-hPa-jet intensity has increased with a broad region of wind exceeding 45 m s^{-1}. The flow at this time is generally perpendicular to the Sierra-Nevada crest, which is favorable for downslope winds and mountain waves. As will be shown below, distinct layers are evident in the static-stability profile upstream of the Sierra-Nevada with strong static stability in the lower troposphere and weaker static stability aloft. This layering leads to a significantly different downslope-wind response as well as different predictability characteristics compared to the IOP-6 case.

3.3 Downslope Wind Variability

In this section the downslope-wind predictability associated with the wave-breaking response (IOP 6) and the layered response (IOP 13) is explored by considering the ensemble variability of the mountain waves and downslope winds forced by the Sierra-Nevada. For the IOP-6 case, the predictability of forecasts valid at 00 UTC, 26 March are considered. For the IOP-13 event we consider the predictability of forecasts which are valid at 06 UTC, 17 April. To quantify the downslope-wind intensity, an average zonal wind is computed on the 3-km domain within the white box depicted in Fig. 3.1c. In order to capture the low-level westerly momentum associated with the downslope winds, the metric box extends from ground level to 350-m AGL. This metric is referred to

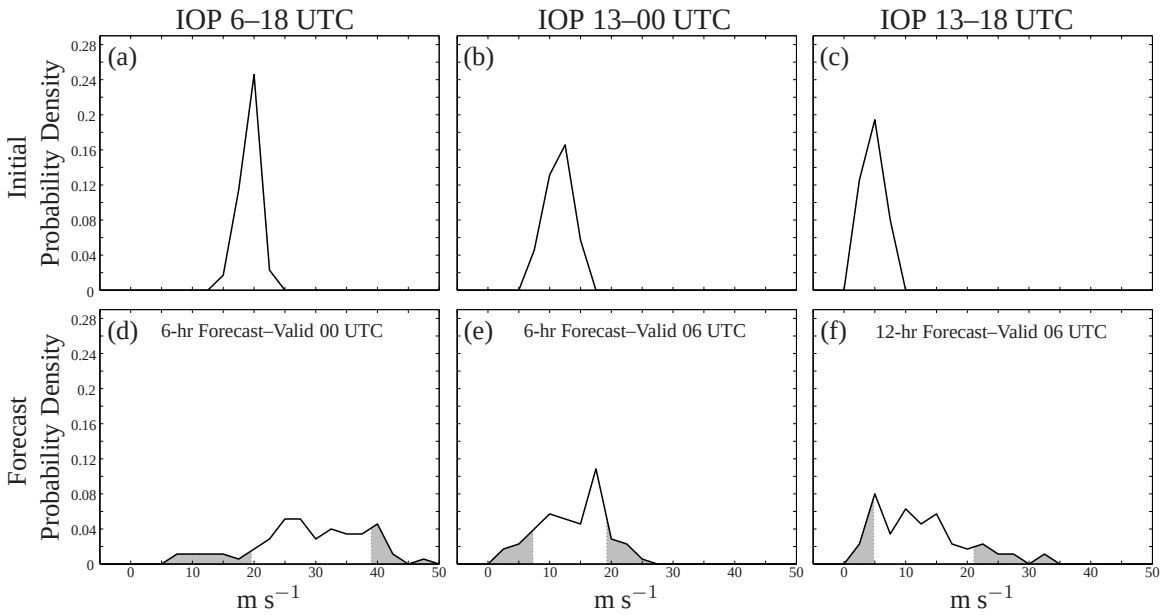

Figure 3.4: The ensemble distributions of the Owens-Valley metric for the (a) IOP-6, 18 UTC, 25 March analysis, (b) IOP-13 00 UTC, 17 April analysis, and (c) IOP-13, 18 UTC, 16 April analysis. Also plotted are the distributions for the (d) 6-hr, IOP-6, 18 UTC forecast, (e) 6-hr, IOP-13, 00 UTC forecast, and (f) 12-hr, IOP-13 18 UTC forecast. The shading shows the fraction of the distribution represented by the strongest- and weakest-10 ensemble members.

as the "Owens-Valley metric" and is used to characterize the downslope wind response throughout this chapter.

3.3.1 Ensemble Distributions

To begin evaluating the predictability characteristics of the two windstorm forecasts, ensemble-derived distributions of the Owens-Valley metric are presented. Figures 3.4a and b show the ensemble distributions of the Owens-Valley metric for the respective IOP-6, 18 UTC, 26 March analysis and IOP-13, 00 UTC, 17 April analysis. The distributions are computed by binning the Owens-Valley metric from each ensemble member into 2.5 m s^{-1}-wide bins and normalizing so that the area under the curve is unity. Equivalently, these can

be thought of as ensemble-derived probability density functions (PDFs). These distributions represent the range of potential downslope wind forecasts given an expected level of uncertainty in the observations and model background.

As a consequence of the EnKF data assimilation, where observations systematically reduce the ensemble variance, the variability of the Owens-Valley metric at the initial time is relatively small. For the 18 UTC, IOP-6 analysis (Fig. 3.4a) the majority of the ensemble members are between 15 and 22.5 m s^{-1} with a definitive peak of the distribution in the 20 m s^{-1} bin. In contrast, the 00 UTC, IOP-13 analysis (Fig. 3.4b) is broader and weaker. The wind speeds at the initial time range between 5 and 17.5 m s^{-1} with a maximum in the 12.5 m s^{-1} bin. The analysis distributions for both the 18 UTC, IOP-6 case and the 00 UTC, IOP-13 case are relatively normally distributed, consistent with the EnKF assumptions (appendix B).

Looking now at the forecast distributions, the PDF of the Owens-Valley metric of the 06-hr, IOP-6 forecast (valid 00 UTC, 26 March) is shown in Fig. 3.4d. The forecast is characterized by large uncertainty growth over the short, 6-hr simulation with a broad region of relatively uniform probabilities between 22.5 and 42.5 m s^{-1}. Assuming that the observed response is sampled from the same distribution as the ensemble, there is approximately a 15% chance that the forecasted winds will verify within any 5 m s^{-1} wide band over this range. In addition, a long tail extends towards weaker winds, suggesting a relatively high chance for false-positive forecasts. On the strong side, there is a sharp cut-off of the distribution for wind speeds greater than 42.5 m s^{-1}, however, one very strong ensemble member is predicting downslope winds close to 50 m s^{-1}. As will be shown below, the synoptic-scale conditions associated with the strong and weak tails of the distribution are similar. This implies that the error growth is localized to the domain of interest.

The distribution for the 6-hr, IOP-13 forecast (valid 06 UTC, 17 April) is

shown in Fig. 3.4e. While the distribution extends from nearly calm flow to downslope winds exceeding 25 m s^{-1}, there is a distinct peak centered at 17.5 m s^{-1} bin. The probabilities within this bin are nearly twice as large as the probabilities associated with the surrounding bins suggesting that more confidence can be placed in the 6-hr forecast of the IOP-13 downslope-wind event than in the 6-hr forecast of the IOP-6 event.

The relatively narrow probability distribution for IOP-13 6-hr forecast suggests that it may be worthwhile to examine a 12-hr forecast for the same event. The distributions for 18 UTC, 16 April analysis and 12-hr forecast valid at 06 UTC, 17 April are shown in Figs. 3.4c and f. Larger uncertainty is associated with the 12-hr, IOP-13 forecast compared to the 6-hr forecast valid at the same time. As with the other two simulations, the analysis is characterized by a relatively narrow distribution associated with the data assimilation procedure; the wind speeds fall between 0 an 10 m s^{-1} (Fig. 3.4c). However, over the course of the 12-hr forecast, the downslope wind speeds increase substantially in a number of the ensemble members. Considerable uncertainty is associated with the 12-hr downslope-wind forecast (Fig. 3.4f). A relatively large section of the PDF uniformly distributed with approximately a 20% chance that the actual wind speeds will fall within any 5 m s^{-1} band between 2.5 and 17.5 m s^{-1}. In contrast to the 6-hr forecast, a relatively long tail extends towards the stronger downslope wind state.

In order to evaluate short-term forecasts with relatively similar ensemble spreads we only consider the 12-hr, IOP-13 forecast initialized at 18 UTC, 16 April. Unless otherwise noted, the simulation initialized at 18 UTC, 25 March will be referred to as the IOP-6 forecast and the simulation initialized 18 UTC, 16 April, 2006 will be referred to as the IOP-13 forecast.

3.3.2 Strongest and Weakest Members

The predictability of the two events can be further examined by considering the range over which the forecasted downslope winds vary within the ensemble. To this end, the members are ranked according to the forecast intensity of the Owens-Valley metric, and the 10 strongest and 10 weakest ensemble members are grouped into two subsets. The shaded regions of the ensemble forecast distributions (Figs. 3.4d-f) shows the fraction of the PDF containing the strongest- and weakest-10 members. While these subsets are located on the tails of the distributions, they represent almost 30% of the total probability.

Averages over the subsets are computed to give representative strong and weak responses which characterize the maximum possible difference of the downslope-wind forecast given expected levels of initial-condition uncertainty. The averages can also be thought of as composites of the strong and weak response. Compositing the response in this way makes for a simple comparison between the strong and weak response on both the mesoscale and the synoptic-scale. Furthermore, using 10 ensemble members to compute the composites ensures that any large differences are not a consequence of unrepresentative outlying members.

For the IOP-6 simulation, the members are ranked from the 6-hr forecast valid 00 UTC, 26 March. As will be shown below, the variation between the strong and weak subset is large at this time and represents the maximum variability over the 12-hr simulation. In contrast, for the IOP-13 forecast the growth rate of the initial uncertainty is slower. We therefore consider differences between strong and weak subsets ranked from the 12-hr forecast initialized 18 UTC, 16 April and valid 06 UTC, 17 April. It will be demonstrated that the ensemble variability for the 6-hr IOP-13 forecast initialized 00 UTC, April and valid 06 UTC, 17 April is considerably smaller than the 12-hr forecast valid

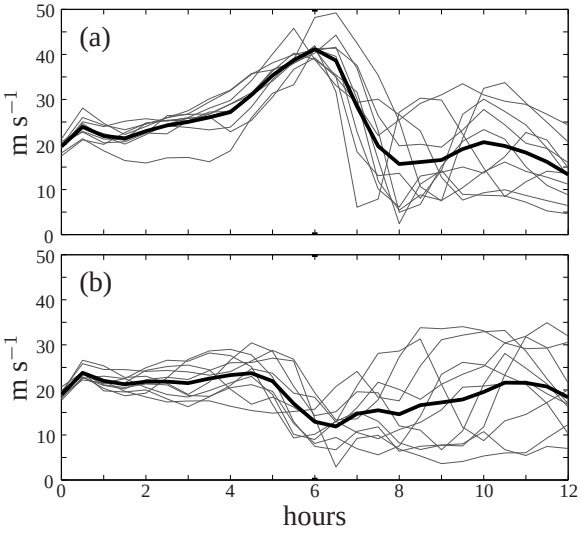

Figure 3.5: The zonal wind averaged over the Owens-Valley metric box during the IOP-6 simulation for the (a) 10-strongest and (b) 10-weakest ensemble members at $t = 6$ hrs. The black line shows the mean of the 10-members subsets.

at the same time.

The time dependence of the downslope winds of the strongest- and weakest-10 members of the 12-hr IOP-6 forecast is shown in Fig. 3.5. The mean evolution of each subset is also plotted. A mean difference of nearly 29 m s^{-1} between the strong and weak members is readily apparent at hour 6. The downslope flow exceeds 35 m s^{-1} for all of the strong members and is generally less than 15 m s^{-1} for all of the weak members. Following the strong-member wind-storm peak, the intensity rapidly decreases. For both the strong and weak subsets the 6–12 hr forecast is characterized by large variability of the Owens-Valley metric with the wind speeds ranging from less than 5 m s^{-1} to stronger than 30 m s^{-1}. As will be shown below, the large variability is associated with mountain-wave breaking in the ensemble solutions.

For the IOP-13 simulations, the evolution of the downslope winds are considerably different. Figure 3.6 shows the individual ensemble members as well

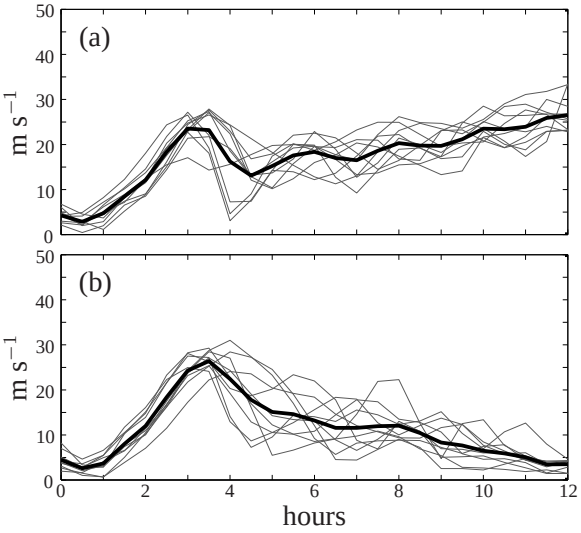

Figure 3.6: The zonal wind averaged over the Owens-Valley metric box during the IOP-13 simulation for the (a) 10-strongest and (b) 10-weakest ensemble members at $t = 12$ hrs. The black line shows the mean of the 10-members subsets.

as the ensemble mean from the strong and weak subsets. The ensemble members are ranked according to the strength of the Owens-Valley-metric at hour 12, corresponding to 06 UTC, 17 April. While the intensity of both the strong and weak subsets is lower compared to the IOP-6 simulation, the difference between the subset means for the 12-hr forecast again exceeds 20 m s^{-1}. Early in the forecast, around hr 3.5, both the strong and weak subsets predict relatively strong downslope winds; however, the differences between the two subsets grows steadily between hours 5 and 12. It should be noted the the difference between the strong- and weak-member mean for the 6-hr IOP-13 forecast initialized at 00 UTC, 17 April and valid 06 UTC, 17 April is approximately 15 m s^{-1} which is consistent with the narrower forecast distribution (Fig. 3.4e).

3.3.3 Downslope-Wind and Mountain-Wave Response

Associated with the strong downslope-wind response in the Owens Valley, is a large amplitude mountain wave forced as the stably-stratified, synoptic-scale flow interacts with the Sierra-Nevada mountains. Here, the difference in the mountain-wave structure associated with the strong and weak downslope-wind response is compared along vertical cross-sections depicted by the solid black lines in Fig. 3.1c. The orientation of the cross-section is representative of the ensemble-mean mid-tropospheric synoptic-scale flow for the 6-hr, IOP-6 forecast (AA' cross-section) and the 12-hr, IOP-13 forecast (BB' cross-section). Both the AA' and BB' cross-sections pass through the center of the Owens-Valley metric box.

Wave-Breaking Response

Figures 3.7ab shows the zonal-wind component, as well as the turbulent kinetic energy (TKE) for the 6-hr, IOP-6 forecast along the AA' vertical cross-section. The panels labeled "weak members" and "strong members" are obtained by averaging the fields over the weak and strong ensemble subsets. Consistent with the evolution of the Owens-Valley metric (Fig. 3.5), the differences between the strong and weak members have grown very large over the short 6-hr forecast. For the strong members (Fig. 3.7b), a tongue of high wind extends from the mid-troposphere, down the lee-slope of the Sierra-Nevada, and into the Owens Valley. An extensive region of wave breaking is indicated by the strongly decelerated flow and large area of turbulent mixing between 8–12 km. The wave breaking is associated with the generation of the strong downslope flow on the lee-slope (Clark and Peltier, 1977; Peltier and Clark, 1979). In contrast, the weak members (Fig. 3.7a) are characterized by high zonal-momentum air that does not extend below crest level. For this solution set, the upper-level wave

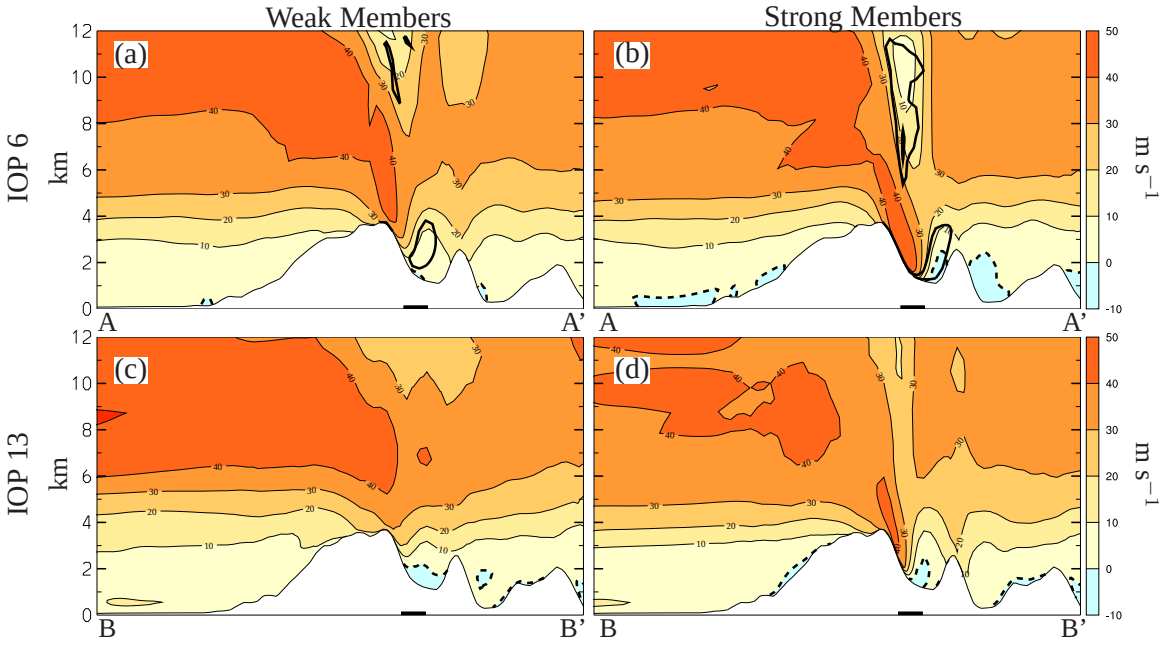

Figure 3.7: The zonal wind u (shaded) and TKE (heavy contours) along a vertical cross-section across the Sierra-Nevada mountains for the (a) weakest- and (b) strongest-10 ensemble members for the IOP-6 6-hr forecast as well as the (c) weakest- and (d) strongest-10 ensemble members for the IOP-13 12-hr forecast. The contour interval is 10 K for u and 10 m^2 s^{-2} for TKE. The zero u contour is depicted by the dashed line.

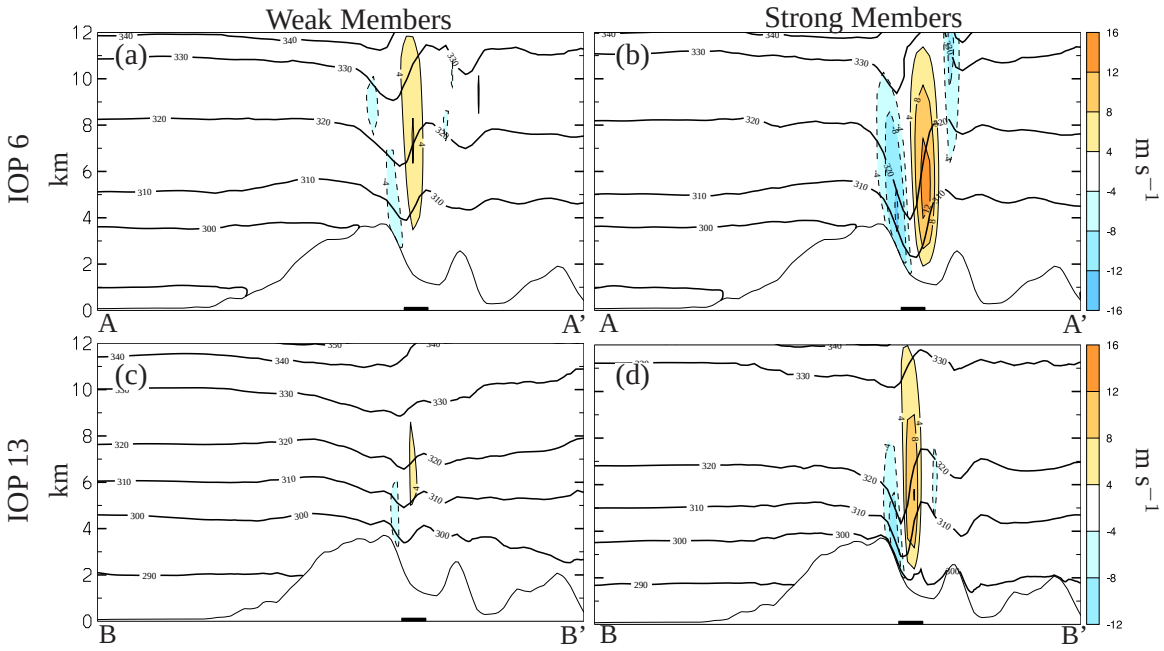

Figure 3.8: Same as Fig. 3.7 except for the vertical velocity w and potential temperature θ. The zero contour of vertical velocity is omitted and the negative contours are dashed.

breaking is less extensive, weaker, and displaced vertically. A small region of decelerated flow, with zonal winds less than 10 m s^{-1} is apparent near 12-km ASL. Furthermore, the spatial extent of the turbulent mixing region is much smaller with the TKE barely exceeding 10 m^2 s^{-2}.

The vertical velocity w and potential temperature θ for the IOP-6, 6-hr forecast are plotted along the same vertical cross-section in Fig. 3.8ab. The strong downslope-wind solution (Fig. 3.8b) contains a high-amplitude mountain wave, as indicated by the large perturbations of θ and couplet of intense vertical velocity on the lee-side of the Sierra-Nevada. For example, the 320-K isentrope is displaced downward nearly 4 km from its nominal upstream height of 8 km. Furthermore, the maximum vertical velocity is nearly 14 m s^{-1} in the core of the updraft. Several of the individual ensemble members have a considerably

stronger mountain wave with vertical velocity magnitudes greater than 26 m s^{-1}. Additionally, overturning is more evident for the individual members, however, the subset average smooths this response. In contrast, the weak solution (Fig. 3.8a) is characterized by a mountain wave with considerably lower amplitude. For these members the maximum vertical velocity is only 8 m s^{-1}, over 40% less than the strong solution. Furthermore, the downward displacement of the 320 K isentrope is close to 50% less than the strong solution.

It is important to note that the difference between the strong and weak downslope wind response is due to major structural differences in the mountain wave as opposed to small contrasts of the downslope extent of the high-momentum air. These large differences occur even though the upstream conditions are very similar. For example, the zonal momentum upstream of the Sierra-Nevada crest is nearly indistinguishable between the strong and weak members (compare the left sides of Figs. 3.7ab). Forward shear is apparent in both examples with the zonal-wind increasing from 10 m s^{-1} near crest level to 40 m s^{-1} near the tropopause. The stability of the upstream profiles is also very similar between strong and weak members (Figs. 3.8ab). A layer of strong crest-level stability is apparent for both solutions and the undisturbed tropopause height is nearly identical for the two solutions. Despite these similarities, the mountain-wave and downslope-wind forecast between the two subsets is considerably different suggesting very strong sensitivity to the model initial conditions and a short predictive time scale.

Clear-air turbulence (CAT) commonly affects aircraft over regions of complex terrain (Nastrom and Fritts, 1992). With fine-scale numerical models it is possible to simulate CAT (Clark et al., 2000), however, the predictability of these events is not known. The large region of turbulent mixing and strong vertical velocities associated with the strong subset, suggest that significant clear-air turbulence is forecast through a deep layer over the Owens Valley. In

contrast, the weak vertical velocities and absence of TKE indicate that significant CAT is not forecasted for the weak members. In this event, the uncertainty associated with CAT forecasts would make accurate predictions difficult.

Layered Response

Consider now the strong and weak IOP-13 downslope-wind predictions. Figures 3.7cd shows the zonal wind, as well as the TKE for the 12-hr IOP-13 forecast along the BB' vertical cross-section. Evident in the strong solution (Fig. 3.7d) is a region of high westerly-momentum air extending down the lee-slope of the Sierra-Nevada mountains and into the Owens Valley. The strength of the downslope flow exceeds 40 m s^{-1} high on the lee-slope but decreases sharply towards the base of the Owens Valley. In contrast to the IOP-6 strong subset, mountain-wave breaking is not present in the upper troposphere along the BB' cross-section. The upper-level winds above the Owens Valley are generally greater than 20 m s^{-1} and turbulent mixing, as indicated by TKE, is completely absent. Despite the lack of wave breaking, the difference between the strong and weak forecast is large. The weak ensemble members (Fig. 3.7c) show that the strong zonal flow is limited to regions above crest-level. Additionally, the weak members exhibit easterly flow within the Owens Valley which extends nearly half-way up the lee-slope of the Sierra-Nevada.

The structure of the mountain-wave for the 12-hr IOP-13 forecast, as revealed by θ and w, are plotted along the BB' vertical cross-section in Figs. 3.8cd. In the strong cases (Fig. 3.8d), the mountain wave is characterized by large θ perturbations and a vertical-velocity maximum greater than 12 m s^{-1}. Upstream of the Sierra-Nevada, the static-stability profile is composed of two distinct layers within the troposphere: a layer of strong static-stability below 6-km ASL and layer of weak static-stability between 6- and 11-km ASL. The layered structure leads to an amplification of the shorter wavelengths through non-

linear processes (Durran, 1986a, 1992) and a short wavelength hydraulic-jump like response on the lee-slope. In fact, the horizontal wavelength is nearly half that of the strong IOP-6 solution (Fig. 3.8b) suggesting that the shorter wavelengths are being amplified.

In contrast, the weak solution contains a mountain wave with considerably lower amplitude (Fig. 3.8c). The vertical-velocity maximum is roughly 66% less than the strong solution and the vertical displacement of the isentropes is generally less than 0.5 km. Upstream of the Sierra-Nevada, the static-stability profile is considerably different. While a layered structure is still evident, the vertical distribution of the Brunt-Väisälä frequency and wind speed varies. Relative to the strong case, the stability is weaker near crest level and stronger in the middle to upper troposphere and the wind speeds are stronger in the upper troposphere. The differences of the static-stability and wind speed between Figs. 3.8c and d are presumably responsible for the differences in the mountain-wave and downslope-wind amplitude, however, the fact that such a large difference between the subsets develops over the 12-hr forecast suggests that this layered-type wind storm experiences a strong dependence on the model initial conditions.

3.4 Synoptic-Scale Variability

In this section, the synoptic-scale variability associated with the wide range of downslope-wind predictions will be considered. Emphasis will be placed on the synoptic-scale structure of the ensemble members with the strongest and weakest wind storms both at the time of the simulated storm as well as the upstream conditions several hours prior to the storm.

3.4.1 Strong and Weak Synoptic-Scale members

Mean synoptic-scale flow structures for the strong and weak downslope-wind response are obtained by averaging the ensemble members on the 9-km domain over the strong and weak subsets. Figure 3.9ab shows the mean 500 hPa wind speed and geopotential heights for the strong and weak IOP-6, 6-hr forecasts (the same time that the ensemble members are ranked). Visual inspection reveals that the location of the 500 hPa trough and jet is very similar between the two subsets. The trough axis for both solutions is located directly over the crest and the wind-speed magnitude upstream of the crest is between 35-40 m s^{-1} with wind speeds slightly larger for the strong subset.

Further evidence of the similarity between the strong and weak IOP-6 solution is revealed by considering the forecast along the CC' vertical cross-section, which as indicated in Fig. 3.1b, is located along the Sierra-Nevada crest. Figures 3.10ab show the 6-hr, IOP-6 forecast of the wind speed U and the potential temperature θ along the cross section for the strong and weak members. Given the large differences between the downslope winds predicted to occur at this time in the strong and weak subsets, the similarities in the flow above the crest are remarkable. Both show a stable layer extending from crest-level to approximately 5-km ASL and both contain a strong jet between 6 and 10 km. Additionally, the tropopause is located at approximately 10 km ASL for both subsets. While the intensity of the cross-barrier flow is slightly larger for the strong members north of the Owens-Valley metric box (indicated by the heavy line at the bottom of the panels), directly upstream of the metric box the velocities are very similar. The similarities can be quantified by considering the RMS differences in the plane of the cross-section between the two subsets. For the wind speed the RMS difference is 2.1 m s^{-1} and for θ it is 0.8 K. These differences are generally within the error bounds typically associated

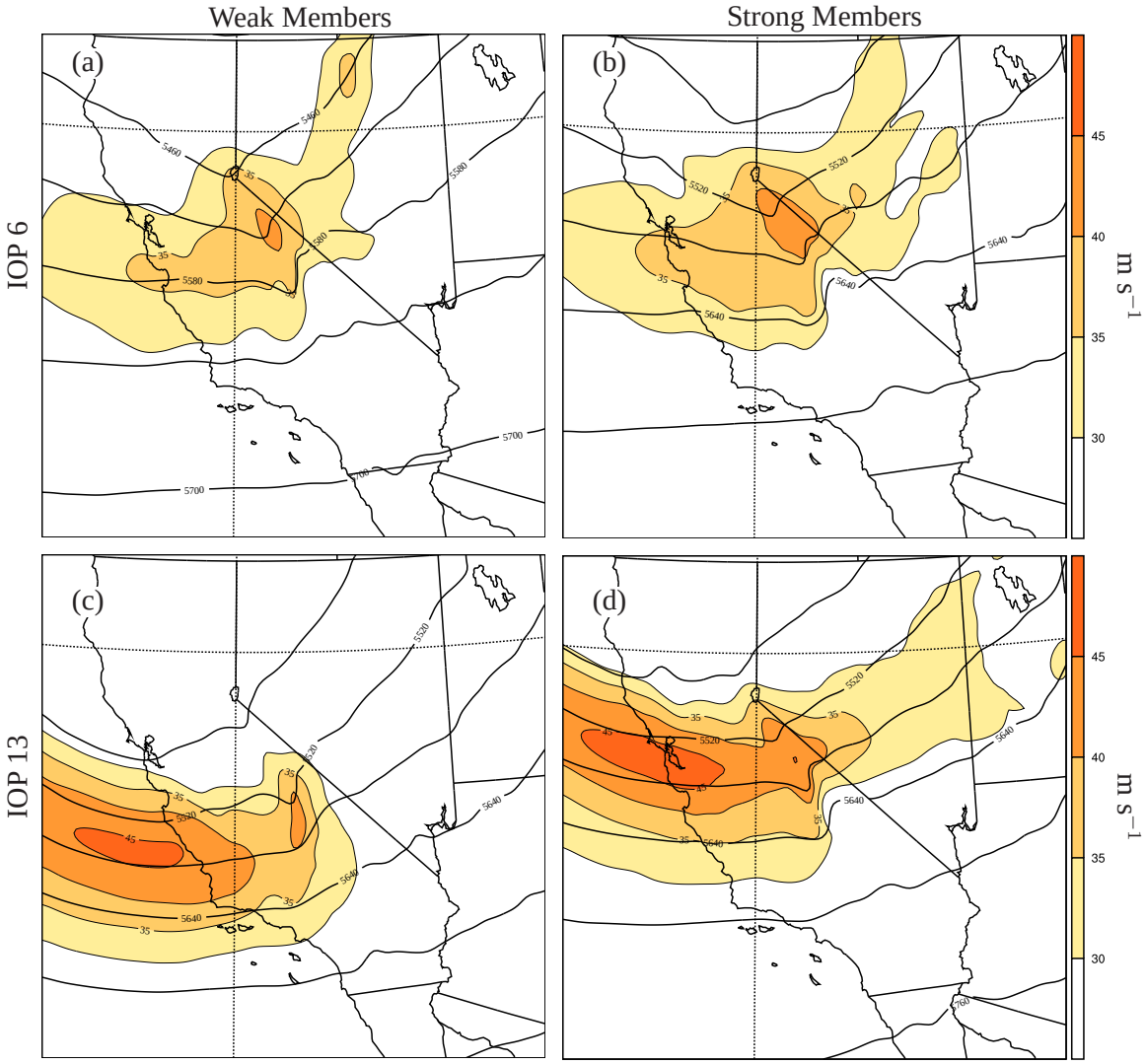

Figure 3.9: The 500 hPa wind speed and geopotential heights for the (a) weak and (b) strong members of the IOP-6 6-hr forecast as well as the (c) weak and (d) strong members for the IOP-13 12-hr forecast.

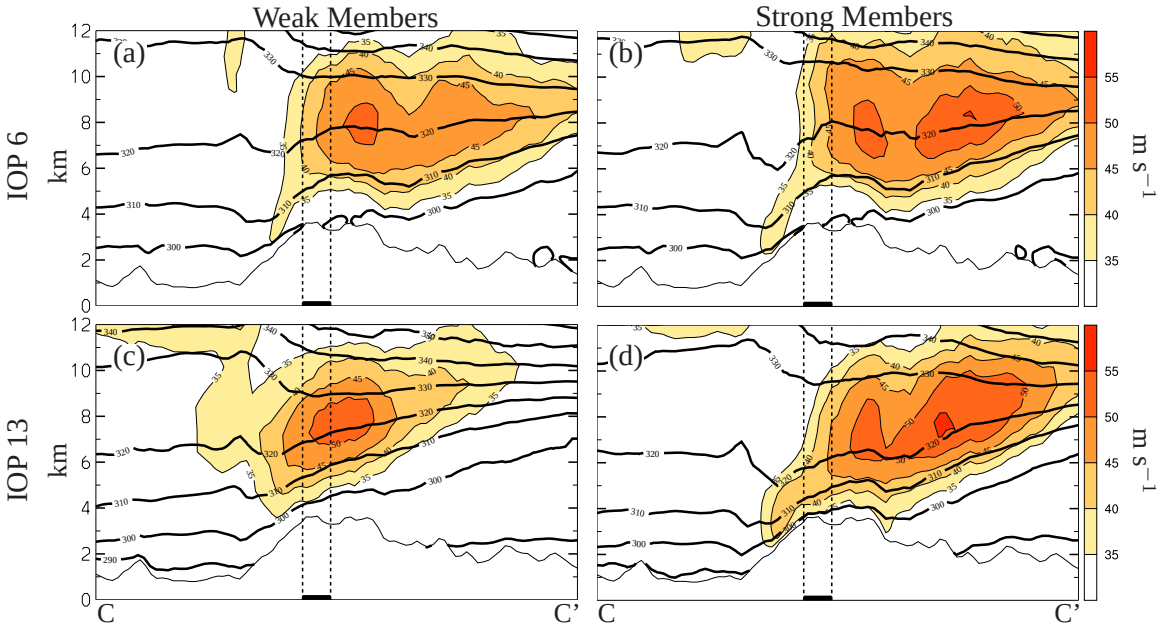

Figure 3.10: The composite total wind speed and potential temperature along a vertical cross-section for the 10 weakest and strongest ensemble members from the (a,b) IOP-6 6-hr forecast and (c,d) IOP-13 12-hr forecast. The cross-section is located on the 9-km domain and extends along the length of the Sierra-crest shown in Fig. 3.1b. Wind speed is contoured ever 10 m s^{-1} while potential temperature is contoured every 10 K.

with radiosonde observations which suggest that differentiating between the wave-breaking and the non-wave-breaking events would be nearly impossible for either a human forecast or a numerical model.

The mean 500-hPa geopotential height and wind speed for the strong and weak members is plotted Figs. 3.9cd. In contrast to the IOP-6 case, relatively large differences are apparent between the strong and weak subsets. For the strong subset, the jet maximum is located over the San-Francisco Bay, while for the weak subset, the jet maximum is displaced approximately 150 km to the south. Additionally, the intensity of the jet is slightly stronger for the strong subset. It should be noted, however, that the differences between the two subsets is not a consequence of a timing error, since the eastward propagation of the 500-hPa trough is almost identical between the two subsets.

The differences of θ and U along the CC' cross-section at the time a maximum winds are also relatively large between the strong and weak subsets (Fig. 3.10cd). For example, north of the Owens-Valley metric box, the winds are considerably stronger for the strong-member subset. However, directly upstream of the metric box the wind speed is actually stronger for the weak-member subset. The RMS wind-speed differences in the plane of the CC' cross-section is 7.5 m s^{-1} which is considerably larger than radiosonde observational errors.

Relatively large differences are are also apparent between the θ fields where the RMS difference is 4.1 K. In the strong-member subset, a region of high static stability is located just above the mountain crest with weaker stabilities further aloft. In contrast, the region of high static-stability in the weak-member subset is displaced upward into the middle troposphere. This vertical displacement of the strong-static-stability layer is associated with the north-south shift of the jet and the associated upper-level front apparent in Fig. 3.9. For the strong solutions, where the jet-stream is further north, the

sloping surface of the upper-level front intersects the Sierra-Nevada crest directly upstream of the Owens-Valley metric box. On the other hand, for the weak members, the sloping surface of the upper-level front is displaced further southward and is therefore located above the mountain crest upstream of the Owens-Valley metric box.

3.4.2 Upstream Soundings

A single sounding profile upstream of a mountain barrier is sometimes used for downslope-wind prediction (e.g. Klemp and Lilly, 1975; Nance and Coleman, 2000). In this section, upstream profiles corresponding to the strong- and weak-member forecasts will be compared. Upstream profiles of the cross-barrier component of the flow U, the potential temperature θ, and the Brunt-Väisälä frequency N for the IOP-6 and IOP-13 forecasts are considered. The cross-barrier wind U is defined as the component of the flow perpendicular to the Sierra-Nevada crest (25° south of westerly).

Figure 3.11 shows the 5-hr IOP-6 forecasted soundings of U, θ, and N upstream of the Sierra-Nevada range for the strong and weak subsets. The location of the soundings corresponds to the termination point of 1-hr back trajectories launched from the 6-hr forecast at 5-km ASL along the Sierra-Nevada crest directly upstream of the Owens-Valley metric box. In this way the profiles represent the air that will, one hour later, interact with the Sierra-Nevada at the time when the ensemble members exhibit their largest variability. The differences between the U profiles are generally less than 3 m s^{-1} through the depth of the troposphere, while the θ and N profiles are nearly indistinguishable. Both the strong- and weak-member soundings contain a well-defined stable layer near crest-level, weaker static-stability in the upper troposphere, and a tropopause height close to 9.5 km. For the IOP-6 wave breaking case it would be hard to imagine that a forecaster could differentiate between the strong

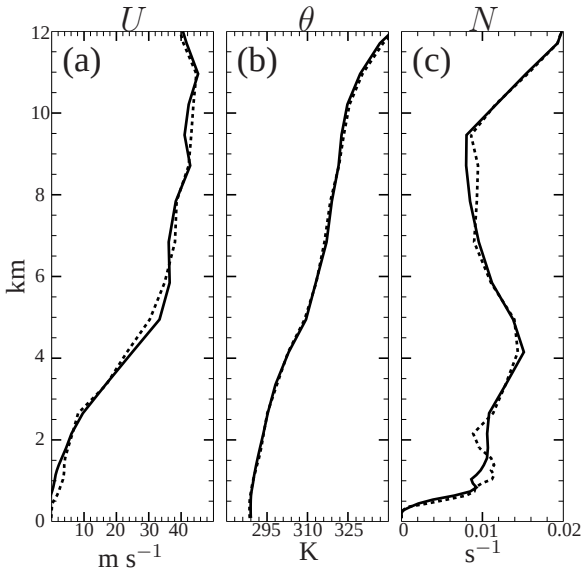

Figure 3.11: Model soundings for the ensemble members with the strongest (solid) and weakest (dashed) weakest downslope-wind responses at $t = 6$ hrs of the IOP-6 simulation. The soundings are valid at $t = 5$-hrs at the upstream edge of the AA' cross-sections depicted in Fig. 3.1c. Plotted is the (a) cross-barrier component of the wind, (b) potential temperature θ, and (c) Brunt-Väisälä frequency N.

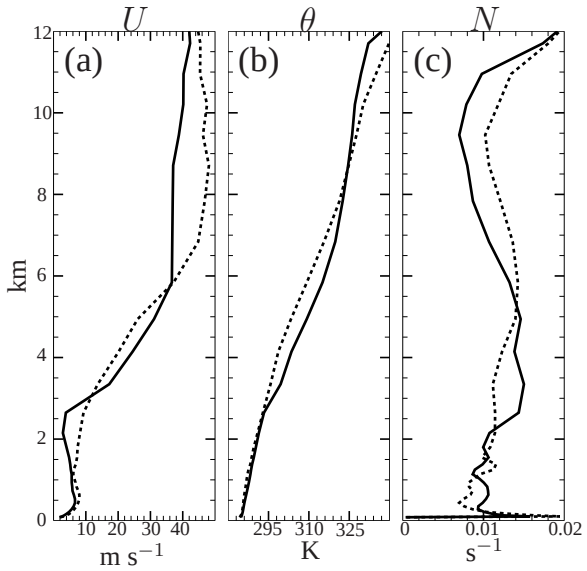

Figure 3.12: Model soundings for the ensemble members with the strongest (solid) and weakest (dashed) weakest downslope-wind responses at $t = 12$ hrs of the IOP-13 simulation. The soundings are valid at $t = 11$-hrs at the upstream edge of the BB' cross-sections depicted in Fig. 3.1c. Plotted is the (a) cross-barrier component of the wind, (b) potential temperature θ, and (c) Brunt-Väisälä frequency N.

response and the weak response based on a single upstream profile. Furthermore, assimilating radiosonde data at this location would do little to improve a NWP downslope wind forecast because the differences between the weak and strong members are within the error bounds associated with radiosonde observations.

The upstream profile of U, θ, and N for the strong- and weak member IOP-13 subset is shown in Fig. 3.12. As with the IOP-6 case, the location of the sounding corresponds to the location of 1-hr back trajectories launched from the 12-hr forecast at the Sierra-Nevada crest 5-km ASL directly upstream of the Owens-Valley metric box. In contrast to the IOP-6 case, however, substantial differences between the strong- and weak-member soundings are apparent in Fig. 3.12. For example, the cross-barrier flow above 6-km is nearly 10

m s^{-1} stronger in the weak members. Additionally, significant differences of the static-stability exist between the strong and weak profiles. For the strong members, a classic layered structure with high static-stability in the lower atmosphere and low static-stability aloft is apparent. This layering is favorable for strong downslope winds on the lee-side of the barrier (Durran, 1986a). In contrast, the weak-member profile has relatively weaker static-stability in the 2.5–4 km layer and a stronger static-stability layer above 5 km. In contrast to the IOP-6 wave-breaking event, signatures potentially capable of distinguishing between the strong and weak subsets are available at short lead times in IOP 13 suggesting a slightly longer predictive time scale for this case.

3.5 Ensemble Sensitivity Analysis

One potential method that could be used to quantify downslope-wind predictability is ensemble sensitivity analysis (ESA). First proposed by Hakim and Torn (2006), ESA computes the sensitivity of a forecast metric with respect to the model initial conditions by utilizing the statistics of the ensemble members and linear regression. If J is defined as a vector, where each element contains an estimate of the forecast metric from each ensemble member, and $\mathbf{X}_i$ contains the ensemble analysis of a given variable (e. g. wind speed, static-stability) at the i^{th} grid point, then the sensitivity of the forecast metric to the analysis variable can be approximated as

$$\frac{\partial \mathbf{J}}{\partial \mathbf{X}_i} \approx \frac{cov(\mathbf{J}, \mathbf{X}_i)}{var(\mathbf{X}_i)}, \tag{3.1}$$

where cov and var are the covariance and variance calculated over the ensemble. In other words, the gradient of the forecast metric with respect to an initial condition is approximated as the linear regression between the ensemble of the forecast metric and the ensemble of the initial variable at each grid point. This sensitivity gradient can then be multiplied by an expected change in $\mathbf{X}_i$

(e. g. the ensemble standard deviation σ) to give an expected change in $\mathbf{J}$.

ESA has been applied in several synoptic-scale situations with general success. Hakim and Torn (2006) used ESA to diagnose relationships between the minimum central pressure of a mid-latitude cyclone and fields such as geopotential height and wind speed. Ancell and Hakim (2007) compared the sensitivity fields derived from the ESA method to adjoint sensitivities. They also derived a linear relation between ensemble sensitivities and adjoint sensitivities. Torn and Hakim (2008a) showed that ESA could be used to determine climatological patterns of initial conditions sensitivity for synoptic-scale forecasts. They demonstrated that forecasts of sea-level pressure and rainfall over Western Washington were sensitive to the upstream mass and temperature variables. While ESA has been successfully applied to synoptic-scale motions, its ability to capture mesoscale sensitivity is unknown and will therefore be tested for downslope winds.

We discuss ESA for the IOP-6 and the IOP-13 simulations. The COAMPS model is initialized with the EnKF analysis at 18 UTC, 25 March for the IOP-6 case and 00 UTC, 17 April for the IOP-13 case. As with the simulations described above, a 27-, 9-, and 3-km configuration is used. The sensitivity of the downslope-wind response on the 3-km domain, as measured by the Owens-Valley metric box, to the wind speed and Brunt-Väisälä frequency analysis on the 27-km domain is presented. Wind speed and static-stability are used because of their theoretical connection to downslope winds. In particular strong crest-level stability and strong cross-barrier flow are commonly associated with strong downslope wind (e.g. Brinkmann, 1974; Bower and Durran, 1986).

The experiments in this section differ from the simulations performed earlier in the chapter in two ways. First, the Owens-Valley metric box has a greater horizontal extent and is defined according to the box in Fig. 2.11b. Second, the horizontal advective terms are computed with second-order finite

differences. While it was shown in chapter 2 that second-order advection can lead to a significant over-amplification of the mountain-wave, it is not unreasonable to test ESA with this advection scheme given that the sensitivities are computed with consistent numerics and dynamics.

Figure 3.13 shows the ensemble sensitivity of the 7-hr, IOP-13 downslope wind forecast on the 3-km domain to the 00 UTC, 17 April EnKF analysis on the 27-km domain. This time is chosen because the downslope wind sensitivities to low-level static stability are maximized. Slightly weaker sensitivities occur at adjacent times. The sensitivity is plotted with respect to the 7-km wind speed and 4-km Brunt-Väisälä frequency. The sensitivities have been multiplied by an ensemble standard deviation in order to give the expected sensitivity response of the downslope winds. The statistical significance of the linear-regression calculation is computed at the 95% level (Wilks, 2006) and regions that do not pass the test are masked. Additionally, regions where the magnitude of the sensitivity response is less than 2 m s^{-1} are masked.

The sensitivity response to the 7-km initial wind-speed field (Fig. 3.13a) is concentrated along a east-west line extending from the Sierra-Nevada mountains, north of the San-Francisco Bay, and westward over the Pacific Ocean. This sensitive region is focused around the zonal jet (contours) and has a maximum directly north of San Francisco. The positive correlations indicate that a stronger mid-tropospheric jet will lead to stronger downslope winds. Quantitatively, the sensitivities predict that a $\pm\sigma$ change of the initial wind speed in this region will result in approximately a ± 7 m s^{-1} change of the 7-hr downslope-wind forecast. Northwest and southeast of the jet are regions of negative sensitivity that predict a $\pm\sigma$ change will result in up to a ∓ 5 m s^{-1} change of the 7-hr downslope-wind forecast.

The downslope-wind sensitivity response to the 4-km Brunt-Väisälä frequency at the analysis time (Fig. 3.13b) is concentrated along a thin band ex-

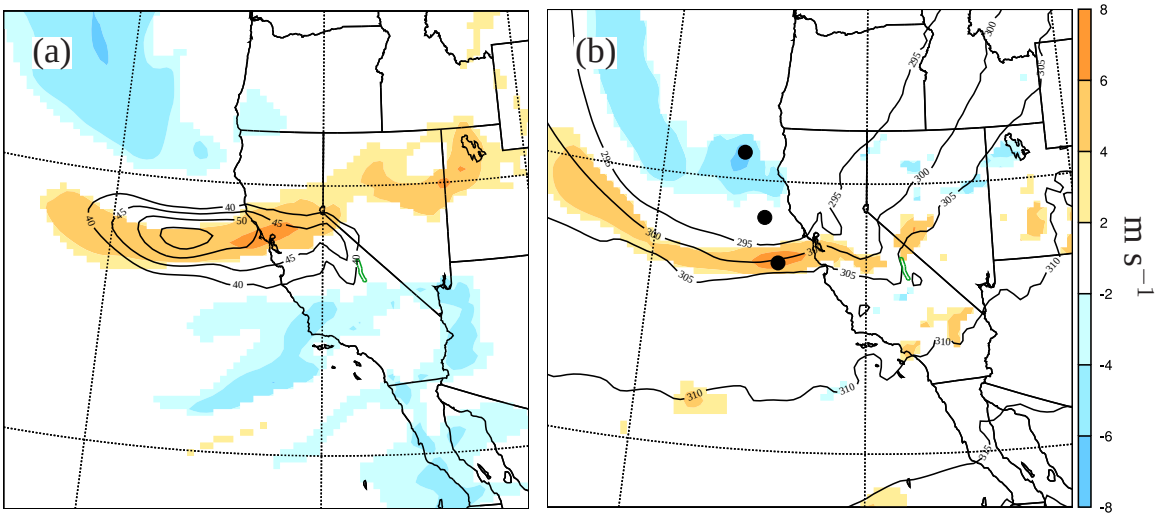

Figure 3.13: The ensemble sensitivity of the IOP-13, 7-hr forecast of the wind speed in the Owens-Valley metric box to the 27-km domain analysis of (a) wind speed at $z = 7$ km and (b) Brunt-Väisälä frequency at $z = 4$ km. The time of the analysis is 00 UTC, 17 April. The sensitivities have been multiplied by an ensemble standard deviation so that the dimensions are m s^{-1} for each plot. Also plotted are the analyzed (a) 7 km wind speeds and the (b) 4 km potential temperature. The location of the metric box is indicated by the green lines. The dots in (b) represent the Brunt-Väisälä perturbation locations.

tending from the San-Francisco Bay westward over the Pacific Ocean. This sensitivity is focused along a strong meridional gradient of θ (contours) which is associated with an upper-level front. North-south oriented vertical cross-sections through the sensitive area shows that the sensitive region tilts upward to the north (not shown). The maximum region of positive sensitivity predicts that a $\pm\sigma$ change of N will lead to over a ± 7 m s^{-1} change of the 7-hr downslope-wind forecast. An area of negative sensitivity is located to the north of the strong θ gradient. In this region a $\pm\sigma$ change in the N is expected to produce a ∓ 6 m s^{-1} change of the 7-hr downslope wind forecast. In between the two points is a region in which ESA predicts no statistically significant sensitivity.

In order to test the sensitivity-analysis predictions, a set of experiments are performed in which the ensemble is perturbed and integrated forward to give an evolved downslope-wind perturbation. In order to develop balanced initial perturbation, the ensemble statistics are used to spread information around the model domain for a $\pm\sigma$ perturbation at a single point. If $\bar{\mathrm{x}}^a$ is the N$\times$1 ensemble mean analysis state vector, $\mathbf{P}^a$ is the N$\times$N analysis-error covariance matrix, and h is a 1$\times$N vector which maps the the state vector onto the single perturbation location, then the ensemble-mean perturbation can be written as

$$\bar{\mathbf{x}}^p = \bar{\mathbf{x}}^a + \mathbf{P}^a\mathbf{h}^T\left(\mathbf{h}\mathbf{P}^a\mathbf{h}^T\right)^{-1}. \tag{3.2}$$

In other words, the initial perturbation of the mean field is a linear regression of a single point perturbation onto the model field using the ensemble analysis statistics. The analysis ensemble is then re-centered around this mean according to

$$\mathbf{x}^p_n = \bar{\mathbf{x}}^p + \mathbf{x}'^a_n, \tag{3.3}$$

where x'^a_n is the nth ensemble perturbation of the original analysis. This perturbation method ensures the ensemble variability is left unchanged while the mean is shifted. The perturbation is constructed on the 3 nests and the 70

members are integrated forward to give an evolved perturbation.

Figure 3.14a shows $\bar{\mathrm{x}}^p - \bar{\mathrm{x}}^a$ of the Brunt-Väisälä frequency at 4-km ASL due to a $\pm\sigma$ perturbation of N at the southern black dot in Fig. 3.13b. This location corresponds to an area of large positively correlated sensitivity associated with the upper-level front. The linear regression spreads the perturbation of N anisotropically with large concentrations located north of the initial perturbation and small negative perturbations to the south. Note that the linearity leads to a symmetric positive and negative initial perturbation. In addition, the covariance perturbs other fields in a manner consistent with the N perturbation. For example, Fig. 3.14b shows the initial perturbation of the U field at 7-km ASL associated with this change in static-stability. Note that the N perturbation projects onto the regions U sensitivity.

The evolution of the N and U fields for the $\pm\sigma$ perturbation is shown for the 7-hr forecast in Figs. 3.14cd. These are computed by integrating the 70 positively and negatively perturbed ensemble members, computing the ensemble mean, and calculating the perturbation from the control run. Apparent is the coherent structure of the perturbation that has remained intact over the course of the integration. Additionally, the positive and negative perturbations are relatively symmetric which suggests that the error growth dynamics for the synoptic-scale flow are linear.

Figure 3.15a shows the evolution of the ensemble mean Owens-Valley metric for the positive- (thick blue) and negative-perturbation (thick red) forecasts as well as the control forecast (black). Due to the distance of the perturbations from the Sierra-Nevada, the first 4-hrs of the forecast are characterized by differences between the control and perturbed runs less than 1 m s^{-1}. As the forecast continues the perturbations grow but are generally less than 5 m s^{-1}.

The ESA predicted downslope-wind response due to perturbing the N field at the southern black dot is also plotted in Fig. 3.15a (thin lines). Forecast

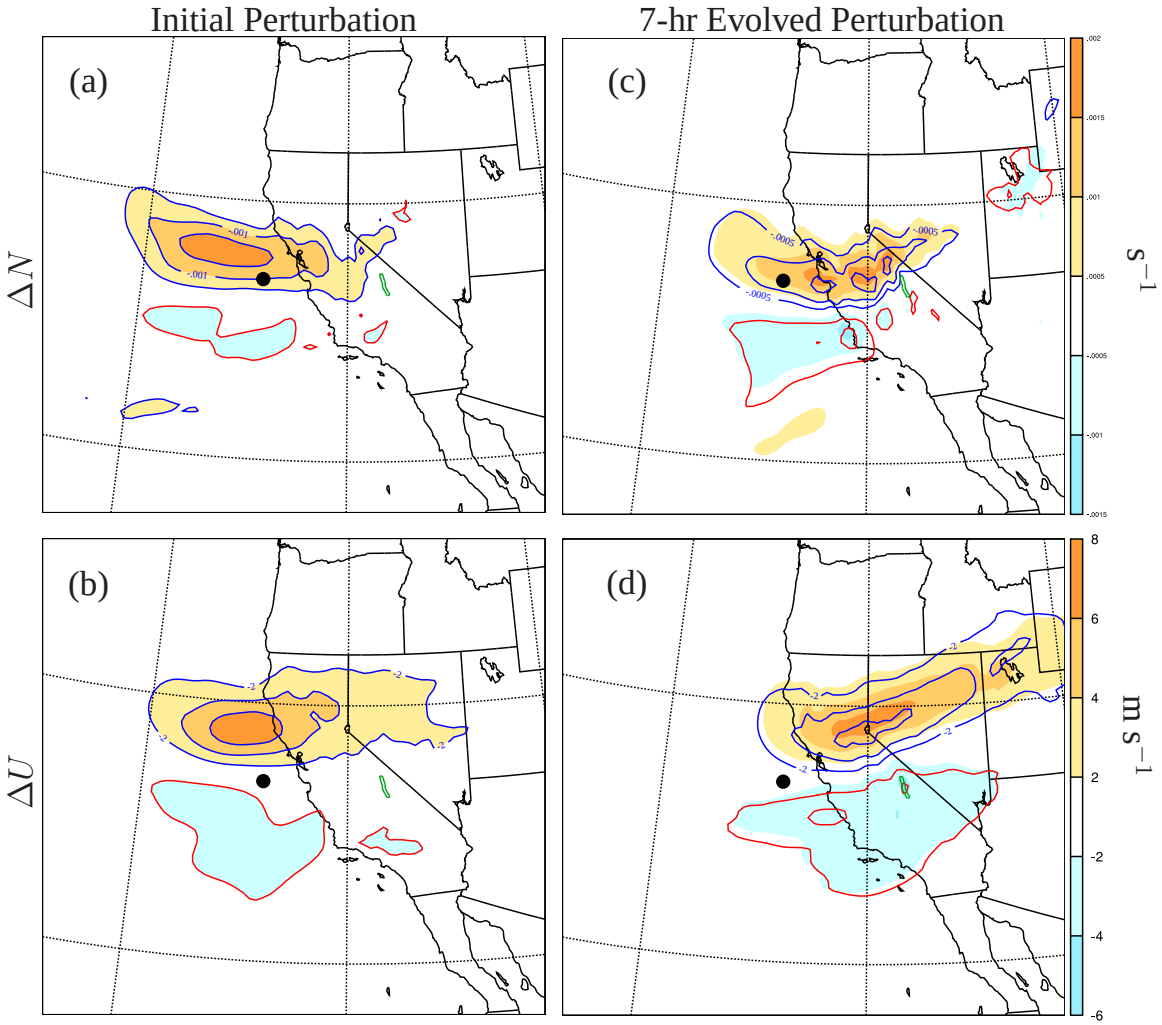

Figure 3.14: The IOP-13 initial perturbation of the (a) 4-km Brunt-Väisäsä frequency and (b) 7-km wind speed on the 27-km domains associated with a $\pm\sigma$ perturbation of N 4-km ASL at the black dot. The positive perturbations are colored and the negative perturbations are contoured. The evolved perturbation as evident from the 7-hr ensemble forecast of the (c) 4-km Brunt-Väisäsä frequency and the (d) 7-km wind speed.

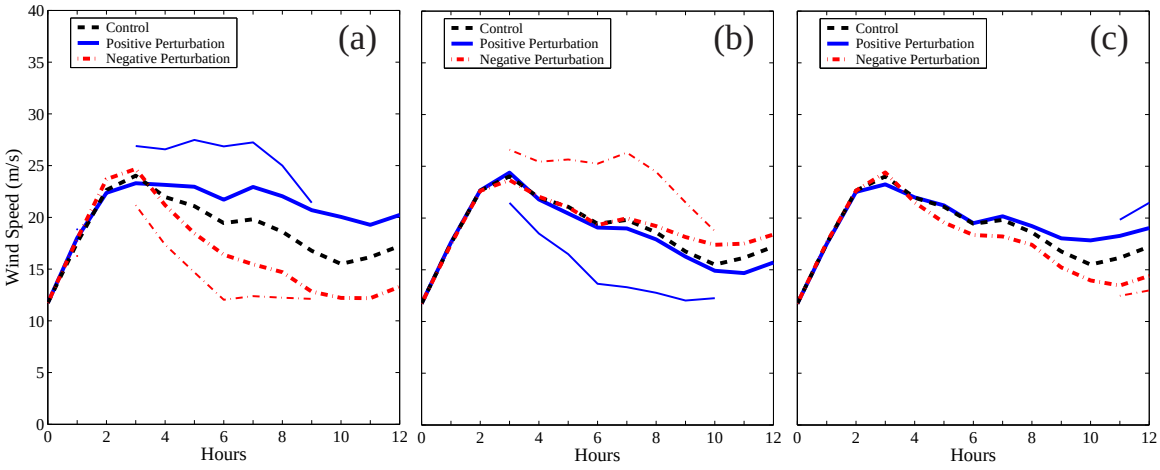

Figure 3.15: The evolution of ESA predicted response (thin-lines) for $\pm\sigma$ perturbation of the 4-km Brunt-Väisälä frequency at the (a) southern, (b) northern, and (c) central black dots in Fig. 3.13b. Also plotted is the actual downslope-wind response (thick lines) associated with perturbing the 4-km Brunt-Väisälä frequency $\pm\sigma$ at the three dots and integrating the ensemble. The unperturbed control run is shown with the black line.

times at which the ESA prediction is not statistically significant at the 95% confidence level are not plotted. While the ESA predicted response is able to capture the sign of the actual response, it substantially over estimates its magnitude. For example, ESA predicts that a positive σ perturbation of N at the initial time will lead to a 7 m s^{-1} increase of the downslope winds for the 7-hr forecast. In actuality, perturbing the ensemble analysis leads to a 3–4 m s^{-1} increase of the downslope wind response. Similarly, ESA prediction over estimates the magnitude of negative perturbation.

To further test ESA downslope-wind-sensitivity predictions, several additional tests are performed in which the 4-km Brunt-Väisälä frequency is perturbed at the northern and the central black dots shown in Fig. 3.13b. As apparent in Fig. 3.13b, according to ESA, the northern black dot is negatively correlated with the 7-hr downslope wind forecast and the central dot is a nodal point

with no statistically significant sensitivity. Figures 3.15b and c show the actual response associated with perturbing the 4-km Brunt-Väisälä frequency by $\pm\sigma$ at the northern and central points, as well as ESA predicted response. The ESA significantly over-estimates the sensitivities associated with the northern black dot (Fig. 3.15b). Almost no sensitivity is associated with actually perturbing the ensemble, whereas, ESA predicts up to a 7 m s^{-1} sensitivity. For the central dot (Fig. 3.15c), ESA predicts no statistically-significant sensitivity for the first 10-hrs of the forecast, the actual response is weakly sensitive to the initial perturbation, especially for the negative perturbation and after 7 hrs. Contrary to the prediction of ESA, the overall character of the sensitivity associated with perturbing the ensemble is somewhat greater at the central point than at the northern suggesting that ESA is unable to capture the correct spatial structure of the downslope wind sensitivity.

One additional experiment is performed for a second event: the 18 UTC, 25 March forecast associated with IOP-6. Figure 3.16 shows the ensemble derived 4-hr downslope-wind sensitivities to the 7-km ASL wind speed and the 4-km ASL Brunt-Väisälä frequency. While the qualitative structure of the sensitivity pattern is similar to the IOP-13 case, several key differences are apparent. The region of 7-km-wind-speed sensitivity (Fig. 3.16a) is located on either side of the jet, as opposed to directly over the jet, suggesting that stronger/weaker downslope winds would occur if the jet translates to the north/south. Similarly, the 4-km N sensitivities are displaced from the strong θ gradient with the largest sensitivities located north of the upper-level front.

The initial N field is perturbed $\pm\sigma$, 4-km ASL at the black dot in Fig. 3.16b. This perturbation is regressed onto the model variables according to (3.2) and the new sets of initial conditions are integrated forward in time in an identical manner to the IOP-13 case. The actual evolution of the downslope-wind response for the perturbed members and the response predicted by ESA is shown

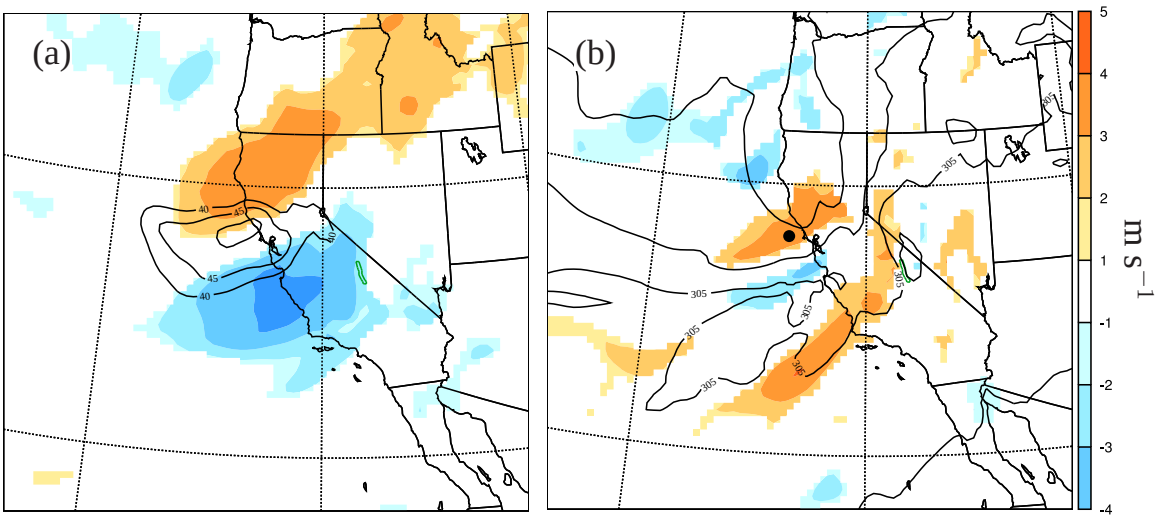

Figure 3.16: Same as Fig. 3.13 except that the sensitivity of the the IOP-6, 4-hr forecast that was initialized 18 UTC, 25 March. Note that the contour interval is half that of Fig. 3.13.

as a function of model forecast time in Fig. 3.17. While the differences between ESA-perturbation prediction and the actual perturbation is smaller than the IOP-13 case, ESA perturbation prediction is roughly 50% stronger than the actual perturbation.

The ESA method appears to significantly over estimate the magnitude of the downslope wind sensitivities. In addition, a non-trivial response is found at a nodal point, implying the shortcomings of ESA are not only quantitative over-estimates of the degree of sensitivity but that it also fails to represent the correct spatial pattern. One possible explanation for the poor performance of ESA is that sampling errors associated with the finite ensemble result in inaccurate statistical relationships between the metric and the synoptic-scale variables. However, the statistical significance tests performed indicate that sampling error is not an issue. Another possibility is the non-linear nature of the downslope wind response. This can, in part, be understood by consid-

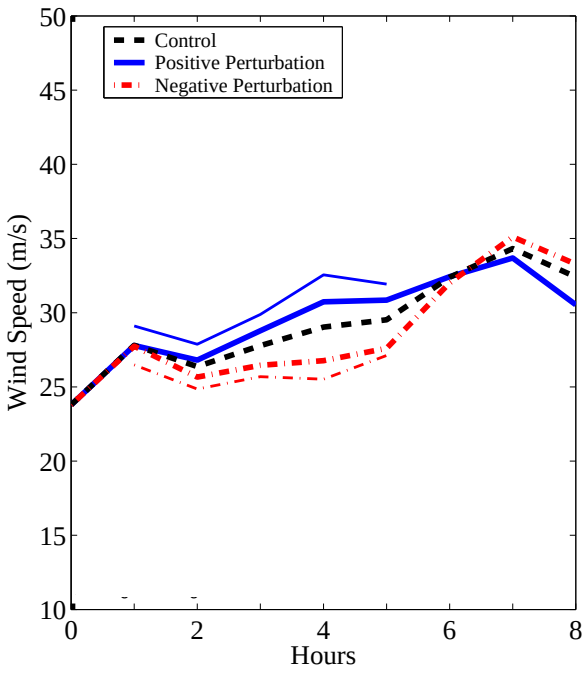

Figure 3.17: The same as Fig. 3.15 except for the IOP-6 simulation. The location of the perturbation is indicated by the black dot in Fig. 3.16b and is 4-km ASL.

ering the ensemble distributions associated with the downslope windstorms. Figure 2.15a shows the ensemble distribution for the 6-hr, IOP-13 forecast considered in this section. The non-linear nature of the downslope wind response leads to a non-Gaussian distribution of the lee-side winds. This non-Gaussian distribution clearly violates the assumption of the ESA method. While ESA has been shown to be beneficial for synoptic-scale motions, the highly non-linear nature associated with the severe downslope windstorms limits its usefulness for this particular application. We therefore do not consider ESA for the remainder of the thesis.

Chapter 4

DATA ASSIMILATION IN COMPLEX TERRAIN

One of the primary benefits of using ensemble based data assimilation is the ability to estimate the background-error statistics with the time-dependent ensemble members. As a result, the way in which observational information is spread around the numerical domain is both flow dependent and consistent with the model dynamics. In this chapter the ability of the flow-dependent background-error statistics to capture physically meaningful mesoscale covariance relationships associated with flow interacting with complex terrain will be explored.

4.1 Experimental Setup

As with the previous two chapters, the numerical model is COAMPS (Hodur, 1997, appendix A). In this chapter the horizontal advective terms are computed with a fourth-order finite difference approximation. The numerical-domain setup is identical to that in the previous two chapters with one exception, a 1-km domain is centered over the Owens Valley and High-Sierra to further resolve the motions associated with the mountain wave and downslope winds. The location of the four domains is indicated schematically in Fig. 4.1.

A deterministic square-root version of the EnKF, described in Whitaker and Hamill (2002) is used for data assimilation. Several high resolution experiments were performed during the TREX (Grubišić et al., 2008) in which observations of ACARS, ASOS, cloud-track winds, and radiosonde data were assimilated by the EnKF every 6 hrs. Due to the high computational costs of running

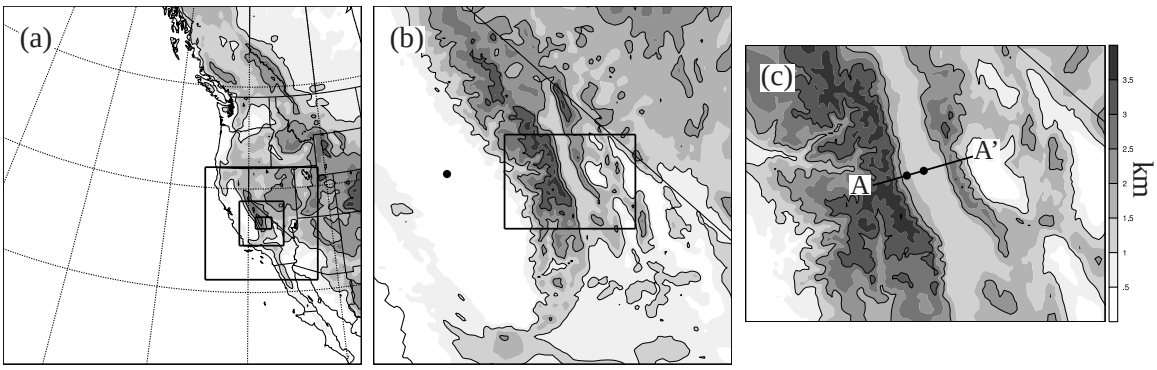

Figure 4.1: The topography on the (a) 27-, (b) 3-, and (c) 1-km domain. The locations of the 9-, 3-, and 1-km domains are shown by the solid lines in (a). The dots in (b) and (c) indicate the locations of the hypothetical surface observations used to calculate the Kalman gain. The solid line in (c) shows the location of the AA' vertical cross-section.

the full ensemble on the high-resolution domains, the 9-, 3-, and 1-km experiments were limited to periods of strong mountain-wave activity. In this chapter we examine the analysis increments that would be associated assimilating surface wind observations adjacent to the Sierra-Nevada mountains for one such period: IOP 6 which occurred 25-26 March, 2006.

In order to avoid initializing the ensemble multiple times during the TREX SOP, the 27-km experiment (described in appendix C) is used to initialize the higher resolution forecasts during periods of interest. For the high-resolution experiments, the ensemble is initialized in sequence from the 9-km mesh to the 1-km mesh by interpolating the members from the next-higher-resolution domain. Data assimilation is then performed by the EnKF independently on each numerical mesh every 6 hrs. For the IOP-6 experiment described in this study, the 9-km mesh is initialized from the 27-km mesh at 06 UTC, 24 March, 2006, the 3-km mesh is initialized from the 9-km mesh at 00 UTC, 25 March, 2006, and the 1-km mesh is initialized from the 3-km mesh at 06 UTC, 25 March 2006.

4.2 Analysis Increments

In this section, the ensemble mean analysis increment due to hypothetical surface zonal-wind observations is explored. If $\bar{\mathrm{x}}^b$ is the ensemble mean model forecast of a state vector containing all the model variables at every grid point, y^o is a vector containing observations, and $\mathbf{H}$ is a matrix which maps the the state vector onto the observational space (e.g. linear interpolation), then the EnKF update equation for the ensemble mean analysis increment is

$$\Delta\bar{\mathrm{x}} = \bar{\mathrm{x}}^a - \bar{\mathrm{x}}^b = \mathbf{K}(\mathrm{y}^o - \mathbf{H}\bar{\mathrm{x}}^b) \tag{4.1}$$

where $\bar{\mathrm{x}}^a$ is the mean posterior model state associated with assimilating the observations y^o, and

$$\mathbf{K} = \mathbf{P}^b\mathbf{H}^T\left(\mathbf{H}\mathbf{P}^b\mathbf{H}^T + \mathbf{R}\right)^{-1} \tag{4.2}$$

is the Kalman gain matrix. The flow-dependent background-error covariances are specified with $\mathbf{P}^b$ and the observational-error covariance is specified with $\mathbf{R}$. The innovation is the differences between the observations y^o and the ensemble mean estimate of the observations $\mathbf{H}\bar{\mathrm{x}}^b$ and is defined to be $(\mathrm{y}^o - \mathbf{H}\bar{\mathrm{x}}^b)$. In principal, if the error distributions are normally distributed, any data assimilation system which utilizes (4.1) with the weight matrix (4.2) will optimally combine the model background state $\bar{\mathrm{x}}^b$ with the observations y^o and minimize the analysis-error covariance (appendix B). However, in practice, $\mathbf{P}^b$ can be highly flow dependent and is not easily specified *a priori*. This may be especially true for mesoscale flows in complex terrain where $\mathbf{P}^b$ can vary rapidly with time and be extremely anisotropic. The advantage of using ensembles for data assimilation is that the background-error covariance are estimated as $\mathbf{P}^b = \left\langle \mathrm{x}^b\mathrm{x}^{b^T} \right\rangle$, where the angled brackets indicate an expected value over the ensemble members. In this way the model updates are both flow dependent and consistent with the model dynamics.

In the following, the structure of $\Delta\bar{\mathbf{x}}$ in regions adjacent to the Sierra-Nevada is explored for individual hypothetical near-surface zonal-wind observations. The hypothetical observations are constructed so that $|y^o - \mathbf{H}\bar{\mathbf{x}}^b| = 1$ m s^{-1}. In other words, the zonal-wind innovation for the single surface observation is 1 m s^{-1} stronger in either the easterly or westerly direction. Equivalently, we could interpret this as the structure of a segment of the $\mathbf{K}$ matrix for a single observation. For a single observation, $\mathbf{R}$ and $\mathbf{H}\mathbf{P}^b\mathbf{H}^T$ are scalars allowing (4.2) to be easily be evaluated. The observational error variance for the single observation is assumed to be $R = 6.25$ m^2 s^{-2}. This choice controls the impact of the observation compared to the background forecast. If the background-forecast variance $\mathbf{H}\mathbf{P}^b\mathbf{H}^T$ is large compared to R then the analysis increment will weight more of the observation. If, on the other hand, R is small compared to $\mathbf{H}\mathbf{P}^b\mathbf{H}^T$ then the analysis increment will weight less of the observation. For each observation below we will compare $\mathbf{H}\mathbf{P}^b\mathbf{H}^T$ to R. We limit our focus to the mean increment on the high-resolution domains (3- and 1-km).

4.2.1 Increments at $t = 6$ hrs

Consistent with the length of the assimilation cycle, we consider analysis increments for the 6-hr forecast initialized 12 UTC, 25 March, 2006. This period is chosen because a number of interesting orographically induced mesoscale phenomenon occur throughout the simulation period, including: upstream blocking in San Joaquin Valley, downslope winds in the Owens Valley, and mountain waves forced by the Sierra-Nevada mountains. The purpose here is to demonstrate that assimilating surface wind observations with the EnKF can provide realistic analysis increments that are consistent with the theoretical understanding of orographic flows.

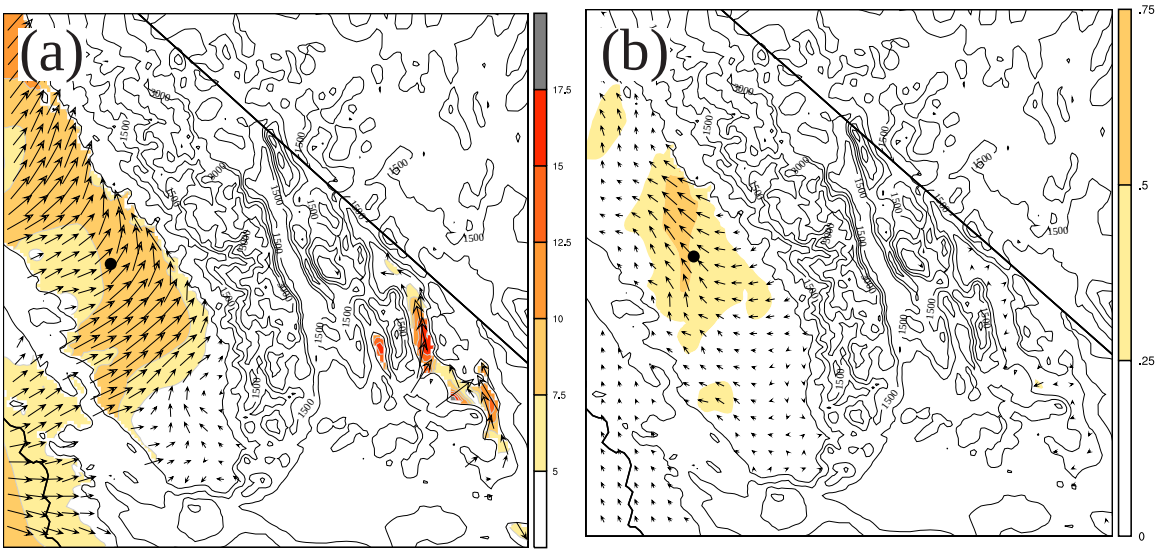

Figure 4.2: (a) The ensemble mean wind speed and wind vectors 250 m ASL at $t = 6$ hrs on the 3-km domain. The contour interval is 2.5 m s^{-1}. (b) The analysis increment of the wind field (vectors) due to a 1 m s^{-1} decrease of the zonal wind at $t = 6$ hrs, 10-m AGL at the black dot. The magnitude of the increment is indicated by the shading.

Upstream Blocking

We begin by examining the analysis increment $\Delta\bar{\mathrm{x}}$ in the presence of orographic blocking. The ensemble mean, 6-hr forecast of the 500 m wind speed and direction is shown from the 3-km domain in Fig. 4.2a. In the western portions of the San Joaquin Valley the low-level flow is perpendicular to the Sierra-Nevada mountains. However, as the air-stream approaches the barrier it is diverted to the north in a direction parallel to the terrain. Forward trajectories launched at $t = 5$ hrs throughout the San Joaquin Valley (not shown) indicate that the low-level flow is diverted northward before passing over the crest near Mammoth, CA.

While terrain parallel jets associated with flow blocking can be a balanced phenomenon, it is not likely that static-covariances designed for large-scale

flows would be able to capture the appropriate mesoscale structures related to the fine details of the topography. The flow dependence of the EnKF is, however, able to capture a physically meaningful increment associated with a surface wind speed observation. Figure 4.2b shows $\Delta\bar{\mathrm{x}}$ of the 500 m wind field that would occur if a zonal wind observation, 1 m s^{-1} weaker than the ensemble mean, was taken 10 m AGL at the black dot in Fig. 4.2. For this location $\mathbf{H}\mathbf{P}^{b}\mathbf{H}^{T} \approx 1.6$ m^2 s^{-1} suggesting that the observation will be weighted less than the background forecast. Apparent in Fig. 4.2b is that weaker terrain perpendicular flow at the surface station leads to analysis increments which broaden the upstream extent of the decelerated region. Additionally, the wind speed increments decay with height and are negligible above crest-level (not shown), which would be expected for a low-level response of blocked flow.

Downslope winds and mountain waves

We turn our attention now to the analysis increments $\Delta\bar{\mathrm{x}}$ associated with wind observations in the Owens Valley. As mentioned previously, downslope winds and mountain waves were present in the 6-hr COAMPS forecast so the focus will be limited to the structure of the increments associated with these features. Figure 4.3 shows the zonal-wind increment from the 1-km domain along the AA' vertical cross-section indicated in Fig. 4.1c. The increments are due to the assimilation of two hypothetical zonal-wind observations separated by 8.5 km: one on the lee-slope of the Sierra-Nevada and one at the base of the Owens Valley. The observation locations are coincident with two mesonet stations in place for the TREX SOP and depicted in Fig. 4.1c: Desert Research Institute (DRI) station 7 (on the lee-slope) and DRI station 10 (on the Valley floor). Since we are only interested in the spatial structure of the individual analysis increments, the impact of the each observation is is considered separately. For both stations we consider an observation of zonal wind that is 1 m s^{-1} stronger

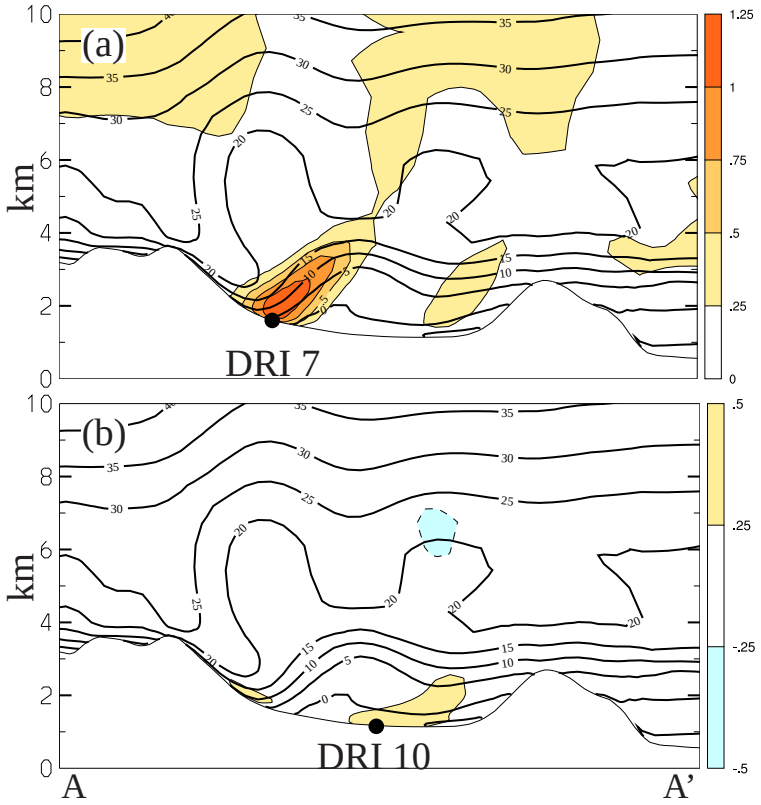

Figure 4.3: The analysis increment (color filled) at $t = 6$ hrs of the zonal wind along the AA' vertical cross-section on the 1-km domain due to a 1 m s^{-1} increase of the zonal wind, 10-m AGL at the black dot in (a) and (b). The ensemble mean zonal wind is also plotted with a contour interval of 5 m s^{-1}.

than the ensemble mean. For the DRI-7 station $\mathbf{H}\mathbf{P}^b\mathbf{H}^T \approx 25$ m^2 s^{-1} and for the DRI-10 station $\mathbf{H}\mathbf{P}^b\mathbf{H}^T \approx 3.5$ m^2 s^{-1}. This suggests that the observation will be weighted more at the DRI-7 station compared to the DRI-10 station. The higher-resolution domain is used because discretization errors associated with poorly resolved waves can result in significant over-amplification of the mountain-wave and downslope-wind response leading to large model error and non-representative increments (chapter 2).

In addition to the analysis increments, the ensemble mean zonal wind along the cross-section is plotted in Fig. 4.3. A tongue of strong downslope flow extends down the lee-slope of the Sierra-Nevada and into the Owens Valley with the strongest winds directly upstream of the DRI-7 station. East of the DRI-7 station the zonal winds are considerably weaker. The zonal-wind analysis increment associated with the DRI-7 station tilts downstream with height and is concentrated along the strong gradient of zonal flow (Fig. 4.3a). This increment shifts the entire stream of strong downslope flow further down the lee-slope. Moreover, the small analysis increment located in the upper troposphere suggests that stronger cross-barrier flow is associated with the more intense downslope wind response. In contrast, assimilation of the DRI-10 observation has very little impact on the structure of the downslope flow (Fig. 4.3b). The zonal-wind increment is small and localized to regions immediately adjacent to the observation. The large variation of $\Delta\bar{\mathrm{x}}$ between the two observations demonstrates that flow dependent covariances can be crucially important in regions of complex terrain.

Associated with the strong downslope flow is a moderately strong mountain wave propagating away from the Sierra-Nevada crest. Figure 4.4 shows the ensemble mean vertical velocity and the analysis increment in w due to the same two zonal-wind-speed observations. As evident in the figure, the mountain wave is oriented downstream with alternating regions of positive and negative

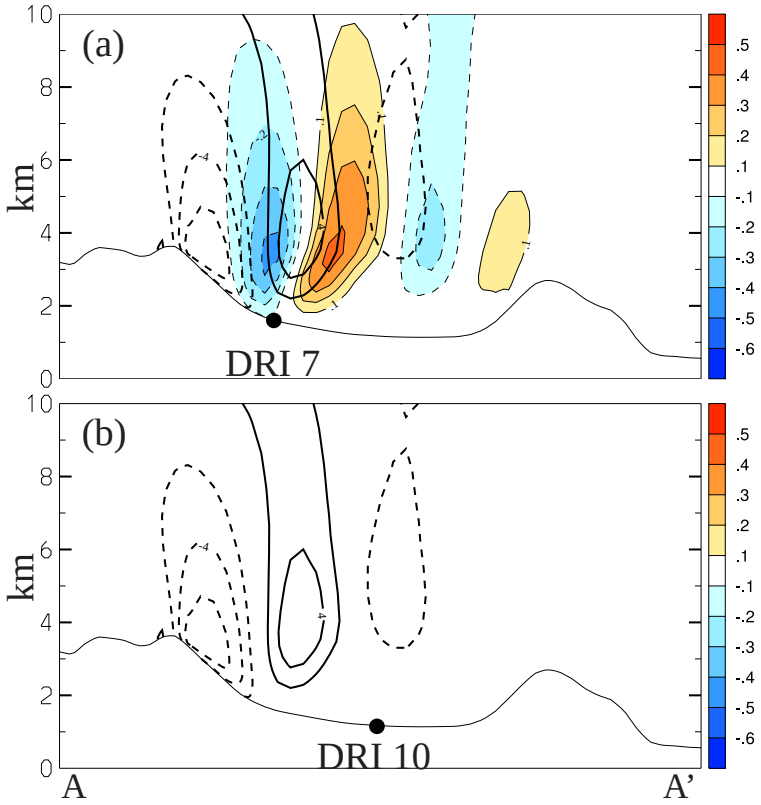

Figure 4.4: The analysis increment at $t = 6$ hrs of the vertical velocity along the AA' vertical cross-section on the 1-km domain due to a 1 m s^{-1} of increase of the zonal wind, 10-m AGL at the black dot in (a) and (b). The ensemble mean vertical velocity is also plotted for reference with a contour interval of 2 m s^{-1}.

vertical velocity with the maximum intensity close to 6 m s^{-1}. Assimilation of the DRI-7 zonal-wind observation (Fig. 4.4a) leads to a vertical-velocity increment which alternates between between positive and negative phases and is shifted approximately 90° from the up-down motions of the mountain wave. Additionally, the increments decay with height and are localized to regions where there is an appreciable mountain-wave signature. This increment represents a downstream shift of the mountain wave which result in the region of strong flow underneath the first downward phase of the wave extending further down the lee slope. In contrast, the vertical-velocity analysis increment for the DRI-10 station is less than 0.05 m s^{-1}, which is smaller than the contour interval. Apparently, surface wind speed observations at $t = 6$ hrs along the bottom of the Owens Valley have a minimal effect on the mountain-wave structure.

The anisotropic nature of the background-error covariance is also evident in the horizontal. Figure 4.5 shows the zonal-wind increment at 250 m AGL for the same two surface observations. The increment for the DRI-7 observation extends along the lee-slope over the entire north-south extent of the Owens Valley (Fig. 4.5a). This is not completely unexpected since the Sierra-Nevada are a quasi two-dimensional mountain range and the structure of the mountain-wave should be only slowly varying along a direction parallel to the ridge line. Nevertheless, it is interesting that the EnKF is able to detect this extremely anisotropic covariance relationships along the lee-slope. The DRI-10 observation, further down the slope, has little impact on the 250 m zonal wind (Fig. 4.5b). This implies that the correlation length scale for this observation is very short.

4.2.2 Increments at $t = 9$ hrs

One of the main advantages of using the EnKF is the flow-dependent nature of the background-error covariances. In the previous section it was demonstrated

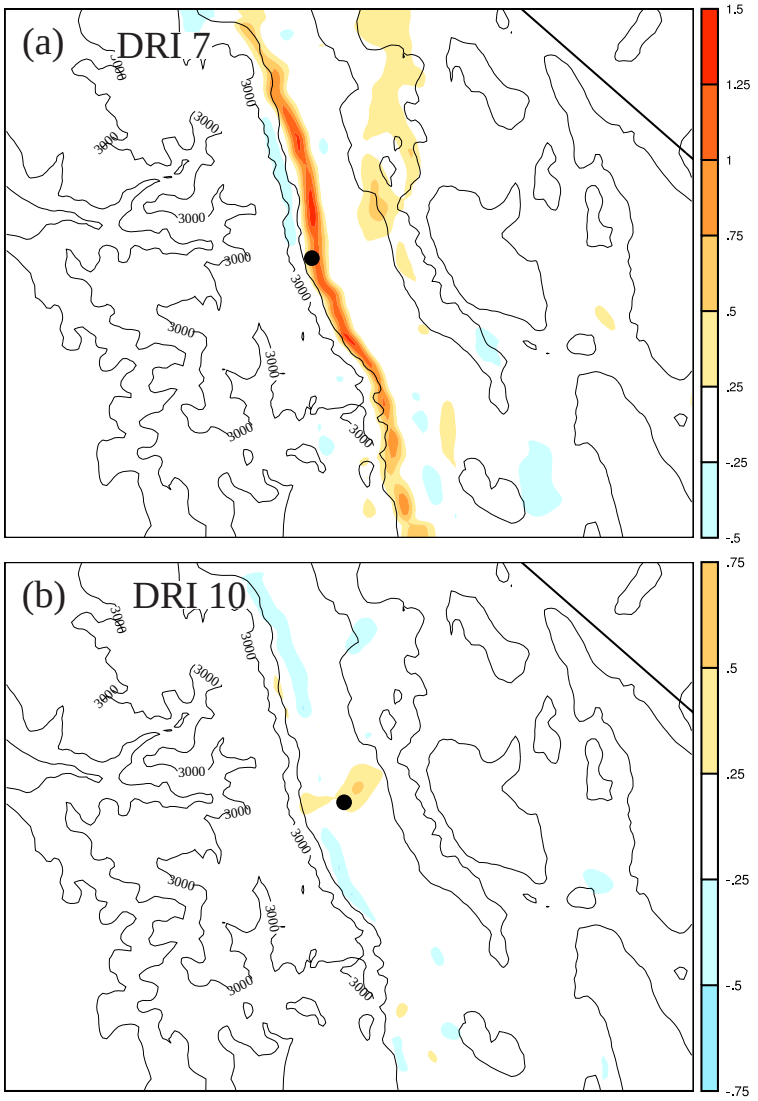

Figure 4.5: The 6-hr analysis increment on the 1-km domain of the zonal wind 250 m AGL due to a 1 m s^{-1} increase of the zonal wind, 10-m AGL at the black dots in (a) and (b).

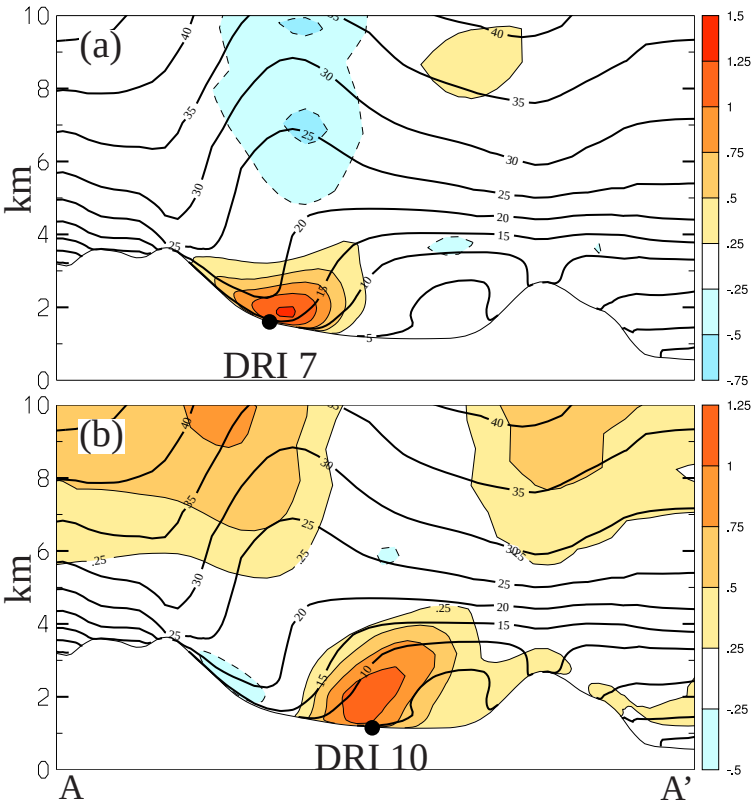

Figure 4.6: Same as Fig. 4.3, except for $t = 9$ hrs.

that large variations in the background-error covariance structure could occur over very short distances. In this section, the time-dependent nature of the background-error covariance is explored by considering how the analysis increments change over a short 3-hr interval.

The zonal-wind increment associated with the DRI-7 and DRI-10 hypothetical zonal-wind-speed observations for the 9-hr COAMPS forecast is shown along the AA' vertical cross section in Fig. 4.6. Also plotted in both panels of Fig. 4.6 is the ensemble mean zonal wind along the cross section. A strong jet extends down the lee slope with the wind speeds exceeding 15 m s^{-1} deep into the Owens Valley. Compared to the 6-hr forecast (Fig. 4.3), the strong wind extending further down the slope, however, at the base of the Valley, the en-

semble mean zonal winds remain relatively calm. Additionally, the ensemble variance at the DRI-10 has increased drastically and is now $\mathbf{HP}^b\mathbf{H}^T \approx 25$ m^2 s $^{-1}$ which implies that the observation will be heavily weighted.

For the observation associated with the DRI-7 station (Fig. 4.6a) the amplitude of the analysis increment is similar to that of the previous time (Fig. 4.3a), however, the structure varies considerably. For the 9-hr forecast the analysis increment remains attached to the lee-slope but extends laterally up and down the lee slope. Further aloft directly above DRI-7, the wind speed increments are negative, consistent with an increase in wave amplitude associated with stronger downslope winds. Further down the slope, the analysis increment associated with the DRI-10 observation (Fig. 4.6b) is considerably different than the analysis increment for the 6-hr forecast (Fig. 4.3a). A large positive increment covers a broad portion of the Owens Valley below the Sierra-Nevada crest. Furthermore, relatively large increments are apparent above 6 km indicating that the stronger downslope winds at the base of the Owens Valley are positively correlated with stronger zonal flow aloft. The correlation length scale has increased substantially for the DRI-10 observation compared to the 6-hr forecast.

Associated with the stronger downslope wind storm at hour 9 is a strong mountain wave. Figure 4.7 shows the ensemble mean vertical velocity, as well as the vertical-velocity increment along the same AA' vertical cross-section. The positive phase of the lee-wave extends over the central portion of the Owens Valley, resulting in a longer horizontal wavelength when compared to the 6-hr forecast. Furthermore, the maximum vertical velocity is less than 4 m s^{-1}, which is somewhat weaker than 6-hr forecast. For both stations the 9-hr vertical-velocity increment differs considerably from the 6-hr forecast. The vertical velocity increment for the DRI-7 observation is shown in Fig. 4.7a. As with the 6-hr forecast, the increment is nearly 90° out of phase, suggesting that the

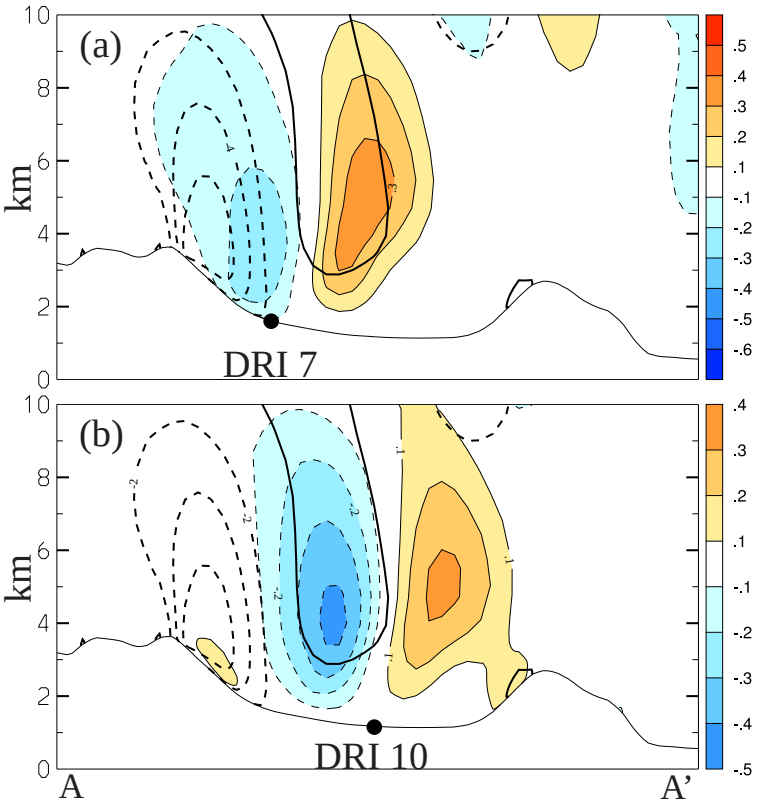

Figure 4.7: Same as Fig. 4.4, except for $t = 9$ hrs.

stronger wind observation shifts the lee-wave downstream, however, the horizontal scale of the increment is broader. The largest differences between the 6- and 9-hr analysis increments are associated with the DRI-10 observation (Fig. 4.7b) where a positive-negative couplet is located directly over the station. The increment is nearly 180° out-of-phase with the vertical-velocity field which decreases the positive vertical velocity component over the central portion of the Owens Valley. This reduces the tendency of the high-speed flow to separate from the surface and allows these winds to extend further down the lee slope. In the horizontal plane, the 250 m AGL analysis increment associated with DRI-10 at hour 9 has a similar crest parallel structure to the DRI-7 increment at hour 6 as shown in Fig. 4.5 (not shown). This implies that the correlation length scale is much larger at DRI-10 for the 9-hr forecast than for the 6-hr forecast. Such rapid variations in the correlation length scale may make distance dependent covariance localization difficult when assimilating observations in complex terrain.

Chapter 5

CONCLUSIONS

This thesis considers several factors relating to the prediction and predictability of mountain waves and downslope winds and represents one of the first attempts to systematically document the variability of downslope-wind forecasts associated with expected levels of synoptic-scale uncertainty in a fully non-linear, three-dimensional NWP mesoscale model. Throughout the thesis the focus is on real-world situations which represent typical forecasting challenges in regions of complex terrain.

The predictability of downslope-wind and mountain-wave forecasts is explored with a fully non-linear, non-hydrostatic, high-resolution NWP model. The model is used to generate an ensemble of 70 different initial conditions for two prototypical downslope-wind events from the TREX SOP: IOP 6 (25-26 March, 2006) and IOP 13 (16-17 April, 2006). The IOP-6 event was characterized by a large-amplitude mountain wave with upper-level tropospheric wave breaking and severe downslope winds. In contrast, wave breaking was not present for the IOP-13 simulations, instead, the strong winds were generated by a layer of high static stability beneath an upper-tropospheric layer of low stability.

An EnKF data assimilation system is used to generate the initial ensemble perturbations for the IOP-6 and the IOP-13 forecasts. In this way the ensemble of initial conditions represents uncertainty that would be present in operational NWP forecasting systems given an imprecise specification of both the observations and the background estimate of the atmosphere. The growth

of the ensemble variance during each forecast represents the degree to which the downslope wind event is sensitive to the expected uncertainty of the initial conditions.

For the wave-breaking simulations (IOP-6), initial-condition errors grow rapidly leading to large variability of the downslope-wind forecast. Quantifying the variability as the difference of the 6-hr downslope-wind forecast between the strongest and weakest-10 subset means shows that differences as large as 28 m s^{-1} are possible on the lee-slope. For the strong subset, an extensive region of decelerated flow and turbulent mixing extends through a deep layer of the troposphere suggesting that wave breaking is a dominant mechanism for the formation of the strong downslope winds. The majority of the error growth occurs between the 3 and 6-hr forecast demonstrating that the predictive time scale for this wave-breaking event is shorter than 3-hrs. A representative upstream sounding, 1-hr prior to the strongest downslope winds, shows that the difference of the cross-barrier wind speed, potential temperature, and Brunt-Väisälä frequency between the mean profiles for the strong and weak subsets is generally less than radiosonde observational errors. This demonstrates that very small differences in the upstream conditions can be responsible for large forecast uncertainty. The uncertainty can potentially limit the ability of deterministic NWP models to accurately predict downslope winds associated with mountain-wave breaking.

For the case with strong low-level static stability (IOP-13), in which wave breaking was not a large contributing factor, the predictability time-scale is somewhat longer. For the forecast initialized 18 UTC, 16 April, 2006, (and valid 06 UTC, 17 April), the differences between the strong and weak subsets grows to 23 m s^{-1} over the 12-hr forecast. In contrast, for the 6-hr forecast valid at the same time (and initialized 00 UTC, 17 April), the differences only reach 15 m s^{-1}. Additionally, the ensemble distributions of the downslope wind speed are

considerably different between the two forecasts. The 12-hr forecast is characterized by relatively low, uniformly distributed probabilities, whereas the 6-hr forecast contains a substantial peak in the distribution at 17.5 m s^{-1} with over twice the probability of the surrounding wind-speed bins. The slower error growth rates and decreased ensemble variability suggests that the IOP-13 layered-type downslope windstorm attains a longer predictive time-scale than the IOP-6 wave-breaking wind storm. Furthermore, a representative upstream sounding, 1-hr prior to the forecast time, shows that significant differences are readily apparent between the mean profiles for strong and weak subsets. For example, a 2-km deep layer of strong static-stability is present directly above crest level for the strong members, whereas, the crest-level static-stability is considerably weaker for the weak members. These differences are associated with the meridional displacement of an upper-level front and associated jet stream and suggest that an accurate prediction of these synoptic-scale features is necessary for accurate predictions of downslope winds.

Downslope-wind predictability limitations appear to be a function of the character of the mountain-wave response. On one hand, for the IOP-6 wave-breaking event, the strong sensitivity of the downslope wind response to the upstream conditions 1-hr prior to the event suggests that data would never be available to allow for the determination between the weak or strong storm. The predictability limitations for the clear-air turbulence simulated in this case are just as short. These limited predictive time scales are consistent with the two-dimensional limitations associated with the wave-breaking regime presented in Doyle and Reynolds (2008). On the other hand, for the IOP-13 event where the upstream profile was characterized by static-stability layering, forecasting the downslope-wind response may be difficult 12-hrs in advance, however, sufficient differences existed in the upstream sounding to allow for a determination between the strong and weak storm 1-hr in advance.

The large forecast uncertainty can be accurately captured with an ensemble and ensemble data assimilation. The potential of the EnKF to assimilate mesoscale observations into high-resolution simulations was explored. It was shown that the flow-dependent background-error covariances were able to capture physically meaningful analysis increments both upstream and downstream of the Sierra-Nevada. For example, two hypothetical zonal-wind observations separated by 8.5 km produced significantly different analysis increments in both the zonal wind field and the vertical velocity field. One observation was located on the lee-slope of the Sierra-Nevada while the other was located at the base of the Owens-Valley. When the lee-slope observation was set to be 1 m s^{-1} stronger than the ensemble mean, the zonal-wind analysis increment was relatively large and concentrated along a narrow band extending along the length of the Sierra-Nevada lee slope. Additionally, the lee-slope observation produced a large analysis increment in the vertical velocity field, shifting the phase of the mountain-wave downstream. At the same time, a similar 1 m s^{-1} innovation at the base of the Owens-Valley had no appreciable impact on either the downslope wind speed, or the vertical velocity field. The analysis increment at this station varied strongly with time. This suggests that the correlation length scale is very short at the base of the Owens Valley. The same 1 m s^{-1} innovation 3-hrs later produced a large increment with a broader correlation length scale. The magnitude of the increment was similar to the magnitude of the increment at the lee-slope station.

The role of discretization errors in numerical solutions to flow over topography is explored with linear theory and non-linear NWP model simulations. Steady gravity waves are considered for scales ranging from non-hydrostatic, where errors are most likely to be found in high-resolution mesoscale NWP models, to inertial waves, that may be in error in coarser resolution global models. Analytic solutions to the discrete linear two-dimensional mountain-wave

problem are computed with the horizontal advective term approximated with first- through sixth-order finite differences. Surprisingly, for a non-hydrostatic mountain-wave ($\delta = 1.8$) forced by a $8\Delta x$-wide mountain, the vertical velocity in the second-order solution is 30% stronger than in the continuous solution. In contrast, for hydrostatic mountain waves ($\delta = 10$) forced by an $8\Delta x$-wide mountain, the the vertical velocities in the second-order solution are 7% weaker than those in the continuous solution. Decreasing the horizontal resolution further, so the mountain is resolved by 4 grid points, results in a 39% decrease in the amplitude of the hydrostatic wave.

The errors in mountain-wave amplitude are associated with errors in the discrete representation of the group velocity. In the non-hydrostatic solution, the group-velocity vector for the dominant wave forced by the coarsely resolved topography does not point sufficiently downstream. Instead, wave energy accumulates over the mountain peak, over-amplifying the mountain wave. Higher-order schemes are able to more accurately capture the downstream orientation of the group-velocity vector; the fourth- and sixth-order solutions for the $8\Delta x$-wide non-hydrostatic mountain are only 11% and 4% stronger than the continuous solution. In contrast, the amplitude of the discrete hydrostatic mountain wave is reduced because the group-velocity vector for the dominant wave forced by the coarsely resolved topography points erroneously upstream.

The practical implications of over-amplification on the structure and predictability of mountain waves and downslope winds is demonstrated in the context of a 70-member COAMPS ensemble simulation of a mountain-wave event over the Sierra-Nevada mountains of California. Here, an experiment is performed in which the horizontal advective scheme on a 3-km resolution mesh is switched from second- to fourth-order. In the second-order solution a very strong mountain-wave with vertical velocities in the ensemble mean exceeding 16 m s^{-1} is forced by the topography. Associated with the simulated mountain

wave is a severe downslope windstorm with ensemble mean winds close to 45 m s^{-1}. Switching to fourth-order-accurate advection, the mountain-wave amplitude decreases such that the ensemble mean vertical velocities do not exceed 8 m s^{-1}, and the downslope winds are reduced to approximately 15 m s^{-1}, which is close to the 12 m s^{-1} wind speed that was observed during the event. Additionally, the ensemble variability decreases substantially when switching from the second-order scheme to the fourth-order scheme. This is because many of the second-order solutions contain regions of substantial wave breaking which leads to strong downslope winds. In contrast, most of the fourth-order solutions do not contain wave-breaking and the downslope winds are much weaker.

Regardless of the mechanism responsible for strong downslope winds, the limited predictive time scales for the IOP-6 and IOP-13 events are considerably shorter than the optimistic view of mountain-wave predictability presented in Klemp and Lilly (1975). Although the predictability results for these two events may not generalize to all mountain-wave and downslope-wind scenarios, they demonstrate that the predictive limits of these features may be much shorter than previously thought. Future work should be directed towards sampling a larger set of downslope wind and mountain wave events. Furthermore, the difficulties that other downslope-wind forecasting attempts have experienced (e.g. Nance and Coleman, 2000), are possibly due, in part, to the large initial condition sensitivities demonstrated in this thesis. Specifying an ensemble of initial conditions with the EnKF is a way in which this uncertainty can be accounted for. Future high-resolution operational models will most likely need to use ensemble forecasting techniques to predict not only downslope wind, but the uncertainty associated with downslope-wind forecasts.

BIBLIOGRAPHY

Ancell, B. and G. J. Hakim, 2007: Comparing adjoint and ensemble sensitivity analysis. *Mon. Wea. Rev.*, **135**, 4117–4134.

Anthes, R. A., 1984: Predictability of mesoscale meteorological phenomena. *Predictability of fluid motions*, G. Holloway and B. J. West, Eds., American Institute of Physics, 247–270.

Anthes, R. A., Y. Kuo, D. P. Baumhefner, R. M. Errico, and T. W. Bettge, 1985: *Prediction of Mesoscale Atmospheric Motions*, Vol. 28B, 159–202.

Asselin, R., 1972: Frequency filter for time integrations. *Mon. Wea. Rev.*, **100**, 487–490.

Barker, D. M., W. Huang, Y. R. Guo, A. J. Bourgeois, and Q. N. Xiao, 2004: A three-dimensional variational data assimilation system for MM5: Implementation and initial results. *Mon. Wea. Rev.*, **132**, 897–214.

Bower, J. B. and D. R. Durran, 1986: A study of wind profiler data collected upstream during windstorms in Boulder, Colorado. *Mon. Wea. Rev.*, **114**, 1491–1500.

Bretherton, F., 1969: Momentum transport by gravity waves. *Quart. J. Roy. Met. Soc.*, **95**, 213–243.

Brinkmann, W. A. R., 1974: Strong downslope winds at Boulder, Colorado. *Mon. Wea. Rev.*, **102**, 592–602.

Caya, A. J., J. Sun, and C. Snyder, 2005: A comparison between the 4DVAR and the ensemble Kalman filter techniques for radar data assimilation. *Mon. Wea. Rev.*, **133**, 3081–3094.

Clark, T. L., W. D. Hall, and R. M. Banta, 1994: Two- and three-dimensional simulations of the 9 january 1989 severe Boulder windstorm: comparison with observations. *J. Atmos. Sci.*, **51**, 2317–2343.

Clark, T. L., W. D. Hall, R. M. Kerr, L. Radke, F. M. Ralph, P. J. Neiman, and D. Levinson, 2000: Origins of aircraft-damaging clear-air turbulence during the 9 december 1992 colorado downslope windstorm: Numerical simulations and comparison with observations. *J. Atmos. Sci.*, **57**, 1105–1131.

Clark, T. L. and W. R. Peltier, 1977: On the evolution and stability of finite amplitude mountain waves. *J. Atmos. Sci.*, **34**, 1715–1730.

Colle, B. A. and C. F. Mass, 1998: Windstorms along the western side of the Washington Cascade mountains. Part I: a high-resolution observational and modeling study of the 12 february 1995 event. *J. Atmos. Sci.*, **126**, 28–52.

Davies, H. C., 1976: A lateral boundary formulation for multi-level prediction models. *Quart. J. Roy. Met. Soc.*, **104**, 405–418.

Davies, L. A. and A. R. Brown, 2001: Assessment of which scales orography can be credibly resolved in a numerical model. *Quart. J. Roy. Met. Soc.*, **127**, 1225–1237.

Dirren, S., R. D. Torn, and G. J. Hakim, 2007: A data assimilation case-study using a limited-area ensemble Kalman filter. *Mon. Wea. Rev.*, **135**, 1455–1473.

Dowell, D. C., F. Zhang, L. J. Wicker, C. Snyder, and N. A. Crook, 2004: Wind and temperature retrievals in the 17 May 1981 Arcadia, Oklahoma, supercell: ensemble Kalman filter experiments. *Mon. Wea. Rev.*, **132**, 1982–2005.

Doyle, J. D., C. Amerault, and C. A. Reynolds, 2007: Sensitivity analysis of mountain waves using an adjoint model. *Meteor. Z.*, **16**, 607–620.

Doyle, J. D. and Q. Jiang, 2006: Observations and numerical simulations of mountain waves in the presence of directional wind shear. *Quart. J. Roy. Met. Soc.*, **132**, 1877–1905.

Doyle, J. D. and C. A. Reynolds, 2008: Implications of regime transition for mountain wave breaking predictability. *Mon. Wea. Rev.*, in pres.

Doyle, J. D. and M. A. Shapiro, 2000: A multi-scale simulation of an extreme downslope windstorm over complex topography. *Meteor. Atmos. Phys.*, **74**, 83–101.

Doyle, J. D. and R. B. Smith, 2003: Mountain waves over the Hohe Tauren: Influence of upstream diabatic effects. *Quart. J. Roy. Met. Soc.*, **129**, 799–823.

Doyle, J. D., H. Volkert, A. Dörnbrack, K. P. Hoinka, and T. F. Hogan, 2002: Aircraft measurements and numerical simulations of mountain waves over the central Alps: A pre-MAP test case. *Quart. J. Roy. Met. Soc.*, **128**, 2175–2184.

Doyle, J. D., et al., 2000: An intercomparison of model-predicted wave breaking for the 11 January, 1972 Boulder windstorm. *Mon. Wea. Rev.*, **128**, 900–914.

Durran, D. R., 1986a: Another look at downslope windstorms. Part I: The development of analogs to supercritical flow in an infinitely deep, continuously stratified fluid. *J. Atmos. Sci.*, **43**, 2527–2543.

Durran, D. R., 1986b: Mountain waves. *Mesoscale Meteorology and Forecasting*, P. S. Ray, Ed., American Meteorological Society, 472–492.

Durran, D. R., 1990: Mountain waves and downslope winds. *Atmospheric Processes Over Complex Terrain*, Amer. Meteor. Soc., 23, 59–81.

Durran, D. R., 1992: Two-layer solutions to Long's equation for vertically propagating mountain waves: How good is linear theory? *Quart. J. Roy. Met. Soc.*, **118**, 415–433.

Durran, D. R., 1999: *Numerical Methods for Wave Equations in Geophysical Fluid Dynamics*. Springer, 465 pp.

Echevin, V., P. De Mey, and G. Evensen, 2000: Horizontal and vertical structure of the representer functions for sea surface measurements in a coastal circulation model. *J. Phys. Oceanogr.*, **30**, 2627–2635.

Ehrendorfer, M., 1994: The Liouville Equation and its potential use for the prediction of forecast skill. Part I: Theory. *Mon. Wea. Rev.*, **122**, 703–713.

Ehrendorfer, M. and R. M. Errico, 1995: Mesoscale predictability and the spectrum of optimal perturbations. *J. Atmos. Sci.*, **52**, 3475–3500.

Ehrendorfer, M., R. M. Errico, and D. Raeder, 1999: Singular-vector perturbation growth in a primitive equation model with moist physics. *J. Atmos. Sci.*, **56**, 1627–1648.

Errico, R. M. and D. Baumhefner, 1987: Predictability experiments using a high-resolution limited-area model. *Mon. Wea. Rev.*, **115**, 488–504.

Evensen, G., 1994: Sequential data assimilation with a nonlinear quasi-geostrophic model using Monte Carlo methods to forecast error statistics. *J. Geophys. Res.*, **99 (C5)**, 10 143–10 162.

Evensen, G., 2003: The ensemble Kalman filter: theoretical formulation and practical implementation. *Ocean Dynamics*, **53**, 343–367.

Gal-Chen, T. and R. C. J. Somerville, 1975: On the use of a coordinate transformation for the solution of the Navier-Stokes equations. *J. Comput. Phys.*, **17**, 209–228.

Garvert, M. F., B. Smull, and C. Mass, 2007: Multiscale mountain waves influencing a major orographic precipitation event. *J. Atmos. Sci.*, **64**, 711–737.

Gaspari, G. and S. E. Cohn, 1999: Construction of correlation functions in two and three-dimensions. *Quart. J. Roy. Met. Soc.*, **125**, 723–757.

Gill, A. E., 1982: *Atmosphere-Ocean Dynamics*. Academic Press, New York, 662 pp.

Gohm, A., G. Zängl, and G. J. Mayr, 2004: South foehn in the Wipp Valley on 24 October 1999 (MAP IOP 10): verification of high-resolution numerical simulations with observations. *Mon. Wea. Rev.*, **132**, 78–102.

Grasso, L. D., 2000: The differentiation between grid spacing and resolution and their application to numerical modeling. *Bull. Amer. Meteor. Soc.*, **81**, 579–580.

Grubišić, V., et al., 2008: The Terrain-induced Rotor Experiment: An Overview of the field campaign and some highlights of special observations. *Bull. Amer. Meteor. Soc.*, **In press**.

Hakim, G. J. and R. D. Torn, 2006: Ensemble synoptic analysis. *Fred Sanders Monograph*, Amer. Met. Soc., accepted.

Hamill, T. M., 2001: Interpretation of rank histograms for verifying ensemble forecasts. *Mon. Wea. Rev.*, **129**, 550–560.

Hamill, T. M., 2006: Ensemble-based atmospheric data assimilation: A tutorial. *Predictability of weather and climate*, T. Palmer and R. Hagedorn, Eds., Cambridge University Press, 124–156.

Hamill, T. M., J. S. Whitaker, and C. Snyder, 2001: Distance-dependent filtering of background error covariance estimates in an ensemble Kalman filter. *Mon. Wea. Rev.*, **129**, 2776–2790.

Harshavardhan, R. Davies, D. Randall, and T. Corsetti, 1987: A fast radiation parameterization for atmospheric circulation models. *J. Geophys. Res.*, **92**, 1009–1015.

Hodur, R. M., 1997: The Naval Research Laboratory's coupled ocean/atmosphere mesoscale prediction system (COAMPS). *Mon. Wea. Rev.*, **125**, 1414–1430.

Hohenegger, C., D. Lüthi, and C. Schär, 2006: Predictability mysteries in cloud-resolving models. *Mon. Wea. Rev.*, **134**, 2095–2107.

Houtekamer, P. L. and H. L. Mitchell, 1998: Data assimilation using and ensemble Kalman filter technique. *Mon. Wea. Rev.*, **126**, 796–811.

Houtekamer, P. L. and H. L. Mitchell, 2001: A sequential ensemble Kalman filter for atmospheric data assimilation. *Mon. Wea. Rev.*, **129**, 123–127.

Houtekamer, P. L., H. L. Mitchell, G. Pellerin, M. Buehner, M. Charron, L. Spacek, and B. Hansen, 2005: Atmospheric data assimilation with and ensemble Kalman filter: results with real observations. *Mon. Wea. Rev.*, **133**, 604–620.

Jaubert, G., P. Bougeault, H. Berger, C. Chimani, C. Flamant, M. Häberli, M. Lothon, and S. Vogt, 2005: Numerical simulation of meso-gamma scale

features of föhn at ground level in the Rhine Valley. *Quart. J. Roy. Met. Soc.*, **131**, 1339–1361.

Kain, J. S. and J. M. Fritsch, 1990: A one-dimensional entraining/detraining plume model and its application in convective parameterization. *J. Atmos. Sci.*, **47**, 2784–2802.

Kain, J. S. and J. M. Fritsch, 1993: Convective parameterization for mesoscale models: The Kain-Fritsch scheme. *The representation of cumulus convection in numerical models, Meteor. Monogr.*, American Meteorological Society, 46, 165–170.

Klemp, J. and R. Wilhelmson, 1978: The simulation of three-dimensional convective storm dynamics. *J. Atmos. Sci.*, **35**, 1070–1096.

Klemp, J. B. and D. K. Lilly, 1975: The dynamics of wave-induced downslope winds. *J. Atmos. Sci.*, **32**, 320–339.

Klemp, J. B., W. C. Skamarock, and O. Furhrer, 2003: Numerical consistency of metric terms in terrain-following coordinates. *Mon. Wea. Rev.*, **131**, 1229–1239.

Lilly, D. K., 1978: A severe downslope windstorm and aircraft turbulence event induced by a mountain wave. *J. Atmos. Sci.*, **35**, 59–79.

Lilly, D. K. and E. J. Zipser, 1972: The Front Range windstorm of January 11, 1972. *Weatherwise*, **25**, 56–63.

Lorenc, A. C., 1986: Analysis methods for numerical weather prediction. *Quart. J. Roy. Met. Soc.*, **112**, 1177–1194.

Lorenz, E. N., 1969: The predictability of a flow which possesses many scale of motion. *Tellus*, **21**, 289–307.

Louis, J. F., 1979: A parametric model of vertical eddy fluxes in the atmosphere. *Bound.-Layer Meteor.*, **17**, 187–202.

Mass, C. F., D. Ovens, K. Westrick, and B. A. Colle, 2002: Does increasing horizontal resolution produce more skillful forecasts? *Bull. Amer. Meteor. Soc.*, **84**, 407–430.

McFarlane, N. A., 1987: The effect of orographically excited gravity wave drag on the general circulation of the lower stratosphere and troposphere. *J. Atmos. Sci.*, **44**, 1775–1800.

Mellor, G. and T. Yamada, 1974: A hierarchy of turbulence closure models for planetary boundary layers. *J. Atmos. Sci.*, **31**, 1791–1806.

Mesinger, F. and A. Arakawa, 1976: *Numerical Methods Used in Atmospheric Models*, GARP publication series, Vol. 17. World Meteorological Organization, 64 pp.

Mitchell, H. L. and P. L. Houtekamer, 2002: Ensemble size, balance, and model-error representation in an ensemble Kalman filter. *Mon. Wea. Rev.*, **130**, 2791–2808.

Nance, L. B. and B. R. Coleman, 2000: Evaluating the use of a nonlinear two-dimensional model in downslope windstorm forecasts. *Wea. Forecasting*, **15**, 717–729.

Nastrom, G. D. and D. C. Fritts, 1992: Sources of mesoscale variability of gravity waves. Part I: topographic excitation. *J. Atmos. Sci.*, **49**, 101–110.

Paegle, J. and Vukicevic, 1989: The influence of one-way interacting boundary conditions upon predictability of flow in bounded numerical models. *Mon. Wea. Rev.*, **117**, 340–350.

Palmer, T. N., G. J. Shutts, and R. Swinbank, 1986: Alleviation of systematic westerly bias in general circulation and numerical weather prediction models through an orographic gravity wave drag parametrization. *Quart. J. Roy. Met. Soc.*, **112**, 1001–1039.

Peltier, W. R. and T. L. Clark, 1979: The evolution and stability of finite-amplitude mountain waves II: Surface wave drag and severe downslope windstorms. *J. Atmos. Sci.*, **36**, 1498–1529.

Robert, A., 1966: The integration of a low order spectral form of the primitive meteorological equations. *J. Met. Soc. Japan*, **44**, 237–244.

Rutledge, S. A. and P. V. Hobbs, 1983: The mesoscale and microscale structure of organization of clouds and precipitation in midlatitude cyclones. VIII: A model for the "seeder-feeder" process in warm-frontal rainbands. *J. Atmos. Sci.*, **40**, 1185–1206.

Shutts, G., 1992: Observations and numerical model simulations of a partially trapped lee wave over the Welsh Mountains. *Mon. Wea. Rev.*, **120**, 2056–2066.

Smith, R. B., 1979: The influence of mountains on the atmosphere. *Adv. Geophys.*, B. Saltzman, Ed., Academic Press, Vol. 21, 87–230.

Synder, C. and F. Zhang, 2003: Assimilation of simulated doppler radar observations with an ensemble Kalman filter. *Mon. Wea. Rev.*, **131**, 1663–1677.

Tong, M. J. and M. Xue, 2005: Ensemble Kalman filter assimilation of Doppler radar data with a compressible non-hydrostatic model: OSS experiments. *Mon. Wea. Rev.*, **133**, 1789–1807.

Torn, R. D. and G. J. Hakim, 2008a: Ensemble-based sensitivity analysis. *Mon. Wea. Rev.*, **136**, 663–677.

Torn, R. D. and G. J. Hakim, 2008b: Performance characteristics of a pseudo-operational ensemble Kalman filter. *Mon. Wea. Rev.*, **136**, In press.

Torn, R. D., G. J. Hakim, and C. Snyder, 2006: Boundary conditions for a limited-area ensemble Kalman filter. *Mon. Wea. Rev.*, **134**, 2490–2502.

Velden, C., et al., 2005: Recent innovations in deriving tropospheric winds from meteorological satellites. *Bull. Amer. Meteor. Soc.*, **86**, 205–223.

Volkert, H., C. Keil, C. Kiemle, G. Poberaj, J. Chaboureau, and E. Richard, 2003: Gravity waves over the easter Alps: A synopsis of the 25 October 1999 event (IOP 10) combining *in situ* and remote-sensing measurements with a high-resolution simulation. *Quart. J. Roy. Met. Soc.*, **129**, 777–797.

Vukicevic, T. and R. M. Errico, 1990: The influence of artificial and physical factors upon predictability in estimates using a complex limited-area model. *Mon. Wea. Rev.*, **118**, 1460–1482.

Walser, A., D. Lüthi, and C. Schär, 2004: Predictability of precipitation in a cloud-resolving model. *Mon. Wea. Rev.*, **132**, 560–577.

Whitaker, J. S., G. P. Compo, X. Wei, and T. M. Hamill, 2004: Reanalysis without radiosondes using ensemble data assimilation. *Mon. Wea. Rev.*, **132**, 1190–1200.

Whitaker, J. S. and T. M. Hamill, 2002: Ensemble data assimilation without perturbed observations. *Mon. Wea. Rev.*, **130**, 1913–1924.

Wilks, D. S., 2006: *Statistical methods in the atmospheric sciences*. Academic Press, Burlington, MA, 627 pp.

Zhang, F., N. Bei, R. Rottuno, C. Snyder, and C. C. Epifanio, 2007a: Mesoscale

predictability of moist baroclinic waves: convective-permitting experiments and multistage error growth dynamics. *J. Atmos. Sci.*, **64**, 3579–3594.

Zhang, F., Z. Meng, and A. Aksoy, 2006: Tests of an ensemble Kalman Filter for mesoscale region-scale data assimilation. Part I: perfect model experiments. *Mon. Wea. Rev.*, **134**, 722–736.

Zhang, F., Z. Meng, and A. Aksoy, 2007b: Test of an ensemble kalman filter for mesoscale and regional-scale data assimilation. Part II: imperfect model experiments. *Mon. Wea. Rev.*, **135**, 1403–1423.

Zhang, F., C. Snyder, and R. Rottuno, 2002: Mesoscale predictability of the ”surprise” snowstorm of 24-25 January 2000. *Mon. Wea. Rev.*, **130**, 1617–1632.

Zhang, F., C. Snyder, and R. Rottuno, 2003: Effects of moist convection on mesoscale predictability. *J. Atmos. Sci.*, **61**, 1173–1185.

Zhang, F., C. Snyder, and J. Sun, 2004: Impacts of initial estimate and observation availability on convective-scale data assimilation with an ensemble Kalman filter. *Mon. Wea. Rev.*, **132**, 1238–1253.

Appendix A

NON-LINEAR NUMERICAL MODEL

The numerical integrations in this thesis are performed with the atmospheric portion of the Coupled Ocean/Atmosphere Mesoscale Prediction System (COAMPS; Hodur, 1997). A brief description of the numerical model is given in this section.

COAMPS solves a finite difference approximation to the fully non-linear, non-hydrostatic, compressible equations of motion on a terrain-following Arakawa-C grid. Prognostic equations for the zonal, meridional, and vertical velocities (u, v, and w), as well as potential temperature, θ, and perturbation Exner function, π are marched in time with a semi-implicit, split time-level second-order accurate integration (Klemp and Wilhelmson, 1978). Additionally, the grid-scale evolution of micro-physical variables for water vapor, q_v, cloud-water, q_c, rain water, q_r, ice, q_i, and snow q_s are accounted for.

Consistent with the C-grid staggering, the u and v variables are displaced one-half grid point in the zonal and meridional direction, respectively, while w is staggered one-half grid point in the vertical direction. The micro-physical variables are co-located with θ and π. Following Gal-Chen and Somerville (1975), the model utilizes a terrain-following height-based-σ coordinate defined by

$$\sigma = z_t \left(\frac{z - z_s}{z_t - z_s} \right) \tag{A.1}$$

where z_t is the model top, z_s is terrain height, and z is the physical height. In all experiments the model top is set to $z_t = 34.08$ km. Forty vertical levels are unevenly distributed with the highest resolution near the surface and coarse

resolution in the upper-most 10 km of the domains.

A.1 Model Equations

The set of dynamical equations on the transformed σ-height coordinate system can be written as

$$\frac{Du}{Dt} - fv + c_p\theta_v\left(\frac{\partial\pi}{\partial x} + G_x\frac{\partial\pi}{\partial\sigma}\right) = D_u + K_H\nabla^4 u, \tag{A.2}$$

$$\frac{Dv}{Dt} + fu + c_p\theta_v\left(\frac{\partial\pi}{\partial y} + G_y\frac{\partial\pi}{\partial\sigma}\right) = D_v + K_H\nabla^4 v, \tag{A.3}$$

$$\frac{Dw}{Dt} + c_p\theta_v G_z\frac{\partial\pi}{\partial z} = g\left(\frac{\theta'}{\bar{\theta}} + 0.608q'_v - q_c - q_r - q_s - q_i - q_g\right) + K_H\nabla^4 w, \tag{A.4}$$

$$\frac{D\pi}{Dt} + \dot{\sigma}\frac{\partial\bar{\Pi}}{\partial\sigma} + \frac{R_d}{c_v}\left(\bar{\Pi}+\pi\right)\left(\frac{\partial u}{\partial x} + \frac{\partial v}{\partial y} + \mathbf{G}\cdot\frac{\partial\mathbf{u}}{\partial\sigma}\right) - \frac{R_d}{c_v}\left(\frac{\bar{\Pi}+\pi}{\theta_v}\right)\frac{D\theta_v}{Dt} = 0, \tag{A.5}$$

$$\frac{DS^{(i)}}{Dt} = M^{(i)} + D_{s^{(i)}} + K_H\nabla^4\left(S^{(i)} - \bar{S^{(i)}}\right). \tag{A.6}$$

In the preceding,

$$\frac{D}{Dt} = \frac{\partial}{\partial t} + u\frac{\partial}{\partial x} + v\frac{\partial}{\partial y} + \dot{\sigma}\frac{\partial}{\partial z} \tag{A.7}$$

is the total derivative operator,

$$\bar{\Pi} + \pi = \left(\frac{R_d}{p_0}\rho\theta_v\right)^{\frac{R_d}{c_v}} \tag{A.8}$$

is the Exner function,

$$\theta_v = \theta\left(1 + 0.608q_v\right) \tag{A.9}$$

is the virtual potential temperature, and

$$\mathbf{G} = (G_x, G_y, G_z) = \nabla\cdot\sigma, \quad \text{and} \quad \dot{\sigma} = \mathbf{G}\cdot\mathbf{u} \tag{A.10}$$

are related to the terrain transform. Equation (A.6) represents the scalar advection of potential temperature θ ($S^{(1)} = \theta$) as well as the mixing ratios of

water vapor ($S^{(2)} = q_v$), cloud water ($S^{(3)} = q_c$), rain water ($S^{(4)} = q_r$), ice crystals ($S^{(5)} = q_i$), and snow ($S^{(6)} = q_s$). For θ, $M^{(1)}$ represents the sources and sinks of heat, while $M^{(2-4)}$ represent the sources and sinks of the micro-physical variables. In (A.2) - (A.8), ρ is the density; p_0 is a reference pressure; c_p and c_v are the specific heat at constant pressure and volume, respectively; R_d is the dry-air gas constant; g is the gravitational force; and f is the Coriolis force. In the preceding equations, over-bars represent background variables.

A.2 Parameterizations

The Rutledge and Hobbs (1983) microphysical parameterization is used to explicitly treat convective and non-convective moist processes in the numerical model. However, for the 27-km domain, convective motions are treated with the Kain and Fritsch (1990, 1993) cumulus parameterizations. Following the methods of Harshavardhan et al. (1987), the shortwave and longwave radiative transfer is computed every 1-hr during the model integrations. Turbulent mixing for momentum, heat, and the scalar quantities is represented through D_u, D_v, D_w, and $D_{s^{(i)}}$ with a 1.5 order, level 2.5 scheme (Mellor and Yamada, 1974). With this method a prognostic equation for the turbulent kinetic energy (TKE) is solved explicitly and then used to set the turbulent fluxes of heat, moisture and momentum. Surface fluxes of momentum and heat are represented with the Louis (1979) scheme.

A.3 Boundary Conditions

One-way nested lateral boundary conditions are used for all of experiments in this thesis. The lateral boundaries on the 27-km domain are specified from the Naval Operational Global Atmospheric Prediction System (NOGAPS) operational forecast according to the method of Davies (1976). The NOGAPS

fields are interpolated to the 7 outer-most COAMPS grid points with a bi-cubic spline and are then interpolated to the COAMPS vertical levels. A linear combination of the NOGAPS and COAMPS fields is computed at each of the 7 grid points with the NOGAPS field being fully weighted at the outer grid point and the COAMPS field being fully weighted at the 7^{th} grid point. The NOGAPS boundaries are updated every 6-hrs and the linear time tendency between two updates is used to specify the boundaries at the intermediate times. The boundaries for the nested domains are specified in the same way as the outer domains except that the COAMPS forecast is used to update the boundary at every time step.

The upper-boundary condition is specified by setting $\dot{\sigma} = 0$ at the top model level. In order to prevent spurious gravity-wave reflection from the top boundary, u, v, w, and θ are damped to smoothed values over the top 7 grid points of the model.

Topography on the lower boundary is specified from the 1-km resolution GLOBE DEM dataset and interpolated to the model grid points. A 25-point filter is applied to the interpolated topography field to remove the $2\Delta x$ signal. The lower boundary conditions is specified by setting $\dot{\sigma} = 0$ at the bottom model level.

A.4 Numerical Integration

The prognostic equations (A.2)–(A.6) are marched forward in time with a semi-implicit, split time-level second-order accurate integration (Klemp and Wilhelmson, 1978). A small time step is used to integrate the sound wave modes while a large time step is used to integrate the gravity- and Rossby-modes. The large time step is $\Delta t = 30$ s for the 27-km domain and reduced by a factor of 3 for each nested domain. The small time step is $\Delta\tau = 0.5\Delta t$. The large time step integration is computed with the second-order leapfrog method. To control the

computational mode associated with the leapfrog integration, a Robert-Asselin time filter (Robert, 1966; Asselin, 1972) is applied at each large time step with a coefficient of 0.2.

With the exception of the horizontal advective terms in (A.2)–(A.6), the spatial derivatives are computed with second-order finite differences. An option exists within COAMPS to compute the horizontal advective terms with either second-order or fourth-order finite differences. Both the second-order and fourth-order horizontal advective schemes are used throughout the thesis.

The maximum stable time step of the fourth-order advection scheme for the linear advection equation should be approximately 71% of the maximum stable time step for the second-order advection scheme (Durran, 1999). Tests with COAMPS revealed that the fourth-order scheme required a time-step approximately 30% of the second-order-scheme time step, which is considerably less than theory predicts. This excessive time-step reduction required for the integration to remain stable was linked to the way in which the $u\frac{\partial u}{\partial x}$ and $v\frac{\partial v}{\partial y}$ terms were calculated in (A.2) and (A.3), respectively. If the terms were calculated in the advective form, shown above, then the stringent time step was required to maintain stability. However, if the terms were calculated as $\frac{\partial u^2}{\partial x}$ and $\frac{\partial v^2}{\partial y}$, then the time step constraint was more consistent with linear theory. The cause of this sensitivity was not fully explored, however, it is suspected to be associated with the non-linear instability present in Burgers's Equation. Flux-form numerical integrations of Burgers's Equation are less susceptible to non-linear instabilities than advective form integrations (Durran, 1999).

Artificial numerical diffusion is required in non-linear numerical models to prevent the spurious build-up of energy at the shortest resolvable wavelengths. COAMPS uses a fourth-order diffusion operator which effectively removes the shortest wavelengths while leaving the longer wavelengths relatively unchanged. This operation is controlled by the parameter K_H in (A.2)–

(A.6). For the simulations in this thesis $K_H = -0.0025\Delta t/\left(\Delta x^2 \Delta y^2\right)$ which completely removes the 2Δ wave in one time step.

Appendix B

ENSEMBLE KALMAN FILTER

In this appendix, the Kalman Filter is derived from a general non-linear probability distribution of the model state and the observational information. The derivations in this section closely follows Lorenc (1986).

B.1 Bayesian Statement of Data Assimilation

The problem of sequential data assimilation can be concisely stated as on of trying to determine the probability density function (PDF) of the current atmospheric state[1] x_t given observations $\mathbf{Y}_t$ at the current time and at all previous times, or mathematically

$$P(\mathbf{x}_t|\mathbf{Y}_t). \tag{B.1}$$

Here, x_t is a state vector representing the atmosphere at time t, $\mathbf{Y}_t = [\mathrm{y}_t, \mathbf{Y}_{t-1}]$ is a vector containing every observation up to time t, y_t are the observations available at t, and P is the probability distribution.

Using Bayes theorem, (B.1) can be rewritten as

$$P(\mathbf{x}_t|\mathbf{Y}_t) \propto P(\mathbf{Y}_t|\mathbf{x}_t)P(\mathbf{x}_t). \tag{B.2}$$

If the observational errors are assumed to be temporally uncorrelated then they are independent from each other. Using the definition of independence the first term on the RHS of (B.2) can be rewritten as

$$P(\mathbf{Y}_t|\mathbf{x}_t) = P(\mathbf{y}_t|\mathbf{x}_t)P(\mathbf{Y}_{t-1}|\mathbf{x}_t). \tag{B.3}$$

[1]While the context in this thesis is limited to the atmosphere, the Kalman filter is applicable to any dynamical system.

Substituting (B.3) into (B.2) and once again using Bayes Rule gives the probabilistic update for data assimilation

$$P(\mathbf{x}_t|\mathbf{Y}_t) \propto P(\mathbf{y}_t|\mathbf{x}_t)P(\mathbf{x}_t|\mathbf{Y}_{t-1}). \tag{B.4}$$

The term on the left hand side (LHS) is the posterior PDF and is what we are seeking. This term is the probability of the current atmospheric state given all current and past observations. The first term on the RHS is the observational likelihood function which accounts for observational uncertainty associated with instrument errors and representativeness errors. The second term on the RHS is the prior PDF and represents the probability of the current state given all the observations prior to the current time. Equation (B.4) can repeated recursively every time a new observation is available, assuming that there is a method to generate a new prior.

B.2 Gaussian Approximation

In principal one could solve (B.4) by using the Liouville equation to update the new prior (Ehrendorfer, 1994), however; in practice this problem becomes computationally intractable for even small systems, let alone complex NWP models. It is therefore advantageous to assume that the distributions in (B.4) are normally distributed with a specified expected value and covariance. The normally distributed prior estimate can be written as

$$P(\mathbf{x}_t|\mathbf{Y}_{t-1}) \approx N(\mathbf{x}_t|\mathbf{x}_b, \mathbf{P}_b) \propto e^{-(\mathbf{x}_t-\mathbf{x}_b)^T\mathbf{P}_b^{-1}(\mathbf{x}_t-\mathbf{x}_b)}. \tag{B.5}$$

In the preceding, N is a normal distribution with mean $\mathbf{x}_b$ and covariance $\mathbf{P}_b$. In the context of (B.4), $\mathbf{x}_b$ is the background estimate given all previous observations is and $\mathbf{P}_b$ is the first moment of the distribution. The $\mathbf{P}_b$ matrix is square and positive definite. The normally distributed observation likelihood

can be written as

$$P(\mathbf{y}_t|\mathbf{x}_t) \approx N\left(\mathbf{y}^o|\mathcal{H}(\mathbf{x}_t), \mathbf{R}\right) \propto e^{-[\mathbf{y}^o-\mathcal{H}(\mathbf{x}_b)]^T\mathbf{R}^{-1}[\mathbf{y}^o-\mathcal{H}(\mathbf{x}_b)]} \tag{B.6}$$

Above, the observations at time t are written as $\mathbf{y}^o$, $\mathcal{H}(\mathbf{x}_t)$ is a non-linear vector valued function that maps the model state onto the observational space, and R is the observation-error covariance matrix. Substituting (B.5) and (B.6) into (B.4) and dropping the time index for simplicity gives

$$P(\mathbf{x}|\mathbf{Y}) \propto e^{-\mathbf{J}(\mathbf{x})} \tag{B.7}$$

where

$$\mathbf{J}(\mathbf{x}) = (\mathbf{x}-\mathbf{x}_b)^T\mathbf{P}_b^{-1}(\mathbf{x}-\mathbf{x}_b) + \left[\mathbf{y}^o - \mathcal{H}(\mathbf{x})\right]^T \mathbf{R}^{-1}\left[\mathbf{y}^o - \mathcal{H}(\mathbf{x})\right]. \tag{B.8}$$

Equation (B.7) is the Gaussian approximation to the data assimilation problem.

B.3 The Most Likely State

The maximum likelihood state can be determined by finding the state $\mathbf{x}_a$ that maximizes (B.7), or equivalently; minimizes (B.8). This is done by setting the derivative of (B.8) with respect to x equal to 0;

$$\left.\frac{\partial \mathbf{J}}{\partial \mathbf{x}}\right|_{\mathbf{x}_a} \propto \mathbf{H}\mathbf{R}^{-1}\left[\mathbf{y}^o - \mathcal{H}(\mathbf{x}_a)\right] - \mathbf{P}_b^{-1}(\mathbf{x}_a - \mathbf{x}_b) = 0. \tag{B.9}$$

In the preceding $\mathbf{H} = \frac{\partial \mathcal{H}}{\partial \mathbf{x}}$ is the Jacobian of $\mathcal{H}$ and represents a linear operator between the model space and observation space.

In general $\mathcal{H}(\mathbf{x}_a)$ is a non-linear function between the model space and observational space. For example, the radiative transfer equation for satellite observed radiance's or the power equation for observed radar reflectivities. This complexity makes solving (B.9) for $\mathbf{x}_a$ difficult. It is therefore necessary to linearize $\mathcal{H}(\mathbf{x}_a)$ about the background state $\mathbf{x}_b$:

$$\mathcal{H}(\mathbf{x}_a) = \mathcal{H}(\mathbf{x}_b) + \mathbf{H}\left(\mathbf{x}_a - \mathbf{x}_b\right). \tag{B.10}$$

Substituting (B.10) into (B.9) and rearranging gives

$$\mathbf{x}_a = \mathbf{x}_b + \left(\mathbf{H}^T\mathbf{R}^{-1}\mathbf{H} + \mathbf{P}_b^{-1}\right)^{-1}\mathbf{H}^T\mathbf{R}^{-1}\left[\mathbf{y}^o - \mathcal{H}(\mathbf{x}_b)\right]. \tag{B.11}$$

Using the fact that $\mathbf{P}_b$ and $\mathbf{R}$ are symmetric matrices (B.11) can be simplified by substituting the identity relationship

$$\left(\mathbf{H}^T\mathbf{R}^{-1}\mathbf{H} + \mathbf{P}_b^{-1}\right) = \mathbf{H}^T\mathbf{R}^{-1}\left(\mathbf{R} + \mathbf{H}\mathbf{P}_b\mathbf{H}^T\right)\left(\mathbf{P}_b\mathbf{H}^T\right)^{-1}$$

and using standard matrix operations. This substitution yields that Kalman Filter update equation

$$\mathbf{x}_a = \mathbf{x}_b + \mathbf{K}\left[\mathbf{y}^o - \mathcal{H}(\mathbf{x}_b)\right] \tag{B.12}$$

where

$$\mathbf{K} = \mathbf{P}_b\mathbf{H}^T\left(\mathbf{H}\mathbf{P}_b\mathbf{H}^T + \mathbf{R}\right)^{-1}. \tag{B.13}$$

Equation (B.12) states that the analysis that maximizes the Gaussian approximation to the data assimilation problem can be expressed as a linear combination between the background model state $\mathbf{x}_b$ and the innovation, $\mathbf{y}^o - \mathcal{H}(\mathbf{x}_b)$. The innovation is weighted by the Kalman Gain $\mathbf{K}$.

B.3.1 Minimizing the Analysis-Error Covariance

If the background state and the observations are assumed to be unbiased and uncorrelated with each other and the forward operator $\mathcal{H}(\mathbf{x})$ is linear (or approximated to be linear with (B.10)), then the analysis-error covariance can be written as

$$\mathbf{P}_a = (\mathbf{I} - \mathbf{K}\mathbf{H})\,\mathbf{P}_b\,(\mathbf{I} - \mathbf{K}\mathbf{H})^T + \mathbf{K}\mathbf{R}\mathbf{K}^T. \tag{B.14}$$

The preceding can be further simplified by substituting (B.13) into (B.14) to give

$$\mathbf{P}_a = (\mathbf{I} - \mathbf{K}\mathbf{H})\,\mathbf{P}_b. \tag{B.15}$$

The analysis-error covariances given in (B.14) is general in the sense that it does not depend on the particular form of $\mathbf{K}$. We will show in this section that if $\mathbf{K}$ is given by (B.13) then the total variance of $\mathbf{P}_a$ is minimized. Using a general weight matrix $\mathbf{W}$ in place of $\mathbf{K}$, (B.13) can be rewritten as

$$\mathbf{P}_a = \mathbf{P}_b - (\mathbf{WHP}_b)^T - \mathbf{WHP}_b + \mathbf{W}\left(\mathbf{HP}_b\mathbf{H}^T + \mathbf{R}\right)\mathbf{W}^T. \tag{B.16}$$

To minimize the total variance, we must minimize the trace of $\mathbf{P}_a$ with respect to $\mathbf{W}$. Using properties of the matrix trace and the fact that $\mathbf{P}_b$ and $\mathbf{R}$ are symmetric

$$\frac{\partial}{\partial \mathbf{W}}\text{trace}\left(\mathbf{P}_a\right) = -2\left[\mathbf{P}_b\mathbf{H}^T - \mathbf{W}\left(\mathbf{HP}_b\mathbf{H}^T + \mathbf{R}\right)\right]. \tag{B.17}$$

Setting the preceding equation equal to zero and solving for $\mathbf{W}$ yields

$$\mathbf{W}_{min} = \mathbf{P}_b\mathbf{H}^T\left(\mathbf{HP}_b\mathbf{H}^T + \mathbf{R}\right)^{-1}. \tag{B.18}$$

It is simple to see that this is a minimum by taking the second-derivative of (B.17) with respect to $\mathbf{W}$ and noting that $\left(\mathbf{HP}_b\mathbf{H}^T + \mathbf{R}\right)$ is positive definite. Comparing (B.18) to (B.13) reveals that $\mathbf{W}_{min} = \mathbf{K}$, in other words, the Kalman Gain $\mathbf{K}$ minimizes the total variance of the analysis error covariance matrix.

B.4 The Kalman Filter

In the previous section the most likely analysis state and analysis-error covariance were derived in terms of the background state and the background-error covariance, respectively. The key to the Kalman filter is that it provides a method to update the background-error covariances.

If $\mathbf{M}_{t,t_0}$ is a linear model which evolves the state vector $\mathbf{x}(t)$ from time t_0 to time t then the new background state can be written in terms of the analysis state as

$$\mathbf{x}_b = \mathbf{M}\mathbf{x}_a + \epsilon \tag{B.19}$$

where ϵ represents a model error term with zero mean and covariance matrix $\mathbf{P}_Q$. The new background-error covariance can then be written as

$$\mathbf{P}_b = \left\{\mathbf{x}_b{\mathbf{x}_b}^T\right\} = \left\{\mathbf{M}\mathbf{x}_a{\mathbf{x}_a}^T\mathbf{M}^T\right\} + \left\{\epsilon{\mathbf{x}_a}^T\mathbf{M}^T\right\} + \left\{\mathbf{M}\mathbf{x}_a\epsilon^T\right\} + \left\{\epsilon\epsilon^T\right\} \tag{B.20}$$

where the curly brackets represent the expected value. If it is assumed that the model error is uncorrelated with the analysis then the second and third terms on the RHS of the preceding equation vanish and the updated background-error covariance can be simplified to

$$\mathbf{P}_b = \mathbf{M}\mathbf{P}_A\mathbf{M}^T + \mathbf{P}_Q. \tag{B.21}$$

The Kalman filter can thus be summarized as using using (B.19) and (B.21) to evolve the analysis state and analysis-error covariances to a new background state and background-error covariance. These flow dependent statistics are used to assimilate new observations according to (B.12), (B.13), and (B.15). This process can be repeated to continuously assimilate new observations and produce new background states.

B.4.1 Putting the "En" in the "KF": The ensemble Kalman filter

In general, (B.19) and (B.21) are not applicable for data assimilation problems in geophysical fluid dynamics such as NWP. The dynamics are sufficiently non-linear so (B.19) is not directly applicable. It may be possible to use a tangent linear model to approximate (B.19), however, the state-space of NWP is still to large to compute (B.21) directly. Evensen (1994) proposed a method in which Monte Carlo simulations are used to estimate $\mathbf{P}_b$. In this way a fully non-linear model can be used to evolve the analysis state $\mathbf{X}_a$ to a new background state $\mathbf{X}_b$. Here the upper-case $\mathbf{X}$ represents a matrix in which each column represents an individual ensemble member in the Monte-Carlo simulation. The

new background-error covariance can then be estimated as

$$\mathbf{P}_b \approx \frac{1}{N-1}\mathbf{X}_b'\mathbf{X}_b'^T \tag{B.22}$$

where N is the number of ensemble members and the prime indicates a perturbation about the ensemble mean. Using a non-linear numerical model to evolve $\mathbf{P}_b$ is completely flow dependent and consistent with the model dynamics. Observations can be assimilated according to (B.12) using (B.13). In implementing the EnKF the full covariances usually do not need to be stored in computer memory and efficient algorithms have been developed to perform the data assimilation (e.g. Whitaker and Hamill, 2002).

Appendix C

TWO-MONTH-LONG EXPERIMENT

For several reasons, it was beneficial to cycle the EnKF data assimilation system on 27-km synoptic-scale COAMPS domain for the entire two-month TREX SOP. For one, the two-month long experiment generated a reasonably large set of statistics in which the EnKF could be evaluated. Additionally, performing the long-term experiment allowed the ensemble to be appropriately calibrated by determining several parameters experimentally. Finally, because of the high computational cost of the high-resolution ensemble simulations, they could only be run during specific periods of interest. The 27-km domain ensemble was able to provide an initial ensemble for the higher resolution experiments. This appendix describes the setup two-month-long experiment on the 27-km domain.

The geographic location as well as the topography on the 27-km domain is shown in Fig. C.1. The domain extends from approximately 150° W in the Pacific Ocean to 105° W along the Rocky Mountains and from approximately 25° N near the southern most point of Baja California to 55° N near the southern most point of Alaska. The large domain is necessary so the eastward propagating disturbances will take several assimilation cycles to reach the Sierra-Nevada mountains from the western domain boundary. The domain is place on Lambert Conformal projection with two standard latitudes of 60° N and 30° N and a standard longitude of 119.4° W which is directly over the southern Sierra-Nevada mountains. The horizontal grid spacing is 27-km with maximum and minimum map scale factors of 1.036 and 0.942, respectively.

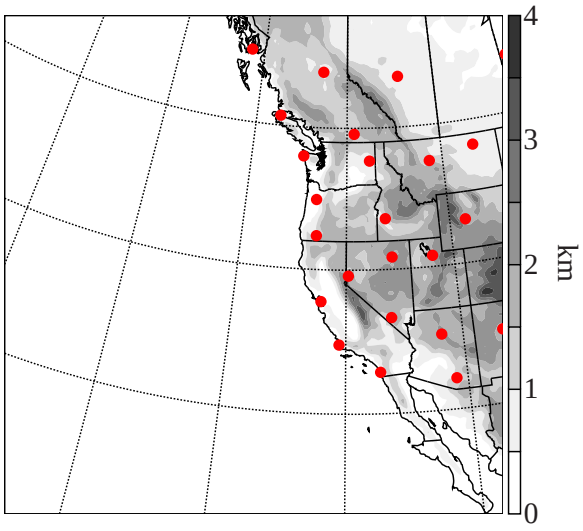

Figure C.1: The topography on the 27-km domain. The geographic locations of the upper-air soundings used for assimilation are shown with red dots.

C.1 Initial Ensemble

The 70-member ensemble is initialized 12 UTC, 02 March 2006 by interpolating a 36-hr forecast of the Naval Operational Global Prediction System (NOGAPS) to the 27-km domain and adding random perturbation drawn from the WRF-VAR static-covariances (Barker et al., 2004). Following Torn and Hakim (2008b), the initial perturbations are scaled by a factor of 1.75 so that the initial ensemble variance is slightly larger than the RMS error between the ensemble mean and radiosonde observations. The ensemble size was limited to 70 members by the computational resources available. Several studies have indicated that ensembles with $O(100)$ members are sufficient to perform data assimilation on the synoptic scale (e.g. Whitaker et al., 2004; Mitchell and Houtekamer, 2002; Dirren et al., 2007).

C.2 Observations Assimilated

The EnKF is used to assimilate several types of observations that are available at the 6-hr cycling interval. Surface observations of wind speed, wind direction, temperature and pressure data are assimilated from fixed off-shore buoys and on-shore automated surface observing system (ASOS) stations. Additionally, pressure data from off-shore drifting buoys and on-shore meso-networks are assimilated. Surface stations that are displaced more than 100 m from the model topography are not assimilated because of potential biases. Radiosonde observations of wind speed, wind direction, temperature, and relative humidity are assimilated at mandatory levels when available. The upper-air radiosonde network is indicated in Fig. C.1 for reference. The aircraft communication addressing and reporting system (ACARS) is used to assimilate observations of wind speed, wind direction, temperature, and relative humidity. These observations are mostly concentrated surrounding major airports and along routinely used flight corridors. Finally, satellite observations of cloud-drift winds are assimilated (Velden et al., 2005).

C.3 Boundary Conditions

In order to avoid an artificial loss of ensemble variance associated with the prescribed deterministic NOGAPS boundary conditions, perturbations are applied at the boundaries according the the fixed-covariance method of Torn et al. (2006). With this method boundary perturbations evolve in time as an autoregressive process with a specified autocorrelation coefficient of 0.5. The static background-error covariances from the WRF-VAR system (Barker et al., 2004) are used to perturb the boundaries for each ensemble member. In order to maintain an adequate amount of ensemble variance, the boundary perturbations are scaled by a factor of 1.75.

C.4 Filter Divergence

As a consequence of using a relatively small ensemble to sample the background-error statistics, the covariance estimates can generate spurious long-distance relationships (Houtekamer and Mitchell, 2001; Hamill et al., 2001). Additionally, rank-deficient ensembles will tend to underestimate the covariance magnitude (Whitaker and Hamill, 2002). If left unaccounted for, these two issues can lead to "filter divergence", a condition where the ensemble becomes over-confident in its estimate of the background state and subsequently rejects new observations (Hamill, 2006). To deal with filter divergence two standard practices are employed: covariance inflation and covariance localization.

C.4.1 Covariance Inflation

We use the covariance relaxation procedure described by (Zhang et al., 2004) to inflate the analysis-error covariances. With this method, the prior and posterior covariances are combined with a weighted average to give a new posterior covariance. We use weights of 0.775 and 0.225 for the prior and posterior covariances, respectively. These values were determined experimentally so that the ensemble variance is similar to the mean RMS errors. These values are similar to those used by Torn and Hakim (2008b) who cycled a similar mesoscale EnKF data assimilation system.

C.4.2 Covariance Localization

The long-distance correlation issue is handled with the localization function which is unity at the observation location and decreases monotonically to zero 3000 km from the observation (Gaspari and Cohn, 1999, Eq. (4.10)). The localization is isotropic and is limited to the horizontal. It has a half-width scale of

approximately 1000 km.

C.5 Evaluating the Ensemble

In this section the performance of the ensemble is briefly demonstrated by considering several rank-histograms computed over the two-month long data-assimilation experiment. This performance assessment is in no-way a complete evaluation of the synoptic-scale ensemble, but is instead intended to demonstrate that the ensemble variance is properly calibrated. Attention is limited to the mid-tropospheric wind speed and temperature, as these synoptic-scale variables are most closely related to the variables controlling mountain-waves and downslope winds.

The rank histogram is a tool to verify the appropriateness of the ensemble calibration (Hamill, 2001). To compute the rank histogram the ensemble estimate of an observation is first ordered from lowest to highest. The actual observation is then ranked within that ordering and placed into a bin for that ranking. For example, if 15 out of 70 ensemble members had weaker winds than an observation, then that observation would be placed into the 15^{th} bin. If this process is repeated for all available observations then the statistical characteristics of the ensemble can be systematically evaluated.

Several canonical structures of the rank histogram have been described and analyzed in Hamill (2001). For example, a well calibrated ensemble in which the observation is likely to occur in any rank will have a rank histogram that is uniformly distributed. On the other hand, observations that routinely fall outside of the span of the ensemble will be characterized by a u-shaped rank histogram. This is often a sign that the ensemble is under-dispersive. Similarly, the rank histogram for and over-dispersive ensemble is characterized by a hump in the middle of the distribution. Consistent model biases can also be identified with rank histograms. A rank histogram that slopes up (down)

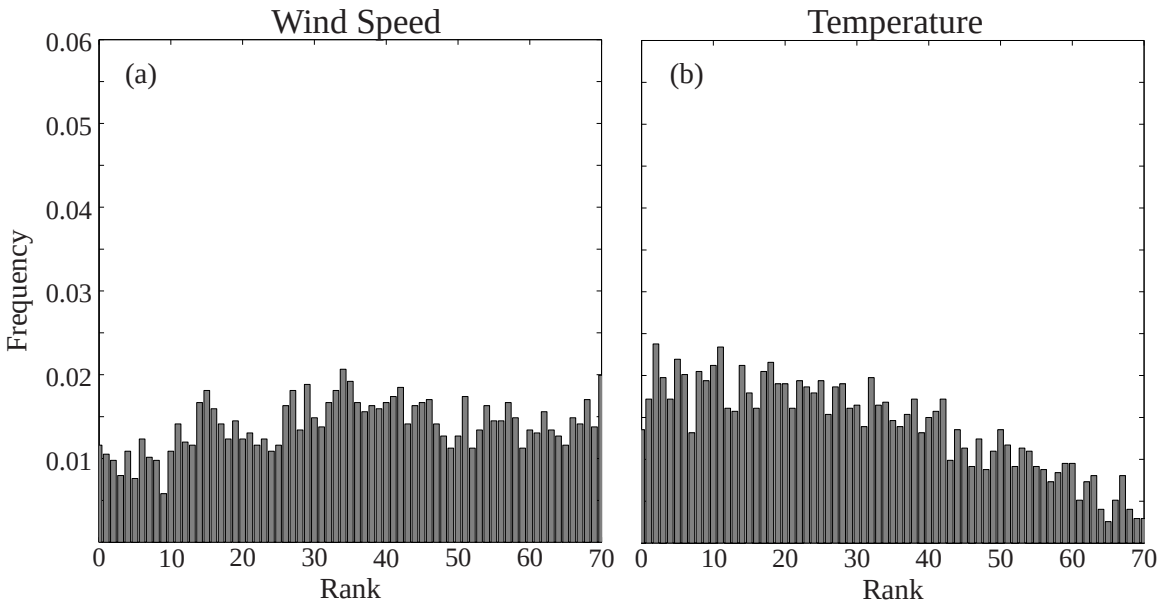

Figure C.2: Rank histograms for the two-month-long experiment of the 500-hPa (a) wind speed and (b) temperature.

towards higher (lower) ranks can signify that the model as a low (high) bias.

Figure C.2 shows the rank histogram of 500 hPa wind speed and temperature computed from 6-hr forecasts using radiosonde data. The 6-hr forecast is used instead of the analysis because the radiosonde observational data would be included into the analysis. A slight warm bias is apparent from the temperature rank histogram (Fig. C.2b) as evident from the right to left upward slope of the distribution. However, the variance for both wind speed and temperature appears to be well calibrated.

The 700 hPa rank histograms for wind speed and temperature are plotted in Fig. C.3. At this level the wind speed histogram indicates a slightly over-dispersive ensemble. However, this is not very alarming because filter divergence is not a large concern with an over-dispersive ensemble. The temperature at 700 hPa is fairly well calibrated, however, a slight increase in the rank from right to left indicates a small warm bias in the temperature. The warm tem-

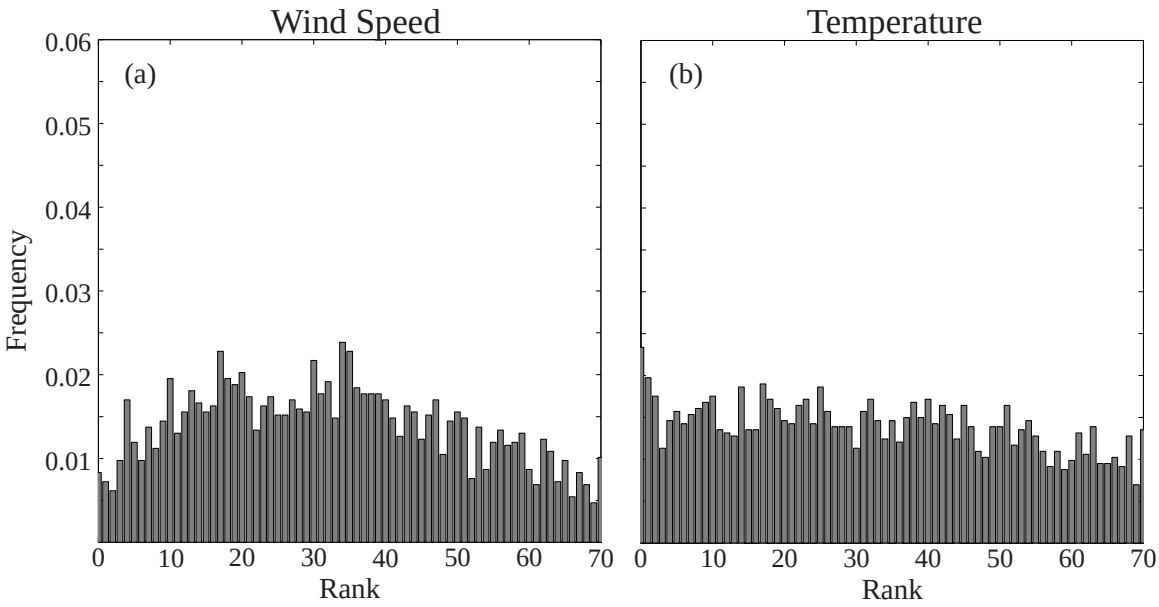

Figure C.3: The same as Fig. C.2 except for 700 hPa.

perature bias at 700-hPa and 500-hPa is in part responsible for a high height bias at 500 hPa (not shown).

VITA

Patrick “Alex” Reinecke was born an raised in Vienna, VA. Immediately following high school he took a job with a civil engineering firm collecting and testing soil and concrete samples. This job directed Alex decidedly away from engineering and soon after he took up scholarship of mathematics at the University of Utah. While in Utah, Alex met his future wife Amy with whom he is happily married to. Immediately following a Bachelor of Science degree in 2002, Alex took up residence in the graduate program at the Department of Atmospheric Science at the University of Washington under the Guidance of Dale Durran. While at the University of Washington Alex has studied problems ranging from orographic blocking to the predictability of downslope winds and mountain waves. Alex has participated in several field campaigns including the Vertical Transport and Mixing Experiment, the Sierra Rotors Project, and the Terrain-Induced Rotors Experiment.